SPAT0016-2: Stage en industrie

Internship Report at ESO:

Optimization of the VLT/Naco alignment procedure to reduce the non-common path errors

Author:
Christiaens Valentin

Coordinator:
Defise Jean-Marc

Supervisors:
Girard Julien
Mawet Dimitri
O'Neal Jared

Département d'Astrophysique, Géophysique et Océanographie
Université de Liège
Liège, Belgium

vchristiaens@student.ulg.ac.be

June 3, 2012

Abstract

NaCo is a state-of-the art instrument mounted on UT4 at Paranal Observatory (ESO). Fed by the adaptive optics system NAOS, CONICA is widely used by the scientific community and allowed several scientific breakthroughs. What constitutes the hidden side of the instrument is the set of calibrations required to obtain optimal performances. We focus here on calibrations correcting static aberrations, taking the shape of so-called *speckles* in the images. A new calibration procedure has been proposed recently to correct more efficiently these static aberrations. Within the framework of this procedure, whose implementation requires teamwork, I was assigned a specific task consisting in the calibration of CONICA's non-common path aberrations, using the new software *OPRA* as well as several *Strehl meters*. The purpose of this report is to compile and comment all the results obtained during these calibrations.

Acknowledgments

First, I want to acknowledge my professor, Jean-Marc Defise, who allowed me to do this internship.

I profoundly acknowledge my supervisors Julien Girard[1], Dimitri Mawet[2], and Jared O'Neal[3] for all their wise advice and suggestions, their patience in answering all my questions and the good atmosphere that they spread during my internship. Thank you very much guys! A special thanks also goes to Pedro Mardones for its guided tour of UT4 and the instrument NaCo!

I also express my gratefulness to Olivier Absil and Charles Hanot, who helped me at the very first steps of the procedure to get this internship. Without them, I would never have met my supervisors.

Last but not least, I acknowledge ESO, and particularly Michael West, for allowing me to carry out this internship and achieve such a rewarding experience, both in Santiago and at the observatory of Paranal. Also, I'm very grateful to Paulina Jiron, for all the actions undertaken to help me recovering my notebook which contained key information concerning both my master thesis and my internship.

This internship was supported by ESO (allowance for lodging and living expenses) and the Université de Liège (airfare).

[1] Operation staff astronomer, NaCo instrument scientist.
[2] Operation staff astronomer, NaCo and Vizir second instrument scientist.
[3] Instrumentation Engineer, NaCo instrument responsible.

Contents

List of Figures

List of Tables

Acronyms

AO	Adaptive Optics
AT	Auxiliary Telescope
CONICA	COudé Near-Infrared CAmera (Imager and Spectrograph)
DIT	Detector Integration Time
DM	Deformable Mirror
FOV	Field Of View
FS	Field Selector
FWHM	Full Width at Half Maximum
IB	Intermediate Band
ICS	Instrument Control Software
IM	Interaction Matrix
LOCI	Locally Optimized Combination of Images
MAD Sr Meter	Strehl Meter developed during the MAD Project
mas	Milli-arcsecond
MVD Sr Meter	Strehl Meter developed by Marcos van Dam
NaCo	NAos-COnica
NAOS	Nasmyth Adaptive Optics System
NB	Narrow Band
NCPAs	Non-Common Path Aberrations
NGS	Natural Guide Star
OB	Observing Block
OPRA	OTF-based Phase Retrieval Analysis
OTF	Optical Transfer Function
PD	Phase Diversity
PV	Peak-to-Valley
px	pixel
PSF	Point Spread Function
rms	Root mean square
RON	Readout Noise
RS	Reference Slopes
SOS	Super Operating System
SPHERE	Spectro-Polarimetric High-contrast Exoplanet Research
Sr	Strehl ratio
TTM	Tip/Tilt Mirror
UT	Unit Telescope
WFS	Wavefront Sensor
WFSAS	Wavefront Sensor Artificial Source

1 Introduction

This internship takes place in the framework of the course *Conception d'une mission spatiale et/ou stage en industrie, partim 2.* It consists in a detailed analysis of a mission or a specific problem encountered by a scientific team in charge of the preparation or the operation of a mission or an instrument. The objective is to confront the student to the problems encountered by the investigators and to help them solving it by the participation in several tasks related to it.

1.1 Motivations

Besides being world's foremost intergovernmental astrophysical and technical organization, ESO offers the possibility to astronomers to use some of the most advanced instruments in the field. As a student, it is an honour to have the chance to work in this organization and try to improve the calibration procedure of the cutting edge instrument NaCo.

In addition, the subject of this internship takes place in an emerging field of observational astrophysics which is high contrast imaging and characterization of extra-solar planetary systems (exoplanets and circumstellar disks). This internship was the opportunity to contribute to this hot topic and more exactly to the root of scientific observations structure: optimization of instrument calibrations. Moreover, this gain of experience will also favour pursuing a PhD thesis that will be simultaneous to the arrival of SPHERE instrument.

1.2 ESO

ESO is the European Organization for Astronomical Research in the Southern Hemisphere. It builds and operates cutting edge research facilities for astronomers and astrophysicists, allowing them to carry out front-line science in the best conditions. As the foremost intergovernmental astronomy organization in Europe, it is equally the world's most productive astronomical observatory.

ESO's 15 member states, supporting the organization, are Austria, Belgium, Brazil, the Czech Republic, Denmark, Finland, France, Germany, Italy, the Netherlands, Portugal, Spain, Sweden, Switzerland and the United Kingdom. The annual member state contributions to ESO are approximately 131 million Euros and ESO employs around 730 staff members. This investment is fruitful: providing the world's most powerful ground-based telescopes to astronomers enables important scientific discoveries. ESO offers numerous possibilities for technology spin-off and transfer, as well as high technology contract opportunities. Consequently, ESO is also a stupendous showcase for European industry.

The headquarters, located in Garching near Munich, consists of the scientific, technical and administrative centre of the organization. Besides Garching, there is the Santiago Centre, where I spent most of my time during my internship and also three remarkable observing sites in Chile: La Silla, Paranal and Chajnantor. In La Silla, ESO operates several intermediate size telescopes, among which the most prolific exoplanet hunter instrument (HARPS spectrograph on the 3.6m telescope). The plateau of Chajnantor, located 5000m high and close to San Pedro de Atacama, hosts the submillimetre telescope APEX and the huge network of submillimetre telescopes ALMA, still under construction together with international partners. Presently, ESO is also involved in the design of the European Extremely Large Telescope.

Located about 130km south of Antofagasta, Mount Paranal (2600m high) is one of the driest place on Earth. This site hosts the Very Large Telescope array (VLT), whose overview is given in figure 1). Scientific activities started in 1999, and led to numerous successful research programs. It is currently the key observatory of European astronomy, in visible and near-infrared, with its

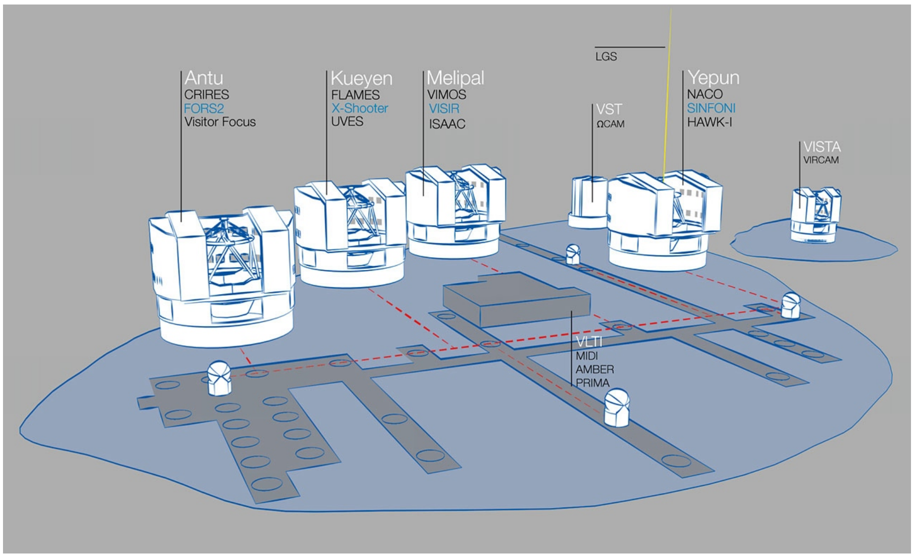

Figure 1: Distribution of the instruments among the four UTs at the VLT (Image from ESO website: http://www.eso.org/sci/facilities/paranal/instruments/overview.html).

four Unit Telescopes (hereafter UTs), four Auxiliary Telescopes (hereafter ATs), the telescopes VST and VISTA, which are dedicated to wide field surveys of the Universe, and the possibility to combine UTs or ATs together as interferometers (VLTI). The four UTs are all equipped with an 8.2m diameter primary mirror, as the complementary and moveable ATs are 1.8m in diameter.

Eleven first generation instruments and a second generation one are currently in operation at the VLT. Their distribution among the different UTs is given in figure 1. Within this framework, my work was exclusively focused on NaCo, which is an instrument mounted on UT4 (Yepun). Three other second generation instruments are awaited soon, including SPHERE, which as a high contrast exoplanet searcher, is considered as the successor of NaCo.

More information is available at http://www.eso.org/public/ .

1.3 Specification of problem and initial objective

NaCo is composed of 2 instruments: NAOS, the *adaptive optics* (AO hereafter) system, and CONICA, the science camera (see section 3 for further information). As for most instruments equipped with an AO system, the light path has to be separated in two by a *beam splitter* (BS hereafter), as one part has to feed the AO system so that it can apply corrections to the *deformable mirror* (DM hereafter), and as the other part is used for science purpose (figure 2).

Therefore, aberrations that would appear in the wavefront after the BS and before the science camera (part (a) in figure 2), would not be corrected by the AO system in closed loop. These aberrations are known as the *non-common path aberrations* (NCPAs hereafter) of CONICA and can typically be due to the collimator, masks, filters and camera of CONICA.

In a similar manner, the aberrations that would appear between the BS and the wavefront sensor (part (b) in figure 2) will be seen by the AO system and *erroneously* corrected since the part of the beam that goes to the science camera is not affected by those aberrations. In this case, we are dealing with the NCPAs of NAOS, which can be caused by the reflecting surface of the dichroic used or the mis-alignment of the WFS sub-pupils.

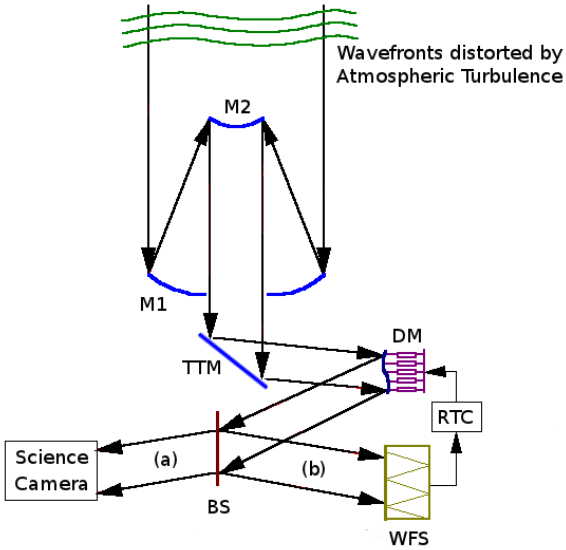

Figure 2: Simplified diagram of an AO System. Distorted wavefronts arrive in the telescope, they are reflected by the primary and secondary mirror (M1 and M2), the tip-tilt mirror (TTM) and the deformable mirror (DM). The light is then separated by a beam splitter (BS). The transmittive part goes to the science camera, whereas the reflective part is used to feed the wavefront sensor (WFS). A real-time computer (RTC) allows then to provide proper corrections to the DM.

The primary objective of this internship was to take part in the elaboration of a new procedure to calibrate the NCPAs of NaCo. My task in that project was more specifically to optimize, automatize and test the CONICA NCPAs calibration with a new *phase diversity* (PD hereafter) software called OPRA. A theoretical approach of the PD principle is summarized in section 2.1, and information about OPRA can be find in subsection 4.3. As will be shown in this report, it turned out that this tool was also useful as a metric to quantify the effects of several parameters on the image quality (section 4.6). A theoretical reminder of the two main AO's figures of merit is therefore given in section 2.2. It also logically ensued that a thorough study of the different computation techniques of the Strehl ratio was necessary (section 4.4).

1.4 Link with my master thesis

My internship allowed me to get used with the calibration process of instrument NaCo and also, indirectly, with the acquisition of data. The subject of my master thesis is in the temporal continuation of my internship since it is focused both on the improvement of a post-processing technique and its use on scientific targets gathered thanks to the instruments NaCo.

The post-processing technique in question is called LOCI, for Locally Optimized Combination of Images, and was initially developed by Lafrenière et al. (2007). Its goal is to reduce the quasi-static speckles which curb the high-contrast direct imaging of exoplanets, subtracting optimized combinations of reference PSF images sequentially for different sub-sections of the images (i.e.: *locally*). Those quasi-static speckles are long-lived since they are due to imperfections in the optics. Therefore, better calibrations give less significant quasi-static speckles, and hence a higher detectability of planetary companions.

2 Theoretical Considerations

2.1 Phase Diversity technique

2.1.1 Fourier optics considerations

In the Fraunhofer approximation, the image $i(\mathbf{r})$ of an object $o(\mathbf{r})$, given by an optical system characterized by its PSF $h(\mathbf{r})$, is the noisy convolution of $h(\mathbf{r})$ with $o(\mathbf{r})$:

$$i(\mathbf{r}) = (h * o)(\mathbf{r}) + n(\mathbf{r}) \tag{1}$$

where $\mathbf{r}$ is an M-dimensional spatial coordinate in the Fourier plane and $n(\mathbf{r})$ represents the photon and detector noises.. In astronomy, $M = 2$, since one is usually dealing with images.

Phase errors are introduced by both the atmosphere and the instrument. In the latter case, one is dealing with the so-called *optical aberrations*. In fact, not only the incoming wavefront is not planar, but the instrument itself is introducing aberrations. These aberrations are taken into account in the impulse response that constitutes the PSF. Since the PSF is the squared modulus of the inverse Fourier transform of the complex pupil function, its expression is given by

$$h(\mathbf{r}) = |FT^{-1}[P(\mathbf{u})]|^2 = |FT^{-1}\{[A(\mathbf{u}).\exp[j\phi(\mathbf{u})]\}|^2 \tag{2}$$

where $\mathbf{u}$ is an M-dimensional spatial coordinate in the pupil plane, $P(\mathbf{u})$ is the pupil function, $A(\mathbf{u})$ is the aperture function and $\phi(\mathbf{u})$ is the aberrated phase.

Aberrations can be expanded in polynomial series, whose sum constitutes the wavefront. A well-known basis of orthogonal polynomials was invented by Zernike (Zernike, 1934). His polynomials are particularly fitted to full circular pupils. Since most of modern telescopes are centrally obscured, the set of polynomials introduced by Mahajan (1981) may be more convenient. Zernike polynomials are characterized by two indices, however using the nomenclature introduced by Noll (1976) (figure 3), aberrations can be mathematically represented by a single index:

$$\phi(\mathbf{u}) = \sum_{i=2}^{k} a_i Z_i(\mathbf{u}) \tag{3}$$

Noll notation labels the focus with i=4, the tangential and sagittal astigmatism with i=5 and 6, coma with i=7 and 8, and so on. In order to describe any wavefront form, k should tend to infinity. In practice however, and in the specific case of static aberration (i.e. long lived aberrations, which are due to the instrument) estimates, the first dozens of polynomials are enough.

2.1.2 Overview of the phase-retrieval methods

Since aberrations reduce the image quality, one wants to measure them in order to minimize them. Optical testing aim at characterizing the phase errors that are introduced by the optical system itself, whereas the aberrations that are caused by the atmosphere are dealt with AO, assuming the AO system introduces very little aberration.

Classical methods of optical testing mainly involve the measurement of the shape of the tested surface. By *classical methods*, we denote the Foucault test, the null test, the Ronchi test (Ronchi, 1964), computer generated holograms (MacGovern & Wyant, 1971), the Hartmann test[4]

[4]The Hartmann test adds a perforated screen in the lightpath, creating rays when the light goes through it, in order to perform a kind of *ray-tracing* analysis. Its evolution, the Shack-Hartmann sensor, can be used with very low illumination, using this time an array of lenslet.

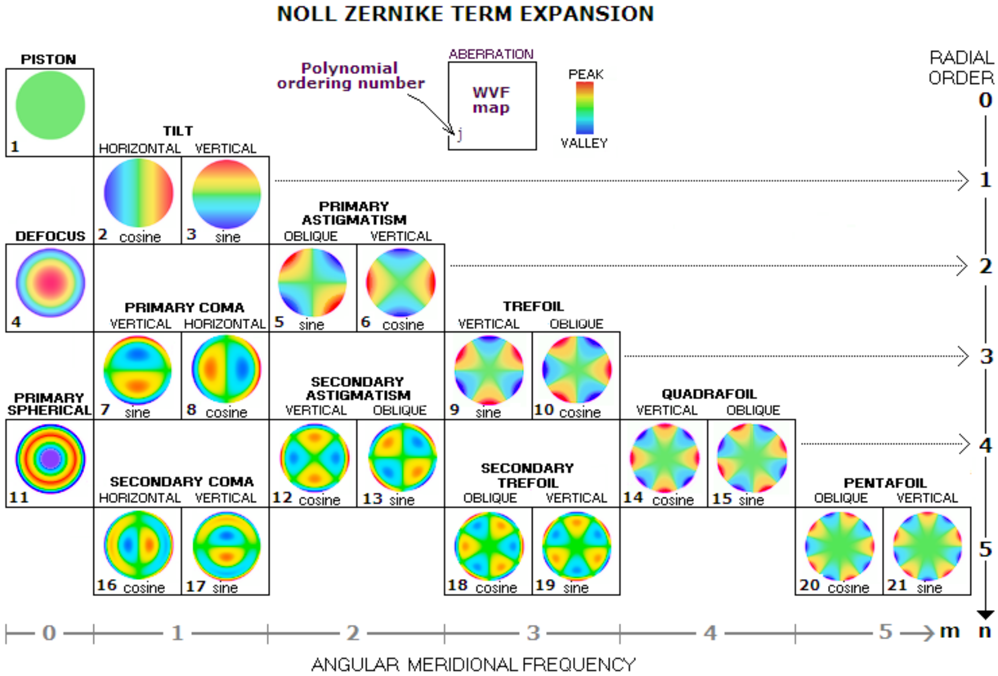

Figure 3: Noll's nomenclature of the Zernike polynomials.

(Hartmann, 1900; Shack & Platt, 1971) and the Roddier test[5] (Roddier et al., 1990).

As for AO systems, one can distinguish interferometric and non-interferometric wavefront sensors. The latter can, in turn, be classified in two main groups: slope and curvature based sensors. The main representatives of the two groups are respectively the aforementioned Shack-Hartmann and Roddier wavefront sensors, although another type of slope sensing WFS has appeared recently: the *Pyramid* WFS (Ragazzoni & Farinato, 1999). More details about AO systems wavefront sensing methods are available in my master thesis.

The wavefront sensors can detect and correct any degradation preceding it (i.e. any common path errors). As mentioned in section 1.3, aberrations however also appear in non-common paths, either in the part of NAOS between the surface of the dichroic and the WFS, or in CONICA which in terms of light path is located after the dichroic. These NCPAs are due to optical elements such as the surface of the dichroic, the off-axis focusing parabola at the output of NAOS, or the filters and masks present in CONICA. Either the propagation through them or their misalignment introduce different phase errors. Whereas it is possible to treat the aberrations introduced by the surface of the dichroic with a calibration lamp located upstream, for the parabola at the output of NAOS and CONICA optical elements the Shack-Hartmann WFS of NAOS is of no use. A solution allowing to determine the aberrations introduced by CONICA optical elements directly on the science camera itself is therefore the most appropriate. As will be shown in subsection 2.1.3, the PD technique is able to achieve this goal. Once the exact aberrations are known, they can be precompensated through Zernike to slopes basis conversion and addition to the *reference slopes*[6]

[5]Though first designed for adaptive optics wavefront sensing, this method also revealed usable to test optical surfaces. It is based on the fact that a symmetric measurement of the intensity before (intra-focal) and after (extra-focal) the focal plane of the system should give same intensities in the case of a perfect system.

[6]As explained in section 4.1, reference slopes are obtained when calibrating NAOS. We record in a matrix all the

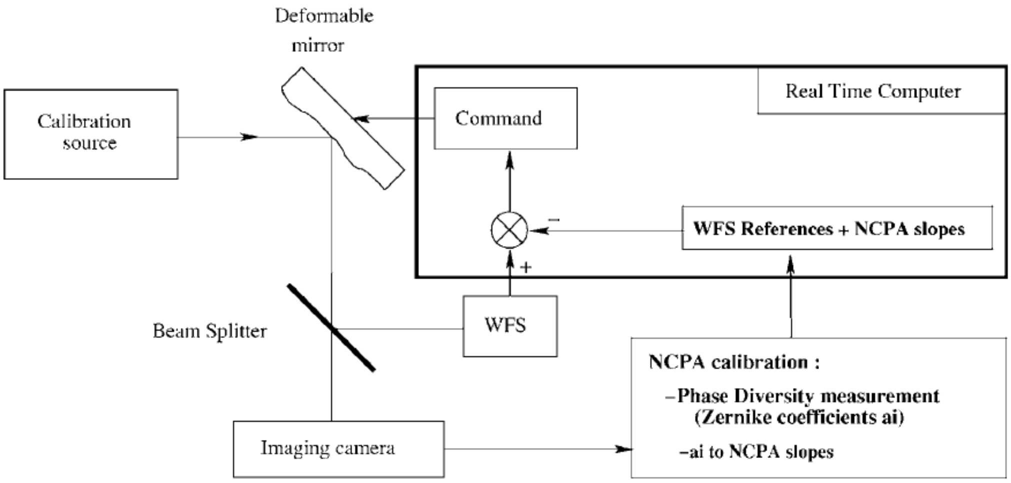

Figure 4: Principle of NCPA precompensation (Sauvage et al., 2007).

(figure 4). In that case, NAOS will not output a true plane wave, but a distorted one that will be flattened after its propagation through CONICA's optical path.

2.1.3 Phase measurement with the PD technique

The main challenge lies in the fact that only intensity measurements can be used to retrieve the phase aberrations. In other words, using the nomenclature introduced in subsection 2.1.1 and expressing the Fourier transform $I(\mathbf{u})$ of an image $i(\mathbf{r})$ with

$$I(\mathbf{u}) = |I(\mathbf{u})| \exp[j\Psi(\mathbf{u})] = FT[i(\mathbf{r})] \tag{4}$$

one wishes to retrieve $\psi(\mathbf{r})$ or equivalently $\Psi(\mathbf{u})$ from measurements of $|I(\mathbf{u})|$ (in the pupil plane) and/or $|i(\mathbf{r})|$ (in the image plane).

A single intensity measurement is not enough to derive a unique value for the phase. Either one has to add a constraint(which typically would be $i(\mathbf{r}) \geq 0$), or a second measurement is needed. Phase diversity corresponds to the latter case, since it consists in taking one intensity measurement in the focal plane and at least one additional image which is defocused by a known phase variation $\phi_d(\mathbf{u})$ (figure 5).

In view of equations (1) and (2), the conventional image and the PD image are respectively expressed by

$$i_1(\mathbf{r}) = |FT^{-1}\{[A(\mathbf{u}).\exp[j\phi(\mathbf{u})]\}|^2 * o(\mathbf{r}) + n(\mathbf{r}) \tag{5}$$

$$i_2(\mathbf{r}) = |FT^{-1}\{[A(\mathbf{u}).\exp\{j[\phi(\mathbf{u}) + \phi_d(\mathbf{u})]\}\}|^2 * o(\mathbf{r}) + n(\mathbf{r}) \tag{6}$$

In our case the phase variation consists only in a defocus term, which in Noll's notation is the fourth Zernike polynomial. We have thus

$$\phi_d(\mathbf{u}) = a_4^d Z_4(\mathbf{u}) \tag{7}$$

centroids shifts on the WFS illuminated by an artificial source's plane WF. The centroids are produced by the WFS lenslet array. The recorded matrix, whose size is therefore $n_{lens}xn_{lens}$, constitutes the so-called *reference slopes*.

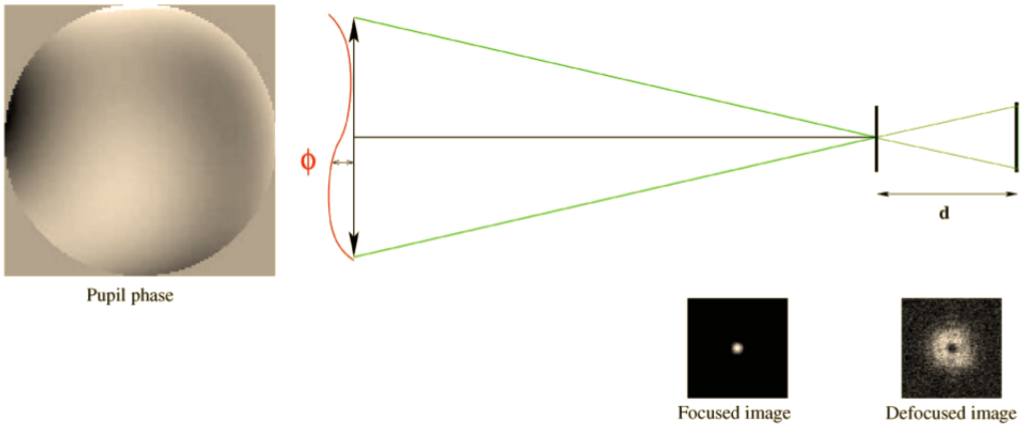

Figure 5: Principle of Phase Diversity (Sauvage et al., 2007).

Because of the spatial sampling of the images, data are actually discrete arrays. Rewriting equations (5) and (6) in their discrete form for both focused and defocused images gives

$$\mathbf{i_1} = \mathbf{H_1 o} + \mathbf{n} \tag{8}$$

$$\mathbf{i_1} = \mathbf{H_1 o} + \mathbf{n} \tag{9}$$

where $\mathbf{i_1}$, $\mathbf{i_2}$, $\mathbf{o}$, $\mathbf{n}$ are the discrete forms of the previous variables and $\mathbf{H_1}$ (resp. $\mathbf{H_2}$) is the Toeplitz matrix corresponding to the convolution by h_1 (resp. h_2)(Ekstrom & Rhoads, 1974).

In summary, measuring $\mathbf{i_1}$ and $\mathbf{i_2}$ and knowing the defocused distance, one needs to estimate the set of aberration parameters a_i (hereafter $\mathbf{a}$), without knowing the object $\mathbf{o}$. In view of equations (5) and (6), there is a non-linear relation between images and aberrated phases, and thereby $\mathbf{a}$. As explained in (Blanc et al., 2003), appropriate mathematical manipulations enable to write a criterion that only depends on the unknown aberrations $\mathbf{a}$ (i.e. not depending on $\mathbf{o}$) and that needs to be minimized. This convergence criterion, whether in the image or in the Fourier (OTF[7]) plane, typically expresses the difference between computed (model) images with measured images.

2.1.4 Iterative algorithm

Once a criterion to minimize has been found, an iterative algorithm is needed for the minimization. Fienup (1982) has shown that for phase retrieval from intensity measurements, error-reduction and gradient search methods are closely related. He also showed the superiority of the conjugate gradient method, whose principle is represented in figure 6.

Both techniques involve iterative Fourier transformation back and forth between the object and Fourier domains and use measured data in each domain as constraints. They can both be summarized by the four following simple steps:

1. Take the Fourier transform of an estimate of the object.
2. Replace the modulus of the computed Fourier transform with the measured $\|I(\mathbf{u})\|$, to create an estimate of the Fourier transform.

[7] Let's remind that the optical transfer function (OTF) is mathematically the Fourier transform of the PSF

3. Take the inverse Fourier transform of the estimate of the Fourier transform.

4. Replace the modulus of the computed image with the measured $\|i(\mathbf{x})\|$ to create a new estimate of the object.

The conjugate gradient method only adds a gradient step between the third and fourth step. In other words, it gives a specific *direction* for the value of the next step, whose exact expression can be found in (Fienup, 1982). The presence of this additive step allows in practice to converge much faster.

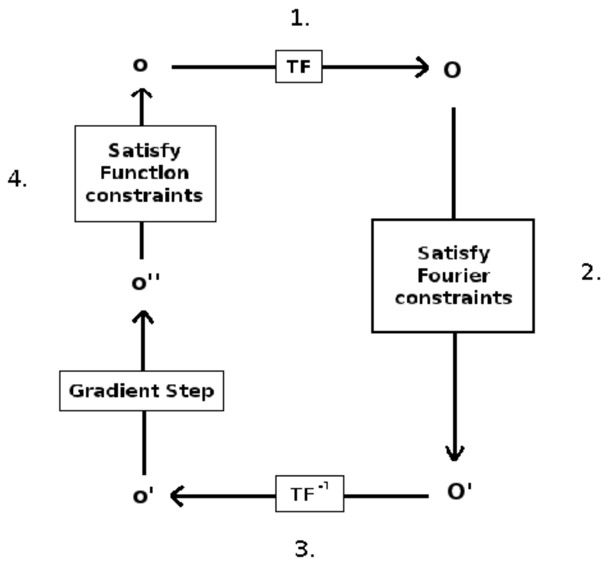

Figure 6: Block diagram of the conjugate gradient algorithm. **o** denotes the object and **O** its Fourier transform. Primes denote estimates.

At each iteration, a new estimate of the object **o** and the images, as well as a new set of aberrations **a** is provided. Finally, the Zernike aberration coefficients are retrieved when the convergence criterion is reached.

The PD technique has already proved its efficiency. Carreras et al. (1994), Kendrick et al. (1994), Lee et al. (1997), Thelen et al. (1999) and Löfdahl et al. (2000) used it successfully in order to retrieve the phase aberrations. The first calibration of the static aberrations of NaCo was logically performed using this technique (Blanc et al., 2003; Hartung et al., 2003).

Another calibration of the static aberrations of NaCo has been performed by mean of the *Nijboer-Zernike* method. This method is similar to the PD technique in the sense that both are based on an iterative process consisting in the minimization of the differences between the model created at each step and the original data. The differences occur both in the fact that the minimization is performed directly on the images (instead of occurring in the OTF plane) and in the process used to determine these aberrations (PSF expanded in modes, themselves expanded in the aberrations). A detailed overview of the Nijboer-Zernike method, its adaptation to NACO's static aberration retrieval and the results of the treatment can be found in A. Magette's PhD thesis (Magette, 2010). Let's emphasise that this implementation directly used science images instead of calibration fibre source's ones.

The PD software that I used during this internship was *OPRA*, described in subsection 4.3.

2.2 AO's figures of merit

2.2.1 Strehl ratio

The *Strehl ratio* (hereafter Sr) is defined as the peak intensity of a measured PSF to the peak intensity of a perfect diffraction limited PSF for the same optical system:

$$Sr = \frac{I(\mathbf{x}=0)}{P(\mathbf{x}=0)} \tag{10}$$

where $\mathbf{x}$ stands for the position vector, $I(\mathbf{x}=0)$ for the maximum intensity of the measured PSF and $P(\mathbf{x}=0)$ for the maximum of the diffraction limited PSF (Strehl, 1901).

The Maréchal approximation gives an alternative definition based on wavefront errors:

$$S = \exp[-\sigma_\phi^2]\exp[-\sigma_\chi^2] \tag{11}$$

where σ_ϕ^2 is the wavefront phase variance and σ_χ^2 is the variance of the log-normal amplitude at the pupil plane (Marechal et al., 1994). It is valid when the Sr $> 10\%$ or $\sigma_\phi^2 < 2.3$. A consequence of the Maréchal approximation is that the total Sr of an instrument is the product of the Sr of its n individual optical elements as long as the phase errors of each component are uncorrelated (ie: $\phi = \phi_1\phi_2...\phi_n$).

In view of its definition, the Strehl ratio has been widely used as the main figure of merit to quantify the performance of AO systems. However, in a more general context than AO, it can be used to estimate the quality of any image.

As shown by Roberts et al. (2004), different techniques can yield significantly different computed Sr. This is accounted for subtle differences from a technique to another, such as the equation it is based on (10, 11 or 15), the way it computes the theoretical diffraction pattern of the instrument, or the way it normalizes the latter with the photometric measurement.

Since there is no perfect method, the Sr related to images that were taken during our calibrations (section 4) were computed through 5 different techniques: the algorithm used by the *ESO pipeline* (hereafter method 1), the one used by *OPRA* (hereafter method 2), the *MAD Strehl meter* (hereafter method 3), the *MVD Strehl meter* (hereafter method 4) and finally the *OTF Strehl meter* (hereafter method 5). In this way, conclusions that will be drawn in section 4 from the comparison of the Sr values obtained with the different methods will not be biased by the computing technique used.

The specificities of these techniques are presented in subsection 4.4 as well as corresponding error bar estimates in subsection 4.5.3. A first classification consists in distinguishing methods computing the Sr thanks to image plane data and the ones computing it in the Fourier plane.

Computation in the image plane (methods 1, 3 and 4) The first group of computation techniques are based on equation (10). It first consists in obtaining the diffraction pattern, which is specific to the pupil shape of the telescope used. It can be created either analytically with the equation for a centrally obscured circular aperture[8], or numerically by using Fourier optics. The analytical computation is used by methods 1 and 3, whereas method 4 uses the numerical one.

Most of the time, the diffraction pattern will be computed numerically if the pupil is not a perfect centrally obscured circular aperture. For example, algorithms used at Keck observatory, as the one developed by Marcos van Dam, compute numerically the diffraction pattern. This

[8]
$$P(\nu) = \frac{2J_1(\nu) - 2fJ_1(f\nu)}{(1-f^2)^2\nu^2}$$
with J_1 the Bessel function of order 1, f the fractional obscuration, and $\nu = \theta\pi D/\lambda$, where θ is the off-axis angle.

computation needs a binary mask, representing the shape of the pupil. This mask is then Fourier-transformed. By definition, this Fourier transform is the complex wavefront at the focal plane of the instrument. The diffraction pattern is then obtained with the modulus squared of the complex amplitude.

The second step is to scale the diffraction pattern to the energy of the PSF in order to have the same total intensity as the PSF. This normalization is often realized by summing all the energy in a region centered on the PSF peak. The main issue is regarding the size of this region. It must be large enough to contain all the energy of the PSF, but not to encompass pixels with pure noise.

The Sr is then the ratio of the peak intensity of the PSF divided by the peak intensity of the diffraction pattern, as stated in equation (10). The measurement of the peak intensity is usually achieved taking the value of the peak pixel, or at least, if the maximum is not falling on a single pixel (which is the most probable), an interpolated value of it.

Computation in the focal plane (method 5) The second main group of computation techniques uses the equivalent of equation (10) in the Fourier (OTF) plane:

$$S = \frac{\int OTF_{PSF}(\mathbf{u})\mathrm{d}\mathbf{u}}{\int OTF_{diff}(\mathbf{u})\mathrm{d}\mathbf{u}} \tag{12}$$

where $OTF_{PSF}(\mathbf{u})$ is the optical transfer function of the image, $OTF_{diff}(\mathbf{u})$ is the OTF of the diffraction limited optical system and $\mathbf{u}$ is the spatial frequency domain vector. In this definition, we assume the maximum value of the PSF is located at $\mathbf{x} = 0$.

Compared to the first type of computation, OTF-based computations present the possibility to filter high-spatial frequencies in the Fourier plane (e.g. frequencies higher than the diffraction limited cut-off frequency, which correspond to pure noise).

2.2.2 The rms of Zernike coefficients

In the field of direct imaging and high-angular resolution, what need to be minimized are the speckles. Their significance, of course, is linked to the Sr since the energy that is not located in the central peak is located in the speckles. In other words, the speckles are proportional to 1 - Sr.

However, it should be noted that the Sr is just a number, and as it appears normal to use this ratio as a figure of merit, one should keep in mind that it does not give the repartition of the lost energy out of the Airy diffraction pattern (i.e.: in the speckles). As mentioned in section 2.1, the exact phase aberrations are fully characterized in the Zernike coefficients base. Therefore a more appropriate figure of merit is the rms of the high-order Zernike coefficients ($i \geq 4$), which has to be minimized.

As a reminder, the rms value of a set of values $a_1, a_2, ..., a_n$ is the square root of the arithmetic mean of the squares of the original values:

$$a_{\mathrm{rms}} = \sqrt{\frac{1}{n}(a_1^2 + a_2^2 + ... + a_n^2)}$$

In consequence, this definition is particularly interesting for a set of both positive and negative values, such as the computed Zernike coefficients. We used this value in the last column of all our **plots** in section 4.5 and 4.6.

However, we insist on the distinction between the above-defined *coefficients rms* and the phase standard deviation σ_ϕ which is *expressed* in nm rms, σ_ϕ^2 being the aberrated phase variance. In the context of PD, this σ_ϕ is usually referred to the *rms*. Therefore, all values of *rms* given in the **tables** of section 4 are the phase standard deviation σ_ϕ.

3 NaCo Instrument

NaCo instrument is mounted on the Nasmyth B focus of VLT UT4 telescope. It is a combination of two instruments: NAOS and CONICA. NAOS is the AO unit, which provides compensated images to the science camera CONICA in the 1 to 5 μm spectral range (ie: from J band to M band[9]). Figure 27 (appendix C) shows the two instruments, we see that NAOS constitutes the front end of NaCo (ie: the first in the light path coming from the telescope), while CONICA is placed at the rear end.

NAOS input beam is the UT4 F=15 Nasmyth focus beam, which is an unvignetted *field of view* (hereafter FOV) of 2 arcmin in diameter. Since the telescope is tracking during the night, so would do the FOV that is observed. To compensate this effect, NAOS is thoroughly attached to a Nasmyth adapter-rotator (figure 28, appendix C) which rotates around the altitude axis of the telescope, and CONICA is directly attached to NAOS.

3.1 Some history

The technical feasibility for the VLT Coude AO (4 AO systems) was first studied in February 1991, then in 92-93 by Matra-Marconi-Space, but the project got cancelled in December 93. In the meantime, the CONICA contract was signed with MPIA et al. in 1991. After the cancellation of the VLT Coude AO project, the NAOS concept is proposed by ESO to STC-FC-Council by the end of 94. At the same time, CONICA is redesigned by MPIA et al. After a preliminary inquiry between December 94 and March 96, and an audit from March 96 to December 96, the contract for NAOS was signed with ONERA (French Aerospace Lab) et al. in March 97. The Final Design Review (FDR) for CONICA was then realized by mid 98, as the one for NAOS finished by June 99.

NAOS-CONICA then got the Preliminary Acceptance in Europe (PAE) in September 2001, and the first light was shed in November of the same year. The next months, until March 2002, NaCo has been commissioned at the VLT and first on sky results and performances in terms of Strehl ratio, seeing conditions and guide star magnitude were revealed. As Rousset et al. (2003) tested the instrumental performance for several direct imaging modes, Lenzen et al. (2003) focused on slit-spectroscopy, polarimetric and coronagraphic modes.

The third and final commissioning run of NaCo took place for the period March 22 to April 4, 2002. The on-sky acceptance tests of NaCo were then completed in May 2002 and the instrument eventually became available to the European astronomical community in October of the same year.

3.2 NaCo Operations and responsibilities

3.2.1 Operations overview

NaCo operations are composed of a large part of calibrations and maintenance checks, which take place during the day. The instrument can then be devoted to science or calibration observations at night. Table 11, (appendix C) gives a detailed list of NaCo operations, with a short description.

3.2.2 Responsibilities overview

A proper distribution of the responsibilities is required in order to operate efficiently a facility such as Paranal Observatory. A description of the main actors and their respective responsibilities is given in table 12 (appendix C).

[9]The exact division of the different IR bands is given in figures 26 and table 10, in appendix C.

3.3 NAOS

NAOS is the first AO system installed at the VLT 8m telescopes. The acronym stands for Nasmyth Adaptive Optics System. It has been designed by a consortium of four different institutes: ONERA (which was the general contractor), LAOG[10], ODP[11] and ESO (which financed the construction and participated to several subsystems). The total cost of this 5-year project came to 5 million euro.

NAOS provides a turbulence-compensated F=15 beam in a 2 arcmin FOV to the astronomical instruments. Figure 29 (appendix C) shows an outline of NaCo including the optical train in NAOS adapter. Let's first notice the two off-axis parabolas, which allow to reimage the telescope pupil on the DM and the Nasmyth focal plane at the entrance focal plane of CONICA. Subsequently in the light path direction, there is the *tip/tilt mirror* (hereafter TTM), the DM, the second off-axis parabola and the dichroic plate which splits the light in reflection toward the WFS and in transmission toward CONICA. An atmospheric dispercion compensator (ADC) can be inserted between NAOS and CONICA in case of high zenith angles.

NAOS adapter, represented at figure 28 (appendix C) carries the optical train explained above, along with the two WFS units and the front-end electronics, which are both not represented on figure 29. This same adapter also holds CONICA. Therefore, during the rotation, the gravity load of both instruments induces flexures of the optical elements inside them and of the CONICA flange. The differential flexures between the WFS detectors and the CONICA detector are actually the most critical issue to deal with. Using calibrated pointing models, the AO loop pre-compensates for these flexures. The current residual differential flexure is of the order of $\sim$15 mas per 180° rotation.

3.3.1 Tip-Tilt and Deformable Mirrors

The overall WF tilt fluctuations are compensated by the TTM. The higher orders fluctuations are compensated by the DM. Figure 30 (appendix C) represents both instruments.

The TTM was manufactured by the Observatoire De Paris. It is equipped with four voice coil[12] actuators working in push-pull, which then allows to incline the mirror along two-axis (*tip* and *tilt*). The mirror itself is 50 % light-weighted. On sky, the angular range is 13 arcsec *peak-to-valley* (hereafter PV) per axis and the resolution 2.1 mas rms.

The DM was manufactured by CILAS (France). It is composed of a *continuous* facesheet mirror above 185 active stacked actuators (piezo-electric material). These actuators are arranged on a square array in a 110 mm diameter pupil image. The total stroke of the WF is 20 μm PV, with a WF error at rest lower than 2.0μm PV. It is then easily corrected in closed-loop. As an order of magnitude, the non-correctable high spatial frequency static aberrations at the time NAOS was commissioned were already lower than 30nm rms (Rousset et al., 2000).

3.3.2 Dichroics and beam splitters

Three dichroics and two neutral BS are offered in NaCo. They allow to choose one out of five possible combinations for the spectral bands going in the WFS unit with the ones that go in the science instrument (table 13 in appendix C). As can be seen in the table, the transmission is very high for all the dichroics ($\sim$ 90 %).

[10] Laboratoire d'Astrophysique de l'Observatoire de Grenoble.

[11] Observatoire de Paris.

[12] This means that the actuators work with the same principle as the coil in a loudspeaker: covering a permanent magnet, the coil is moved by the Laplace force $\mathbf{F} = I\mathbf{l} \times \mathbf{B}$ when a current is going through it, pushing then the diaphragm.

3.3.3 Wavefront sensors

The WFS channel includes the *field selector* (hereafter FS), the WFS selector mirror and the two WFS units: one infrared (0.8-2.5 μm) and one visual (0.45-1.0 μm) Shack-Hartmann WFS.

The role of the FS is to select the *natural guide star* (hereafter NGS) for WF sensing in the 2 arcmin FOV. It allows moving guide object tracking, differential refraction and precalibrated flexure compensation. It is placed at the entrance of the WFS channel and is actually composed of two parallel tip-tilt mirrors (FS1 and FS2). These TTMs work in close loop to achieve a very high angular stability. They were manufactured by CSEM (Switzerland) (Spanoudakis et al., 2000).

Both visible and infrared Shack-Hartmann WFSs include two lenslet array pupil samplings: 14x14 (144 valid subapertures) and 7x7 (36 valid subapertures). The reason of the choice between two different samplings is to cover a wider magnitude range. The 7x7 configuration allows to achieve a substantial correction with faint NGS while the 14x14 subaperture configuration is more adapted for bright NGS.

The characteristics of the visible WFS (VWFS) and its camera, as well as those of the infrared WFS(IRWFS) and its camera are summarized in table 14 (appendix C). The VWFS camera was manufactured by ESO (Gerdes, Beletic, & Duvarney, 1998), as the IRWFS camera is equipped with a Rockwell Hawaii array[13].

3.3.4 Performances

The level of correction in AO systems depends on a large number of factors, such as seeing, speed of the turbulence (τ_0), airmass, brightness and morphology of the reference object, angular distance between the reference object and target, and instrument performance.

As shown by tests during the commissioning periods (Rousset et al., 2003), NAOS can provide Strehl ratios as high as 50 % in the K band for a point-like reference source with a visual brightness of V=12 (figure 31, appendix C). It was also proven that it still provides partial correction for targets as faint as V=16.7 or K=12 (13 with the N90C10 dichroic). UT4, as well as the other UTs, has a diffraction-limited resolution of $\lambda/D = 0.057$ arcsec at $\lambda = 2.2\mu$m. Rousset et al. (2003) achieved this limit during the commissioning period.

3.4 CONICA

CONICA is a high angular resolution IR science camera, which is fed by NAOS. The acronym stands for COudé Near-Infrared CAmera. It is constituted of a Santa Barbara Research Center (SBRC) detector, an InSb 1024x1024 array called *Aladdin 3* (2005 upgrade of the original *Aladdin*), which is sensitive in the 0.8 - 5.5 μm wavelength range. Its readout modes with their allowed saturation levels are summarized in table 15 (appendix C).

Numerous modes have been defined, since the commissioning of NaCo, in order to match the different types of science that can be realized. CONICA is able to perform imaging, polarimetry, coronagraphy, spectroscopy. Special modes such as cube mode, pupil tracking or NoAO are also compatible. New modes are commissioned at the beginning of each new *period*[14], at the same time old ones may be decommissioned.

The position of the different wheels (mask, grism/polarimetry, filter) enabling the different types of science can be found, among other optical elements, in figure 32 (appendix C) representing a

[13] More details about this type of IR sensor at http://www.not.iac.es/instruments/detectors/swir1/hawaii/hawaii.html .

[14] The periods correspond to a length of one semester each. E.g. P88 was from October 1st, 2011 to March 31th, 2012 and P89 has started from April 1st, 2012, lasting until September 30th.

detailed view of CONICA. In the framework of my task, the only wheels that I had to "turn" was the two filter wheels.

Since the purpose of my work only needed the use of basic imaging, we do not describe the abundant other modes. The interested reader should refer to (Girard, 2011).

3.4.1 Imaging

The different objectives of CONICA allows a correct sampling of the telescope diffraction limit in the 1 - 5 μm wavelength range. Their characteristics, such as wavelength range, pixel scale, FOV and filter sampling, are presented in table 16 (appendix C). Orders of magnitude of the sky background and the limiting magnitudes of NaCo in the different infrared bands are given in table 17 (appendix C).

As shown in figure 32 (appendix C), CONICA has several filter wheels placed in the light path. They allow a large choice of broad, intermediate or narrow band filters, which cover the range 1 - 5 μm. They are described in table 18 (appendix C). Please note that in order to observe very bright objects without coronagraphic mask, it is also possible to insert a neutral density filter, reducing the intensity by a factor of 80 ($\lambda < 2.5$ μm) or 50 ($\lambda > 3$ μm).

3.5 Science niches

Characteristics of NaCo make it a state-of-the-art instrument in the field of high-resolution and high-contrast imaging and spectro-imaging. As a matter of fact, it provided several *premieres* in exoplanet science and galactic center science to name but a few.

3.5.1 Exoplanet science

Since the discovery of the first exoplanet (Mayor & Queloz, 1995), a lot of others have followed. Most of those were indirectly detected by the so-called radial velocity method. Other indirect techniques such as transit, pulasar timing or gravitational microlensing have also borne fruit. In this context, the first exoplanet detection by direct imaging was realized thanks to data taken with NaCo (Chauvin et al., 2005). The exoplanet was found around a brown dwarf (2M1207b).

Since then, NaCo also allowed first direct motion monitoring of an exoplanet, Beta Pictoris b (Lagrange et al., 2010) and the first direct spectroscopic re-detection of an exoplanet in the 4μm domain, HR8799 c (Janson et al., 2010).

NACO-SDI mode[15], followed by its successors SDI+ and SDI+4 modes, was expected to boost low-mass methane-rich companions detections. So far, the different studies that have been carried out led to ambivalent results. Around tens of either close young stars (Biller et al., 2007), or solar type stars possessing known brown dwarfs (Jenkins et al., 2010) surveys have been disappointing since they led to null results. The closest known extrasolar planet, orbiting around the active K2 V star ϵ Eri, has also been the subject of an unsuccessful re-finding attempt (Janson et al., 2007). However, not all studies using NACO-SDI have not borne fruit, the detection of the Sun second closest brown dwarf is a remarkable counter-example (Biller et al., 2006), as well as the discovery of 16 brown dwarf companions around G and K dwarfs (Montagnier et al., 2007).

[15]SDI (Simultaneous Differential Imager) is a special imaging mode of NaCo. It produces four images of the same object into CONICA, within three different narrow-band filters surrounding the 1.62 μm methane bandhead. Two images are taken outside the methane feature, at 1.575 and 1.60 μm, and two images are taken inside the feature, both at 1.625 μm).

3.5.2 Galactic center

During more than ten years, the team led by R. Genzel (Max Planck Institute for Astrophysics, Garching) had been observing the galactic center until 2002. That year, using the freshly commissioned instrument NaCo in order to reach higher sensitivity (by ~ 20) and angular resolution (by ~ 3), the team discovered the closest star orbiting Milky Way's supermassive black hole (Schödel et al., 2002).

A few years later, the combination of NaCo Wollaston prism[16] with its half-wave retarder plate[17] brought other interesting results. Observations of the flares from Sagittarius A* with the polarimetric mode of NaCo favored a jet or temporary disk model, at the same time ruling out a boson/fermion ball model (Eckart et al., 2006).

In 2009, Schödel et al. determined the proper motions and mass of the nuclear star cluster of the Milky Way from a combination of former and new data taken in Ks with NaCo. It is the first time that the extended mass of the nuclear star cluster is unambiguously detected.

The efficiency of SAM[18] in galactic center science has also been confirmed. Sanchez-Bermudez et al. (2012) used SAM to image successfully the circumstellar environment of several bright sources with infrared excess in the central parsec of the Galaxy.

3.6 User's interface

At Paranal observatory, all the directives are given to the instruments from the control room. Each of the four UTs has a dedicated space in it, and each of these dedicated spaces has different monitors allocated to different instruments mounted on the same UT. The orders sent from these monitors take the shape of either Observing Blocks (hereafter OBs), Phase II Proposal Preparations (hereafter P2PPs) or instructions directly given from the different control panels of the instrument.

On one hand, OB's and P2PPs are both scripts containing blocks of instructions, and are read with the Browser for Observing Blocks (BOB, figure 33, appendix C). On the other hand, the SOS control panel allows to setup the instrument directly, control the active tasks, check the real-time performances of the AO system, apply some offsets. Since P2PPs are the blocks of instructions that correspond to observations at night, only OBs and control panels were handled during my work.

The main control panel of NaCo is the so-called Super Operating System (SOS hereafter), described in figure 34 (appendix C). It is used to setup the instrument, check the real-time performances of the AO (seeing, coherence, Sr), control the active tasks, apply additional offsets. It is roughly splitted in three main panels: CONICA, NAOS and LGS. The options available for NAOS and CONICA in the SOS panel can also be reached in the respective ICS control panel of both instruments. The latter one is shown in figure 35 (appendix C).

[16] A Wollaston prism is an optical device used for polarimtery. Composed of two cemented calcite prisms which are orthogonal to each other, it separates any light beam (polarized or unpolarized) into two orthogonal linearly polarized outgoing beams. It is thus a polarizer.

[17] A wave plate is an optical device capable of altering the polarization of light. Contrarily to the effect of a polarizer, the polarization state of the outgoing beam depends of the polarization state of the incoming beam. A birefringent crystal constitutes a typical wave plate.

[18] Sparse aperture masking mode consists in special aperture masks that are placed in the pupil plane, in order to obtain the very highest angular resolution at the diffraction limit.

4 Calibration of the NCPAs

If the NCPAs are not perfectly calibrated, they result in quasi-static speckles. Quasi-static speckles reduce sentivity and resolution. Subsequently, they also degrade the Strehl ratio. In the framework of exoplanet research for example, they can not easily be distinguished with faint companions in long-exposure images. Their fluctuation timescale depends on both environmental changes (e.g. temperature) and instrument gravity vector. Although new techniques treat more and more efficiently the residual speckles (see e.g. the modified LOCI-algorithm in my master thesis, (Lafrenière et al., 2007) or (Crepp et al., 2011)), the calibration of the NCPAs should definitely not be neglected. It erases more speckles at the starting point, and as for extreme high-contrast and high-resolution imaging, these speckles are very important to shed.

4.1 Original NaCo calibrations

As mentioned in subsection 2.1.4, the original calibrations were performed by Blanc et al. (2003); Hartung et al. (2003). The procedure used dealt separately with the NAOS and CONICA NCPAs, and furthermore in an element-by-element approach. Since this process is technically cumbersome, a lighter calibration procedure that could be performed on a regular base is needed.

The layout of the original procedure consisted in calibrating as accurately as possible the NAOS NCPAs before the CONICA NCPAs. As for NAOS, the *WFS artificial source* (hereafter WFSAS) located in front of the FS illuminated each WFS, hence allowing the detection of wavefront distortions due to NAOS. Low-order term aberrations (tip/tilt/defocus) are corrected by moving the FS (figure 7), whereas the high-order terms are converted and recorded as *reference slopes*. These reference slopes constitute a matrix composed of each centroid's shift (i.e. *slopes*) on the WFS camera, the centroids being produced by each WFS microlens array (figure 8).

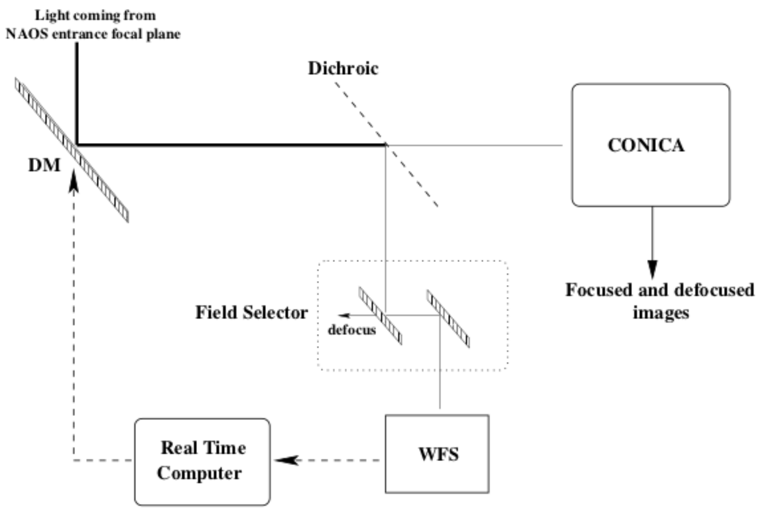

Figure 7: Principle of the low-order aberration terms correction through the FS (Hartung et al., 2003).

As for CONICA, the aberrations were calibrated thanks to a special external fiber source. The mounting of the external lamp with the appropriate tool involves the removal of the calibration sphere. In addition to the testing of the different setups (10 minutes each), two hours are required

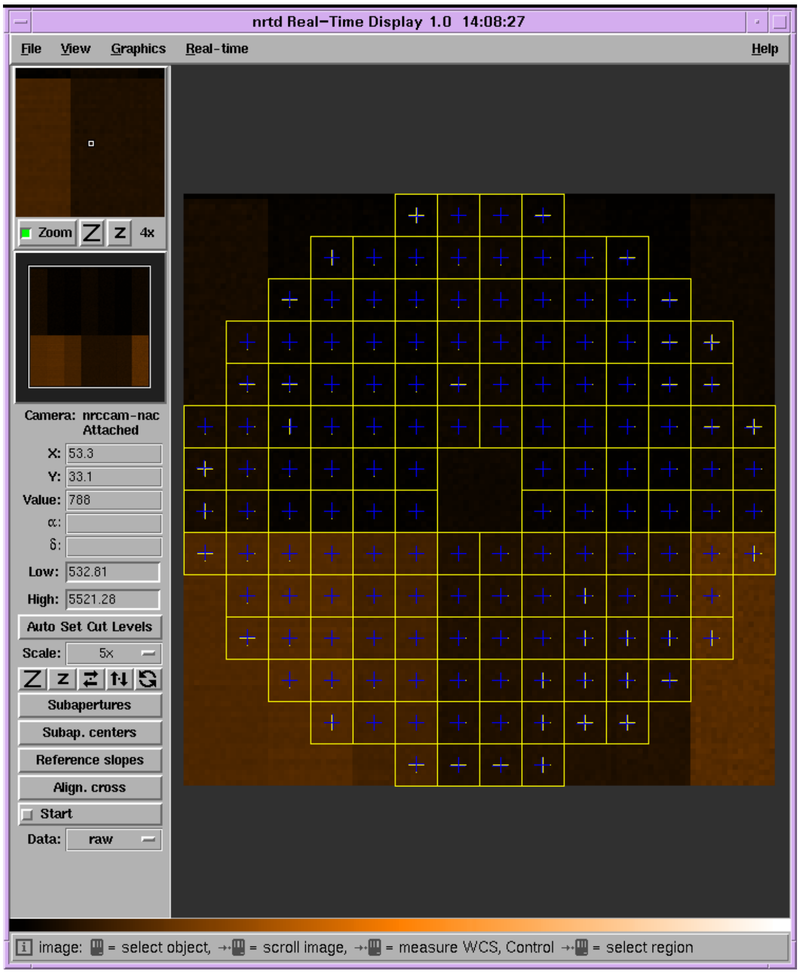

Figure 8: Reference slopes, as seen in the Real Time Display (RTD). The blue crosses are the deviation compared with the center of each square (yellow crosses). When there is no shift, the blue cross is exactly overwriting the yellow one.

to dismount and remount the sphere, and to recheck the alignment of the calibration sphere. This is the reason why the original procedure is considered cumbersome.

The calibration also required the so-called *Zernike tool*. It is a wheel composed of different pinholes, placed at different axial distances starting from the entrance focal plane, and allowing a focus diversity of the resulting images. Eventually, aberrations were computed both for each individual element of CONICA and each dichroic through an IDL-based PD code.

4.2 New calibration procedure

Tests with the new PD software *OPRA* were carried out in October 2011 and yielded promising results. Summarized hereunder, they were extensively used to draft a new calibration procedure (O'Neal, 2012) much lighter than the original one . Instead of a setup including an external source and the Zernike tool, PSF/LED/IM fiber sources in NAOS were this time used in a compatible way to measure CONICA NCPAs with the PD software. The empirical results include:

- Little difference in static aberrations between the S13 and S27 objectives (to be quantified).
- As for other objectives, the generated PSF will probably be too undersampled to allow the proper running of OPRA (to be quantified).
- Little difference in the high-order aberrations between the different filters (to be quantified). The likelihood is that there exists a common set of aberrations for the different CONICA filter setups (including collimator and objective aberrations).
- The NAOS NCPAs are very dependent on the WFS setup tested, particularly between VIS/IR, VIS/LGS and IR/LGS.

Since NAOS and CONICA NCPAs are summed and compensated as one by the DM, it seems appropriate to combine them as one set in the configuration files instead of considering them as separate sets. However, the current configuration scheme in NaCo's software is not compatible with this solution.

Based on the aforementioned results, a new NCPA calibration procedure optimized for efficiency and simplicity, has been proposed for the instrument. Realistic software and instrumentation resource allocation has been favored instead of ultimate performance in order to maximize the performance improvement / effort ratio.

The calibration procedure focuses on the reference mode of NAOS (VIS 14x14). On the one hand, it ensures that the NAOS NCPAs are correctly removed in close loop, on the other hand the system will also be roughly calibrated for the other modes. The plan consists first in a regular NAOS maintenance, a mandatory step before second the application of the NCPA calibration scheme.

4.2.1 Regular NAOS maintenance

Prior to any calibration of the instrument, the four NAOS calibration sources (IM lamp, PSF lamp[19], WFSAS lamp and LGS IM LED) have to be themself stable and well-calibrated towards the instrument. To be certain that it is indeed the case, NAOS calibration units should be measured on a regular basis and the results plotted. Without this insurance, no reliable calibration can be undertaken.

The following OBs are used to monitor NAOS calibration sources.

- `WfsTipTilt` confirms for each WFS in NAOS that the FS *home* position is well-calibrated in order to acquire the IM fiber. It is equivalent to the determination of the Tip/Tilt NAOS NCPA.
- `AlignPSF` confirms for each WFS in NAOS that the FS *home* position is well-calibrated in order to acquire the PSF fiber. The PSF and IM fibers should appear to the WFS to be at the same position in the image plane.
- `FocusPSF` and `FocusOffsetPSF` confirm that PSF and IM fibers are conjugated and that the distance between LED and PSF fibers along the optical axis is correctly calibrated in NAOS.
- `CheckFocus` calibrates the defocus aberration of the NAOS NCPA for each dichroic.

Figure 9 provides a simplified view of NaCo and its calibration sources. More details about both calibration sources and OBs can be found in (Lidman, Ageorges, & Soenke, 2009).

[19] This lamp is composed of two sources, a lamp fiber almost on axis and an off axis LED.

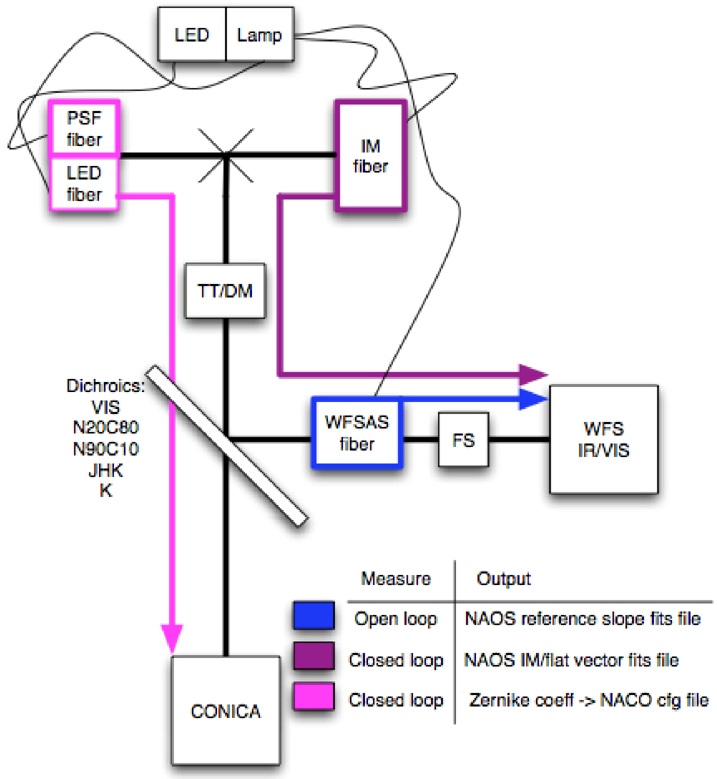

Figure 9: Block diagram of NaCo. Main elements of NaCo are represented, along with the different calibration paths (colored arrows). The blue arrow shows the optical path of NAOS, whose open loop WFS data is saved as the *reference slopes*. The purple arrow is the IM fiber calibration path, it is used for many AO calibrations (including the computation of IM and flat vector files). The magenta arrow represents the proposed calibraton path for closed-loop CONICA NCPAs measurements.

4.2.2 New NCPA calibration scheme

Considering stable calibration sources, it is possible to perform the procedure described hereunder. In the case of satisfactory results, it could be performed sporadically or after all interventions on NaCo or even, if the execution efficiency allows it, on a more frequent (weekly/daily) basis. As aforementioned, the first part of the procedure deals *only* with the reference mode of NAOS (VIS 14x14). Figure 9 provides a graphical representation of the three first steps.

1. NAOS reference slopes - Using the WFSAS, measure the high-order NAOS NCPAs for the VIS 14x14 mode.

2. Interaction matrices - Using the IM fiber, measure the IM for the VIS 14x14 mode. IMs are the conversion matrices from voltages to *slopes* (i.e.: pushing actuators of the DM, we note the effect on the centroids position on the WFS).

3. CONICA NCPA - Using both `cnstooTakePDData` and OPRA, determine the set of high-order aberration coefficients (a_i, $i \geq 5$) common to CONICA setups, with the NB filters and

with the VIS 14x14 NAOS mode. This step was the specific task that was assigned to me, and whose details, results and encountered difficulties are described in sections 4.5, 4.6, 4.7.

4. Configuration files update - Assuming the different objectives present approximately the same aberrations, apply previous step's results to all camera objectives in the configuration files.

5. Focus optimization - Time permitting, estimate the defocus term (a_4) for each filter by taking inter- and extra-focal images[20]. If not, take the rough estimate of a_4 given by OPRA. This value will serve as the new defocus term for the aberration configuration file of the filter.

Time permitting, all the individual filters should be tested with the `cnstooTakePDData` script and OPRA combination. Each time, the resultant aberration coefficients, specific to the filter used, are added to the current coefficients in the corresponding configuration file. At this stage, the system is now calibrated for the visible WFS modes, and is roughly calibrated for the others. The next logical step is then the extension of this procedure to the IR WFS.

1. NAOS reference slopes - Using the WFSAS, measurement of the high-order NAOS aberrations for the **IR** modes.

2. Interaction matrices - Using the IM fiber, measurement of the IM for the **IR** modes.

3. CONICA NCPA - Using both `cnstooTakePDData` and OPRA, determination of the set of aberration coefficients for the **IR** dichroics. However, as referenced in table 13 (appendix C), some of the dichroics transmit a very faint portion of the incoming light to CONICA, performing PD on these elements may thus be harder.

4. Iteration - Iteration of the last three steps in order to reach (in all likelihood) the desired quality of PSF on CONICA.

5. Configuration files update - Addition of the OPRA results to the dichroic's current values in the corresponding configuration file.

At this stage, the system is now calibrated both for the VIS and IR WFS modes. The LGS mode requires similar actions.

4.2.3 Action items

The required tasks in this new calibration procedure are distributed in the following way:

- Alteration of the NaCo daily calibration procedure so that NAOS data is taken as per subsection 4.2.1: D. Mawet, J. O'Neal, N. Slusarenko.
- Addition of the above results plots to AUTREP (ESO's only database): J. O'Neal, N. Slusarenko.
- Optimization, automation and testing of the CONICA NCPA calibration with the new PD software OPRA: D. Mawet, J. Girard, J. O'Neal and V. Christiaens.
- Wrap-up and update of wiki page, operations manual and maintenance plan: all.

[20] As a matter of fact, the sole variation of focus from intra- to extra-focal on the images does not enable the exact determination of the a_4 term because of an *insensitive region* spanning the range several tens of nm intra-focus (compared to the truth focused image) to several tens of nm extra-focus. The trick lies in the deliberate introduction of some astigmatism (a_5) in the image. We then make the defocus term vary until the pattern that is seen becomes perfectly symmetrical, which is what should be obtained assuming that the high-order aberrations are properly corrected. This method, although time-consuming, allows a more accurate determination of a_4.

4.3 OPRA

OPRA is a program written in *Yorick* language[21] that was developed by F. Rigault, B. Neichel and D. Gratadour within their work on the GEMINI MCAO system. The acronym stands for OTF-based Phase Retrieval Algorithm. As its name indicates, it performs the minimization of the criterion in the OTF (or Fourier) plane, instead of the PSF (or image) plane.

In subsection 2.1.4, we presented the formalism of the PD technique using the Zernike basis. Other basis exist to expand the phase. *OPRA* offers the choice between disk harmonic (default), Karhuenen-Loeve or Zernike. Original OPRA code needs to be fed with 4 PSFs, 1 focused and 3 defocused. However, the code being flexible, it was also possible to test the performance of it with only 3 PSFs (1 focused and 2 defocused) as will be shown in subsection 4.3.1.

A useful *OPRA caller* allows to indicate the files that have to be used. It also performs basic operations on the input images, *calls* OPRA function and plots the result. The detailed code of this *OPRA caller* is attached in Appendix B. We summarize hereunder the operations that it realizes:

Definition of variables: both image and corresponding background path and file name, corresponding DITs and defocus for each image.

Preparation of the four images: background subtraction, image centering (or crop), filtering of the pixels that deviate from the local statistics (sigma filtering), set of the minimum value to 0 (clipping) and normalization.

Noise evaluation: rms of the pixel values in a corner of the focused image.

OPRA call: the OPRA function is called with the following arguments, *opra*(images, defocuses, wavelength, pixel size, telescope diameter, central obscuration ratio, number of modes, noise, mode base, keyword for a fixed amplitude during the computation, keyword for a slower introduction of modes than regular version, printout mode coefficients in nm).

Computed coefficients: are in opp.coefs.

Display: Opening of a new window and plot of the computed Zernike coefficients.

In the OPRA call, please note that wavelength, pixel size, telescope diameter and central obscuration ratio are only used to get a starting value for the pupil diameter (in pixels), which is also used as a constraint during the iterative algorithm.

Figure 10 shows the different windows opened while running OPRA. OPRA caller is called from a basic terminal window (providing the path for the Yorick directory). When it calls the OPRA function, the latter opens a new window (*Yorick 0*) showing in real time its computations. The upper part of the window displays the model images and data images, it helps to visualize the aberrations in the image plan. As mentioned above, the minimization is actually performed in the OTF plane. Data, model and drift in the OTF plane are displayed in the lower-left part. A phase map corresponding to the aberrations is drawn at each iteration, similarly a Strehl ratio estimate is given (right part). Finally, the lower-right part displays the distance to data at each iteration. The algorithm stops when the convergence threshold is reached ($3.74\ 10^{-3}$).

As aforementioned, back in OPRA caller, a new window is opened, plotting the additive inverse of the final computed high-order Zernike coefficients (*Yorick 1*). In other words, it displays the opposite values of the phase aberration coefficients that characterize the wavefront. These opposite values are useful (or more precisely their half values) because they correspond to the correction that needs to be performed by the DM. Their initial value (non multiplied by -1) is also displayed in the terminal for convenience (lower-right part of figure 10).

[21] More details about Yorick language available at http://www.maumae.net/yorick/doc/index.php

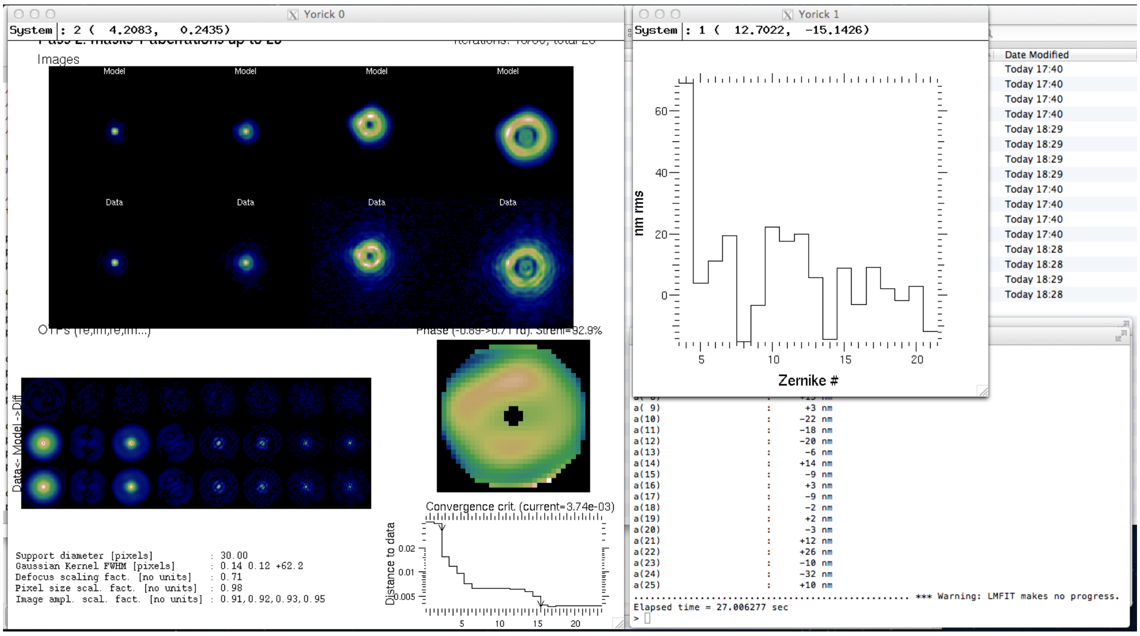

Figure 10: A typical OPRA session.

4.3.1 Effect of a different number of PSFs used by OPRA

Optimization of the procedure also means optimization in the time spent by the PD algorithm for the computation of the coefficients. As explained in section 2.1, the basic principle of the method is compatible with only 2 input images. Therefore, we decided to compare the performances of OPRA for only 3 input images instead of 4 (we rule out the 800nm defocus image). Table 1 presents the results of the comparison. This comparison was performed on the 6 first sets of PSFs acquired on NaCo, merging miscellaneous parameter (rotator angle, objective, date) tests.

Date	**Obj.**	**Rot.**	**3 PSFs**		**4 PSFs**	
		[°]	**Conv. time [s]**	**Sr [%]**	**Conv. time [s]**	**Sr [%]**
18/02	S13	0	16.2	93.1	34.3	92.9
18/02	S27	0	24.8	95.8	37.8	96.0
19/02	S13	0	21.8	91.9	34.9	91.7
24/02	S13	0	34.0	94.5	55.5	94.2
24/02	S13	45	14.9	92.4	21.2	92.2
24/02	S13	90	17.4	77.8	17.1	79.4
Mean convergence time (3 PSFs)					21.5 s	
Mean convergence time (4 PSFs)					33.5 s	
Mean deviation between 3 and 4 PSFs Sr values					0.45%	

Table 1: Convergence time (C.t.), rms of the Zernike coefficients (rms) and Sr computed by OPRA for 3 and 4 input PSFs corresponding to various parameters (date, objective, rotator angle).

From table 1, we derive that the mean convergence time for 3 PSFs is 30 % faster than for 4 PSFs, while Sr computations are roughly the same. In fact, as will be shown in section 4.5.3, the estimated error bars are about 2-3% for each Sr computation method. Therefore, the mean deviation of 0.45 % is clearly negligible. The advantage of a faster convergence time for 3 PSFs subsequently prompted us to perform all the following runs of OPRA with only 3 input PSFs.

4.4 Discussion of the different Sr measurement methods

Before presenting and interpreting calibrations results, we discuss in this section the specificities and biases of the different Sr computation methods. For a same image, different methods provide different Sr values. The goal is not so much the determination of the exact absolute Sr as the comparison of the values given within the same method for different images taken with a varying parameter. For a more thorough comparison about the accuracy on the Sr computation of different types of method, please refer to (Roberts et al., 2004).

4.4.1 Method 1: ESO pipeline

The *ESO pipeline* is run automatically for each image taken with the instrument, knowing the exact parameters of UT4/NaCo (such as the telescope pupil). It is not tunable, contrarily to methods 3, 4 and 5, that are so-called *Strehl Meters*. The scaling of the analytically created diffraction pattern to the energy of the PSF is performed in two steps. First, a background annulus of definite internal and external radii is taken and its median is subtracted from each pixel of the image, and in particular from the region located within the internal radius (called the *star radius*, or latter *sub-image*). Next, the total energy in the star radius is added and enables the normalization of the theoretical diffraction pattern. The ratio of the peak intensity of the PSF divided by the peak intensity of the diffraction pattern gives finally the Sr ratio.

The exact values of the star radius (corresponding also to the internal radius of the background) and the external radius of the background used by the ESO pipeline are respectiveley 2.0 and 3.0 arcsec. As described in subsection 3.4, two cameras are principally used: S13 and S27. Each of them provides respectively a pixel scale of 13 mas/px and 27 mas/px. Therefore, 2 arcsec is equivalent to 154 px and 74 px respectively on the S13 and S27 plates.

These values have to be regarded in parallel with subsection 4.4.3, since the computation principles are the same. A 154 px radius (or 308 px diameter) is far larger than the estimated ideal value (100x100 sub-image size). Taking a larger sub-image size provides a higher normalization of the theoretical diffraction pattern, hence a greater theoretical peak intensity (denominator in equation (10)). Consequently, Sr computed by this method are among the most pessimistic ones.

4.4.2 Method 2: OPRA

As stated in subsection 4.3, the *OPRA* function computes aberration coefficients and shows a phase map at each iteration. Using Maréchal approximation (equation (11)), an Sr computation with the wavefront phase variance is therefore straightforward.

$$\sigma_\phi^2 = \sum_{i>4}^{25} |c_i|^2 \tag{13}$$

where the c_i are the aberration coefficients expressed in radians. OPRA giving them in nm rms, the following conversion has to be done.

$$c_i = \frac{2\pi}{\lambda} a_i \tag{14}$$

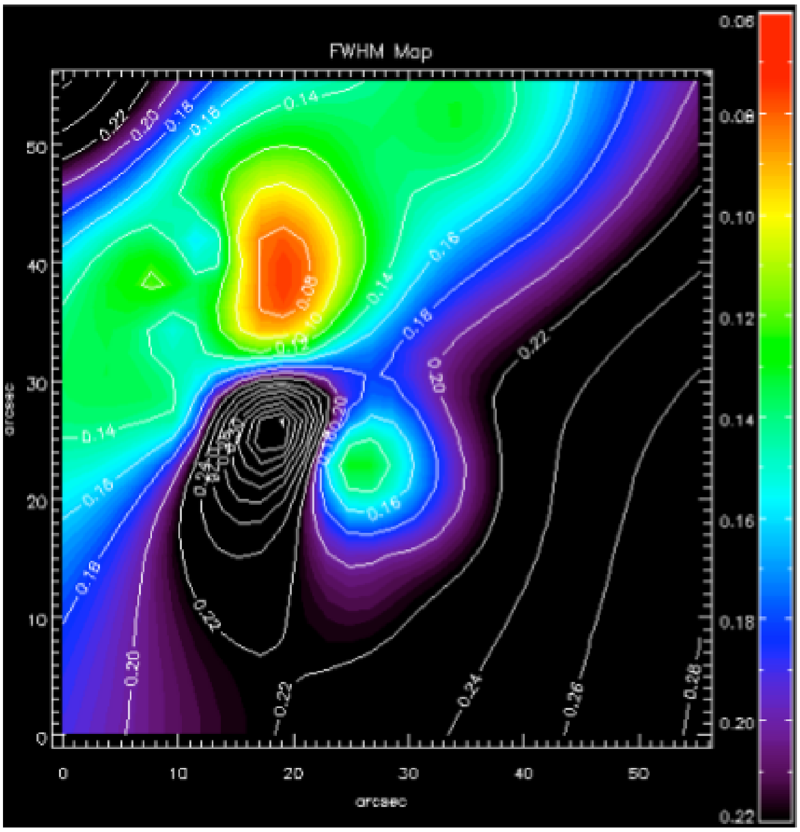

Figure 11: Sr map computed by MAD. Different colors correspond to different Sr values. The color correspondence ruler is plotted to the right of the image display. Lines of *iso-Strehl* are also displayed (Amico & Marchetti, 2007).

Among the five methods, the resulting Sr of this computation is on average the most optimistic. A first reason of this overestimate is the fact that only the first high-order coefficients ($4 \leq i \leq 21$) are taken into account in the computation. In addition, OPRA is not able to fit perfectly the high spatial frequency aberrations, and thereby the high-order aberrations (compare for example data with computed images in the upper part of figure 17). Since OPRA computes the Sr from the smoothed PSF, it tends to be more optimistic.

4.4.3 Method 3: MAD Strehl meter

The *MAD Sr meter* is an interactive tool developed in the framework of the MAD (Multi-Conjugate Adaptive Optics Demonstrator) project [22]. The MAD Sr meter uses roughly the same principle as explained for method one. However, its decisive assets are its ability to produce Sr maps (for several stars in the same field) and to be manually tunable in order to give the most appropriate Sr for each particular case. Figure 11 shows a Sr map produced by MAD whereas figure 12 represents a typical MAD Sr meter session.

In the latter, PSF and background files are uploaded from the upper-left fields. It is possible to perform the background subtraction if it has not been performed yet. If the input image is already

[22]More details about MAD project at http://www.eso.org/sci/facilities/develop/ao/sys/mad.html

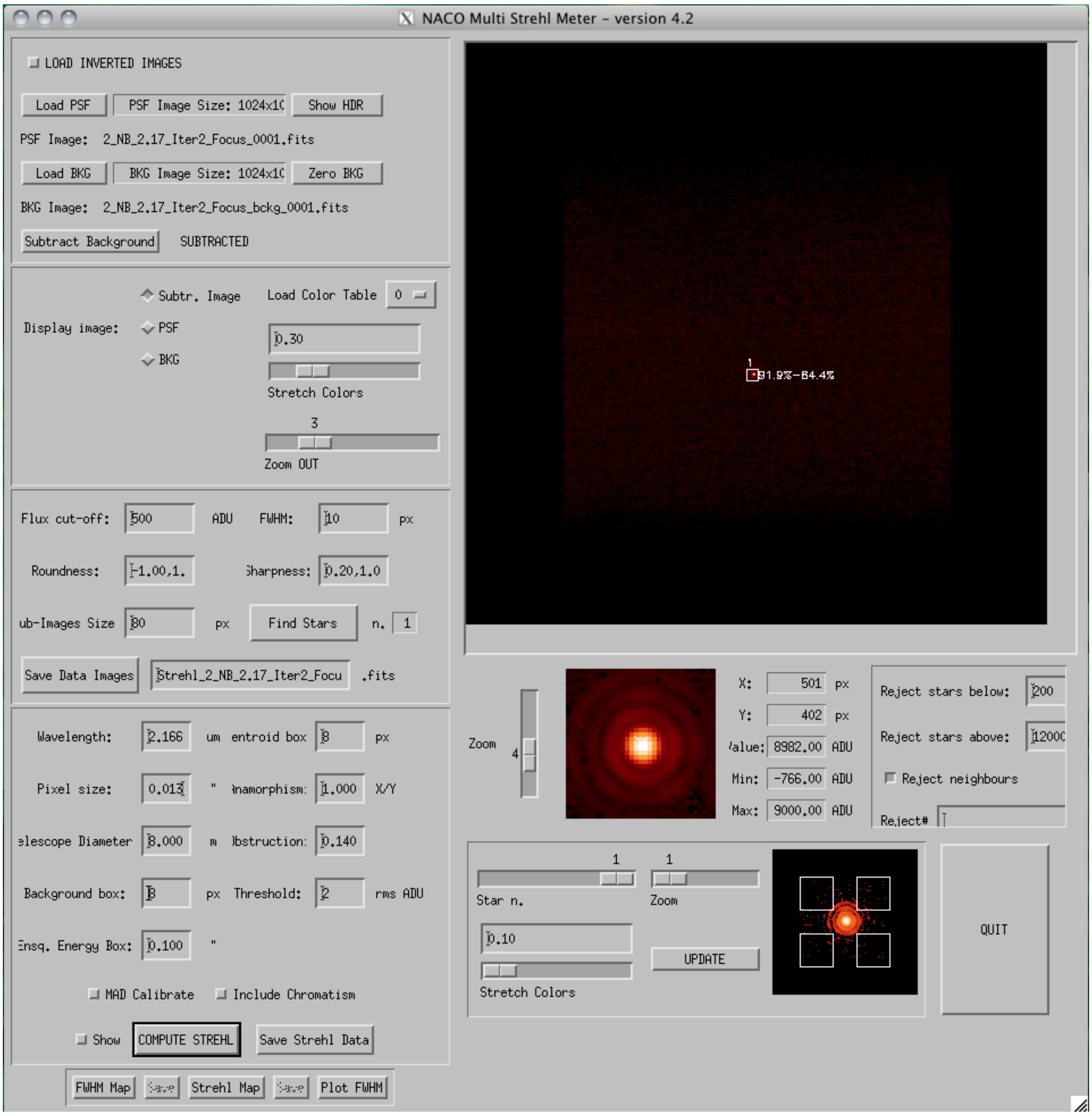

Figure 12: MAD Sr Meter window.

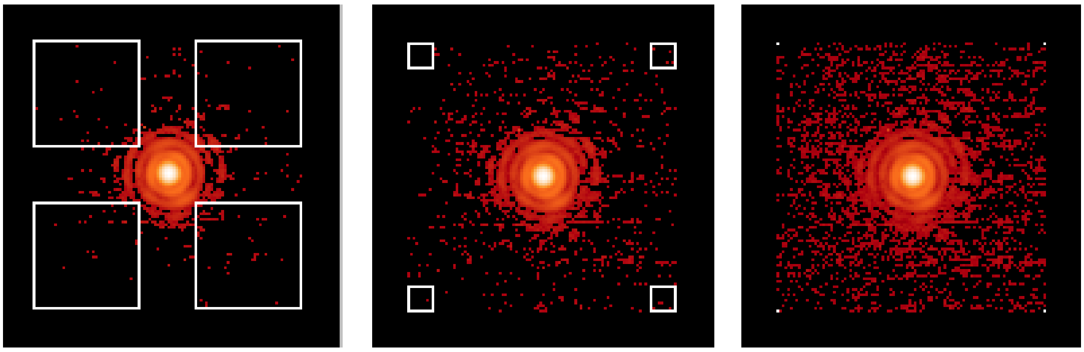

Figure 13: Illustration of three different background box sizes. From left to right: too large (a), ideal (b), too small (c).

background subtracted, choose *zero background*. The display options of the image shown on the right part of the window allow to control parameters such as zoom and colors.

From up to down, we find subsequently the *Find Stars Options*, which are necessary in order to select specific stars in a crowded field. It is mandatory to click on the *Find Stars* button after each change of parameter to let the software allow for the changes before the next Sr computation.

Under the *Find Stars Options* one finds the parameters that affect the Sr computation. Most of them are definite (wavelength, pixel scale, telescope diameter, obstruction), or should not be changed except in very particular cases (anamorphism, threshold, centroid box), but some (background box and sub-images sizes) should be tuned manually to find the most correct Sr. It should be noted that though the sub-image size field is located among the *Find Stars Options*, it is the parameter that affects the most the computed Sr, and should therefore be chosen wisely.

The sub-image enables the normalization of the theoretical diffraction pattern through the total ensquared energy (as explained in subsection 2.2.1). The size of this box matters for two reasons. First, the box should frame the PSF optimally: too small, the PSF is cut and not fully located in the box, too big, and there is a risk that other artifacts unrelated to the PSF are taken into account in the computation of the Sr. Second, background boxes are taken at the corners of this sub-image (instead of an annulus for method one), as shown in figure 13. Therefore, if the sub-image is taken too small or the background boxes set too big, the latest will encroach upon the speckles or even the PSF (case a). On the other hand, if the background boxes are taken too small, the estimated background and, hence, the computed Sr will be dependent upon single pixels effects (case c). Consequently, the background boxes have to be chosen not too small in order to dilute this effect, and not too big neither (case b).

In order to assess the ideal values for the size of these two boxes, we open one of the images taken during the calibrations (with the S13 camera) with *SAOImage DS9* software. Adjusting the scale parameters, it is possible to highlight the speckles (figure 14). A circle is then drawn to encompass it, and the value of its radius is used to define a minimal size for the sub-image. As can be seen on figure 14, a 50 px radius circle encompass most of the speckles. We infer from it that a 100x100 px box is a good choice for the sub-image, and that 10x10px background boxes are also a good compromise.

After the filling of all the parameter fields with the appropriate values, the *compute Strehl* button performs what it says and displays its solution directly on the image, close to the corresponding star. The second ratio that is given is the energy contained in the *ensquared energy box* (one of the parameter that had to be filled).

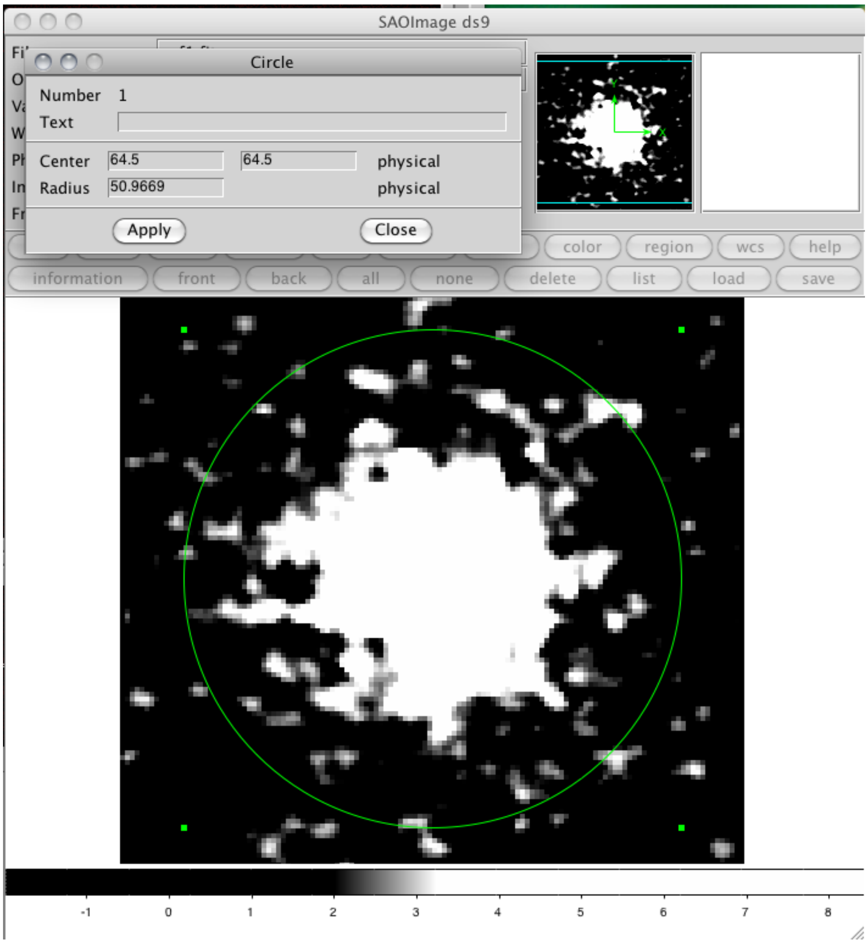

Figure 14: Estimate of the sub-image and background boxes size thanks to *SAOImage DS9* (zscale).

4.4.4 Method 4: MVD Strehl meter

As stated in previous sections, the MVD and the MAD Sr meter proceed in a very similar manner to compute the Sr. Both are based on equation (10), compute the theoretical diffraction pattern and normalize it through the energy ensquared in a region centered on the input PSF, before computing the ratio of the input PSF peak to the normalized theoretical peak. The difference lies in the way the theoretical diffraction pattern is computed. Whereas the MAD Sr meter takes the analytical diffraction pattern created by a centrally obscured telescope pupil, the MVD developed at Keck observatory computes it numerically. Since this numerical computation needs a binary mask representing the shape of UT4 pupil, I computed one through a simple IDL code which is given along with the computed pupil in appendix D.

Figure 15 shows a typical MVD session. The first step consists in entering the filename of the created pupil and the parameters of the observation: pupil pixel scale, PSF plate scale and wavelength. The *Calculate perfect PSF* button uses the pupil and the parameters to create a new .fits file containing the PSF. It basically operates a Fast Fourier Transform on the pupil mask. By definition, this Fourier transform is the complex wavefront at the focal plane of the instrument.

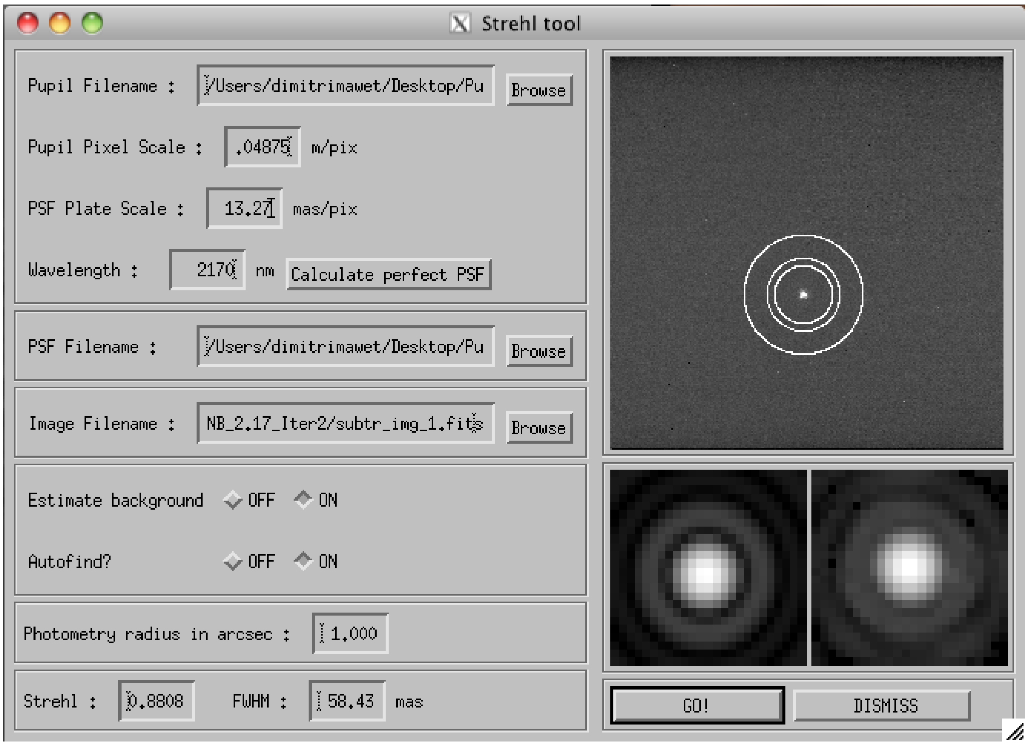

Figure 15: A typical MVD Sr meter session, showing the exact parameters uused for all the Sr measurements. Pupil pixel scale = 0.04875 m/px and PSF plate scale = 13.27 mas/px (cf. table. The input wavelength depends on the filter tested, NB_2.17 filter corresponds to 2170nm.

The diffraction pattern is then obtained with the modulus squared of the complex amplitude. This operation may take up to one minute, however once the PSF file has been created, it can be used again for any Sr computation on images taken with the same instrument at the same wavelength, loading it directly from the *PSF filename field* and thereby skipping the first step.

The filepath of the image with the PSF whose one wishes to estimate the Sr must be filled in the *Image filename* field. It is then displayed in the upper-right field. If the images are not background subtracted, ticking the option *Estimate background* estimates the background (!) from a circular annulus of sky in the vicinity of the star. In our case, they were already background subtracted, although the option was also set since only benefit can be extracted from it (which proved to be indeed the case, after tests with and without this option).

If *autofind* is set to *ON*, the program will automatically locate the star/source. If it is set to *OFF*, the user will be prompted to select the star. The photometry radius may be set or left at its default value of 1.0 arcsec. This is the circular aperture used to calculate the photometry of the star (used for the normalization of the theoretical PSF). Two fields are located under the image display, the left one shows the computed theoretical PSF whereas the right one is a zoom on the PSF of the selected source.

In fact, these two windows were very useful for an accurate value of the pupil pixel scale. Indeed, the telescope diameter being 8.2m and the pupil mask size being 160x160 px, the pupil pixel scale should be 8.2/160 = 0.0506 m/px. However, NaCo has in all likelihood a pupil stop limiting its effective diameter to 7.8-7.9 m. In addition, during calibration acquisitions the PSF is not taken through the telescope itself but thanks to a calibration lamp and a *telescope simulator*, which is an optical setup composed of apertures and lenses assembled to simulate the 8.2m diameter telescope. This simulation is not perfect, so that the diameter it simulates is not exactly 8.2m, while the computed Sr depends a lot on the input pupil pixel scale. In order to assess its correct value, we tested several values close to 0.0506 and compared sizes of the computed and the acquired PSFs. These tests led us to a pupil pixel scale of 0.04875, which correspond to a simulated telescope diameter of 7.8m. As can be seen on figure 15, their sizes are now approximately identical allowing for the blurring of the acquired PSF.

Finally, clicking on the *GO* button outputs the Strehl estimate and the FWHM of the PSF. Whereas the Maréchal approximation (equation (11) was used by OPRA to compute the Sr from the Zernike coefficients, it can here be used for the opposite purpose: the estimate of the residual wavefront error from the Sr[23].

Absolute Sr meter MVD's algorithm was among the 8 different Sr computing methods compared in the last Sr Competition Campaign. The principle of this contest is simple, several PSFs characterized by known Sr is sent to the different competitors. Variations in Sr between images were typically achieved by varying the number of AO actuators across the telescope pupil. Each of the competitors then use their own code to compute the Sr. The goal of this contest was not only to determine the best computing method but also to sensitize astronomers to the fact that computed Sr may vary significantly from one method to another. Results in the case of a Nyquist sampled image are plotted in figure 16.

While Sr computed for 2xNyquist sampled images led to similar and close to the real Sr values, Sr computed for Nyquist sampled images show discrepancies between the results. As can be seen on figure 16, MVD's algorithm was one of the most accurate methods, in particular for high Sr images. In case of discrepancies between the results obtained by the different methods, the results obtained with the MVD will logically be considered with the most weight.

4.4.5 Method 5: OTF Strehl meter

Instead of using (10) like methods 1, 3 and 4, the OTF Sr meter uses its equivalent in the focal plane:

$$Sr = \frac{\int OTF_{PSF}(\mathbf{u})\mathrm{d}\mathbf{u}}{\int OTF_{diff}(\mathbf{u})\mathrm{d}\mathbf{u}} \tag{15}$$

where $OTF_{PSF}(\mathbf{u})$ is the optical transfer function of the image, $OTF_{diff}(\mathbf{u})$ is the OTF of the diffraction limited optical system and $\mathbf{u}$ is the spatial frequency domain vector. In this definition, we assume the maximum value of the PSF is located at $\mathbf{x} = 0$.

The OTF Sr meter that I used was developed by ESO staff astronomer Sridharan Rengaswamy. It is a very intuitive and easy to use Sr meter. The telescope parameters (required for the computation of the pupil) and images path have to be defined at the beginning of the code. Two line codes have been added in order to perform automatically the background subtraction given the background and PSF file names. Launched from the terminal, the code then opens a new window with the acquisition. One has to select the desired star/source and using equation 15, the Sr is rapidly computed.

[23]More information about the MVD Sr meter at http://www2.keck.hawaii.edu/optics/aochar/Strehl_meter2.htm .

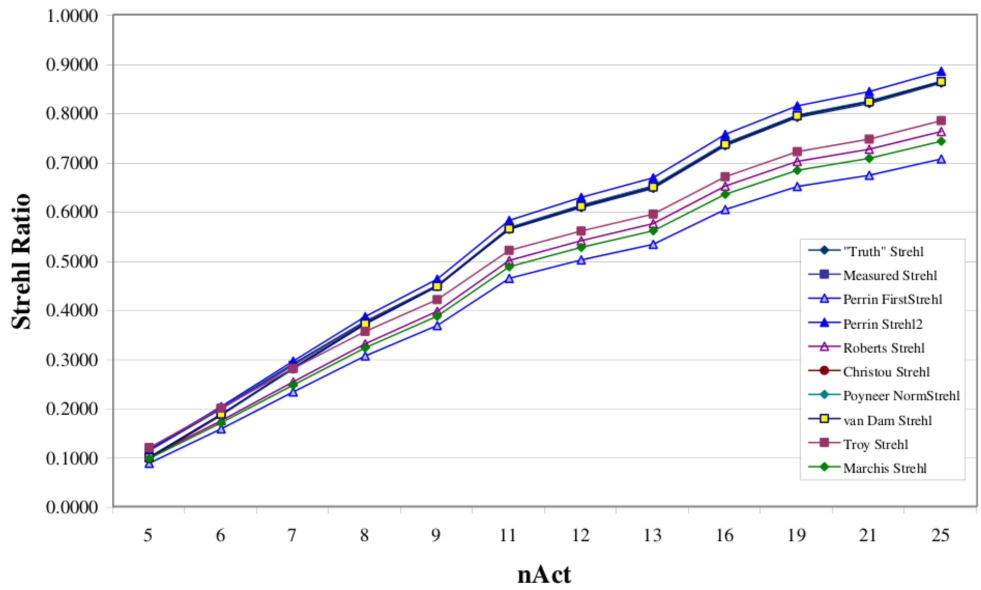

Figure 16: Comparison of the Sr computed by different methods. Marcos Van Dam's algorithm computed results that follow precisely the *truth* Sr curve. *nAct* is the number of AO actuators used while acquiring the image in close-loop. Increasing the number of actuators increases the image quality, thereby the Sr.

4.5 Implementation of the CONICA NCPA measurement procedure

Implementation of the new CONICA NCPA procedure briefly described in section 4.2 consists in the exact following steps.

1. Check in SOS panel (figure 34, appendix C) that the instrument is in park position (Adapter=0° and Rotator=0°), the Nasmyth B focus shutter is closed, and the upper lights are off in UT4.

2. Place NaCo in NIGHT mode.

3. Run the `DailyPupilCheck` OB if it has not been done yet, in order to align the NAOS pupil.

4. Run the VIS/VIS/1-4 `DailyCheckAO` OB to setup system (and load the aberration coefficients determined by the last static calibration campaign). The VIS/VIS/1-4 mode means VIS dichroic (characteristics in table 13, appendix C) and VIS WFS 14x14 (characteristics in table 14, appendix C).

5. Either in CONICA ICS control panel (figure 35, appendix C) or directly in CONICA SOS control panel (figure 34, appendix C), setup CONICA's optical path as follows:

   - Slit/Mask wheel - Field limiting mask (FLM) corresponding to the desired objective (typically FLM_13).
   - FPI wheel - Open.
   - Lyot wheel - Full (since tests with the Full_uszd pupil stop did not yield good results with OPRA).

- Grism wheel - Open.
- Filter1 wheel - the narrow band filter to test if located in this wheel, otherwise: Open.
- Filter2 wheel - the narrow band filter to test if located in this wheel, otherwise: Open.
- Camera wheel - the desired objective (typically S13).

6. Setup CONICA's detector as follows:
   - Either Double_RdRstRd or FowlerNSample readout mode. During our tests, the Double_RdRstRd mode has been prefered for its higher sensitivity.
   - DIT/NDIT - selected to optimize the signal strength but without saturating detector, typically 2s for the focused image. The number of acquisitions NDIT was set to 1 for all images.
   - CONICA detector windowing - 1024x1024.

7. Place NaCo calibration setup to *PSF lamp* so that LED and PSF fibers are respectively seen by the WFS and CONICA (figure 36, appendix C).

8. In the same tab, set the lamp diaphragm to a correct level and turn on the lamp source. Setting the diaphragm level to 500 for the NB filters yields typically a max flux above background of $\sim$ 5400 counts/sec, which is in the correct range for the FowlerNSamp and DoubleRdRstRd readout modes[24]

9. Perform a manual acquisition of the LED fiber with NAOS using the default settings. It is crucial that the acquisition mode is set to *Fine* so that the software correctly takes the distance between the LED and PSF fibers into account (figure 37, appendix C).

10. Close the loop (can be done from the SOS panel > NAOS > *control loops*).

11. Run the data acquisition process with the command line script `cnstooTakePDData` + *filter name*. This script takes 8 images, two (background + acquisition) at each of the four following defocus values: 0nm, 400nm, 800nm and 1200nm. The DIT of each acquisition is proportional to the defocus value in order to gather similar total fluxes (2s, 4s, 7s and 12s respectively).

12. Ftp the resulting phase diverse frames and dark frames to a system comprising OPRA.

13. Adapt OPRA script to allow for the specific file names (*psf_name_tmp* and *psf_dark_name_tmp* in appendix B), then run in order to get the aberration coefficients.

14. The Zernike mode indexing in OPRA matches the indexing used in the CONICA aberration panel. Therefore, entering them in CONICA's configuration files is *almost* straightforward. The entered coefficients have to be sign inverted from the ones given in the terminal panel (note that they are already sign inverted on the plots - figure 10).

15. Finally, if possible, re-run the tests to either iterate for improved corrections or to verify that the values were properly entered into the configuration files.

[24] As shown in table 15 (appendix C), the full well capacity of these two modes are respectively 7500 and 15000 ADU. The linear regime being considered to occur up to two thirds of the full well capacity, 5400 counts/sec is an appropriate level.

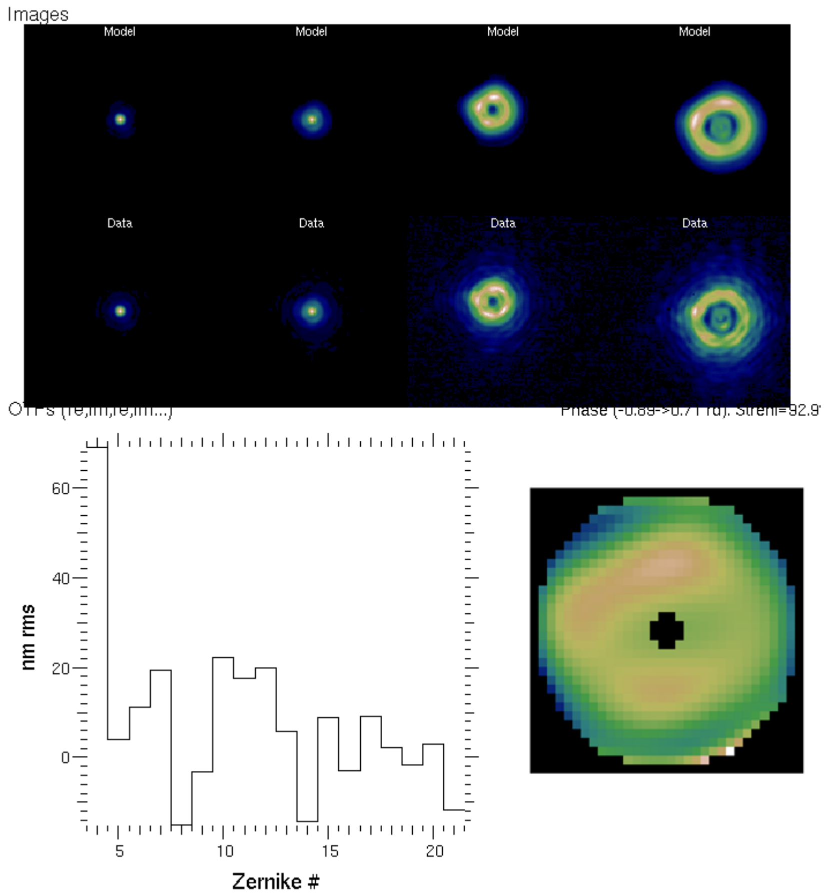

Figure 17: First results computed by OPRA for the reference mode of NaCo (VIS 14x14 WFS, S13 plate, NB_2.17 filter, rotator = 0°). Above: the different acquired PSFs with their corresponding model computed by the algorithm. Lower-left: Plot of the sign inverted Zernike coefficients. Lower-right: Pupil plane phase map.

4.5.1 First results

The described procedure was first applied to the commonly used S13 objective + NB_2.17 filter configuration on February 18th. It ran smoothly. The results computed by OPRA are given in figure 17. The plot of the sign inverted Zernike coefficients shows that the defocus term is by far the greatest coefficient. This is due to the fact that the PD algorithm is based on a variation of this term in order to retrieve the others. By definition, it will not be accurate in its estimate of the a_4 term.

Nevertheless, the high-order coefficients ($i \geq 5$) are below 20 nm in absolute value. One can infer from it that the corrections to this setup are already relatively good. Indeed, as the reference configuration, it was the most optimized by former static calibrations.

Values of the Zernike coefficients are given in table 2. If one wishes to improve the corrections on the static aberrations, these values have to be entered in the window opened by the `cnsguiConicaAberr` command, allowing the DM to correct these aberrations. One can then re-

Zernike #	S13	S27
4	-69	+37
5	-4	-26
6	-11	+12
7	-19	-13
8	+15	+7
9	+3	-1
10	-22	-10
11	-18	+40
12	-20	+2
13	-6	+8
14	+14	+13
15	-9	-9
16	+3	+5
17	-9	-9
18	-2	-1
19	+2	-3
20	-3	0
21	+12	+11
Phase variance (nm^2)	7301	4663
Phase variance σ_ϕ^2 (rad^2)	$6.12\ 10^{-2}$	$3.91\ 10^{-2}$
σ_ϕ **(nm rms)**	85.4	68.3
$\mathbf{Sr_2}$	93.5 %	96 %
$\mathbf{Sr_3}$	85.3 %	81.9 %
$\mathbf{Sr_4}$	81.5 %	78.1 %
$\mathbf{Sr_5}$	85.5 %	65.2 %

Table 2: Zernike high-order coefficients computed by OPRA for the S13 and S27 objectives. The values are expressed in nm. The sum of their squares gives the phase variance (in nm^2). The conversion between nm and radians is given by equation (14). The rms is also calculated (taking the square root of σ_ϕ^2). The Sr computed by OPRA is then given by the exponential of the sign inverted phase variance, as stated by the Maréchal approximation (equation (11)). Finally the Sr computed by the other methods are also given. As explained in next section, Sr values computed by the ESO pipeline are ruled out.

runs the procedure several times to see if further improvement is possible. These *iterations* are described in subsection 4.6.2.

In the same table, we present the Zernike coefficients computed for the same setup but with the S27 objective, which was tested immediately after. The values of the Sr computed by the other methods are also provided for both the S13 and S27 cameras.

Comparing the different Sr in table 2, it is obvious that the Sr computed by OPRA is overestimated. It is due to the insufficient number of Zernike coefficients that are allowed for in the computation. Moreover, the Sr computation based on these coefficients strongly depends on the defocus term since it is the greatest by far. This defocus term is also the least accurate. As will be seen in table 3, variations in time of this defocus term occurs in a range of 50 to 100nm, thereby triggering important fluctuations in the Sr computed by OPRA, while at the same time the Sr computed by the three Sr meters are globally stable. Consequently, as long as the defocus will not be small enough, we decide to only show consideration to the high-order Zernike coefficients computed by OPRA, but not to its derived Sr.

The Zernike coefficients and Sr computed by OPRA for the S27 mode are lower than those of the S13 mode, although almost identical for the Zernike coefficients above the 14th order. However, one should be very careful before stating that the S27 mode is better calibrated than the S13. Indeed, the sampling is different for the two modes. The FWHM of the PSF is roughly equal to 4 pixels ($\sim$ 50 mas) for the S13 objective, hence half for the S27. We are close to the Nyquist frequency sampling, where numerous Sr computing methods are known to be less accurate (cf. subsection 4.4.4).

In this same subsection, we showed that the MVD Sr meter was among the best Sr estimators in the case of Nyquist sampled images. In this case where the variations of Sr derived from one method to another are different, we thus favor the conclusion drawn by the MVD and the MAD Sr meter: there is a slight decrease in the image quality between S13 and S27 modes. It is logical since the resolution with the S27 camera is lower than with the S13, thereby allowing a lower-level detection for correction. We draw thus the opposite conclusion of what OPRA results convey.

From now on, all the following calibrations will be exclusively tested with the S13 objective.

4.5.2 Evolution of the results in time

Regular runs of the calibration procedure applied to the reference mode of NaCo were performed throughout my two stays at Paranal. As will be seen, analyzing the whole *a posteriori* evolution in time of this configuration's results before the results of tests on other configurations delivers several crucial information. Reference setup's aberration coefficients are plotted in figures 18, 19 and 20, respectively comparing the evolution within the same day, during 5 days and with 1 month interval. The values of the Zernike coefficients and the Sr computed at different dates are in table 3.

The first plot (figure 18) is reassuring and conveys stable environmental conditions in the dome (temperature, humidity). Indeed, the coefficients are remarkably similar early in the morning, later in the morning and in the afternoon, though one might however state that there is a tiny change between morning and afternoon. We infer from these values that our error bars are likely to be around 7-9 nm.

Analysing the second plot (figure 19), we first infer that the high-order coefficients (i.e. ruling out the defocus term) stay strikingly similar from one day to another, except for March 17th. Indeed, we observe obvious degradations for terms # 4, 11, 12 and 16 to cite but a few, leading to a substantially greater coefficients rms.

The Sr values computed by the different Sr meters (table 3) confirm that there was a strong degradation on March 17th. After checking my notes, it turned out that maintenance operations involving opening of the dome and moving of the telescope were performed that day. For some acquisitions, an elongated PSF was even visible. In consequence, we decide to not report the biased results obtained that day (comparison between the different WFS modes).

Finally, the 1-month comparison (figure 20) conveys as well a relatively good correspondence between the same Zernike coefficients, taking error bars of 7-9 nm.

The comparison of the Sr values computed by OPRA and the Sr meters (table 3) confirm what had been derived in the previous subsection. They are constantly overestimated and in the case of March 17th entry, do not show such a great loss as the Sr meters. One could be tempted by ruling out the Sr values computed by OPRA, which are only reflecting fluctuations of the defocus term (surpassing by far the other terms). However, we will see in section 4.6.1 that the comparison of the corrections for different filters, and thereby at different wavelengths, can not rely on the other Strehl meters. In addition, when the defocus term will be lower thanks to succesful iterations (section 4.6.2), fluctuations of OPRA's Sr will have more *significance*. Consequently, we will only

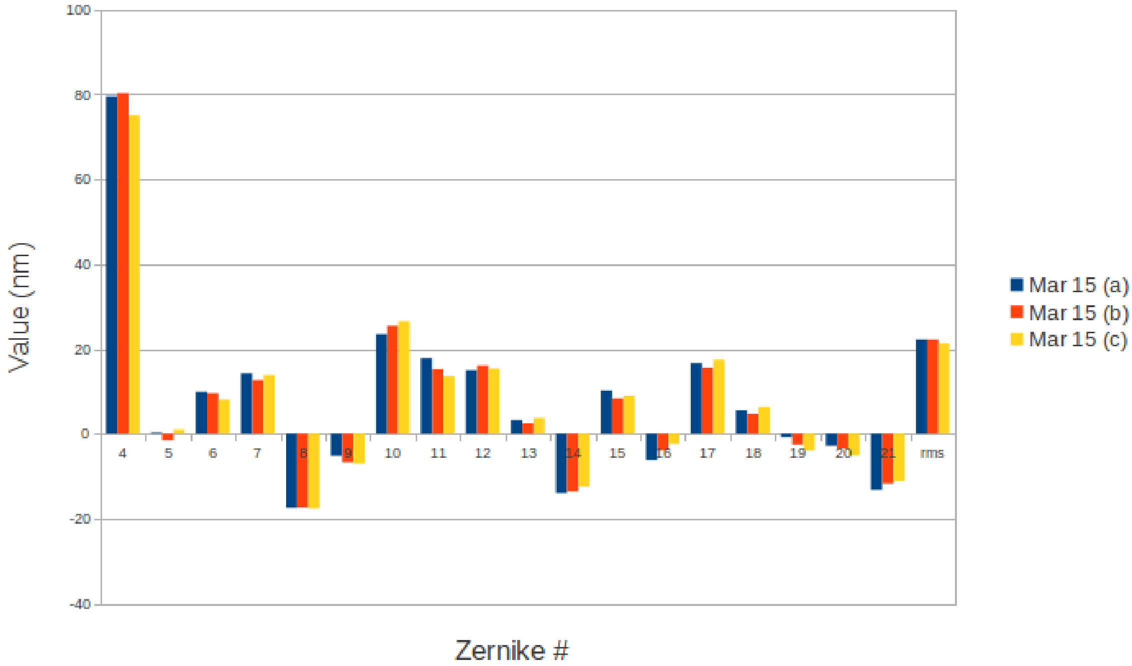

Figure 18: Plot of the Zernike coefficients computed for three measurements taken on March 15th. The first one early in the morning (a), the second later in the morning (b) and the last one in the afternoon (c).

rule out the Sr computed by OPRA when the defocus term is too great.

In the same table, comparing the Sr values given by the ESO pipeline with the Sr meters also leads to unsatisfactory conclusions. Take the case of the ΔSr between March 15th and March 17th. While all methods show a significant decrease, whose reason is now understood, the ESO pipeline shows the opposite trend. The Sr values computed by this method are sometimes close to the ones computed by the three Sr meters, sometimes way more pessimistic. As explained in subsection 4.4.1, the reason is the oversized sub-image. Indeed, using an oversized image for the photometric calibration of the theoretical PSF carries the risk of being influenced by artifacts unrelated to the PSF. A concrete example occured at the beginning of my second stay at Paranal. While the usual Sr values computed by the ESO pipeline are below 83 %, it computed an incredible 95 % Sr. Upon closer inspection, it turned out that the PSF was elongated and thereby could never correspond to such a Sr. In all likelihood, the algorithm took a hot pixel instead of the right PSF, which led to this false value. In consequence, we decide to rule out values given by the ESO pipeline, since they are the least reliable.

4.5.3 Estimates of the different Sr measurement methods error bars

As adverted in subsection 4.4, in the case of an attempt to optimize the set of compensating aberration coefficients, the relative differences of Sr computed within the same method are more important than the absolute Sr value. Subsequently, the error bars that will be estimated in this subsection do not represent the uncertainty towards the absolute Sr value but towards other Sr measurements of the same method. In other words, the error bar of each method represents the difference needed in order to qualify two measurements as *significantly* different.

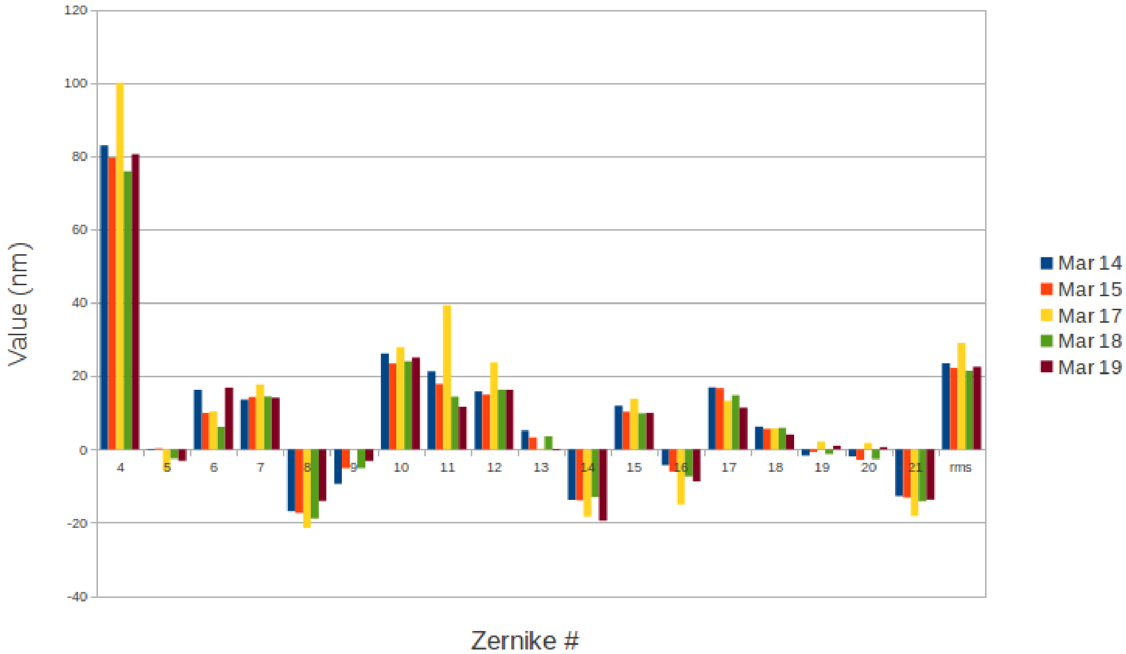

Figure 19: Plot of the Zernike coefficients computed for five different days: on March 14th, 15th, 17th, 18th and 19th.

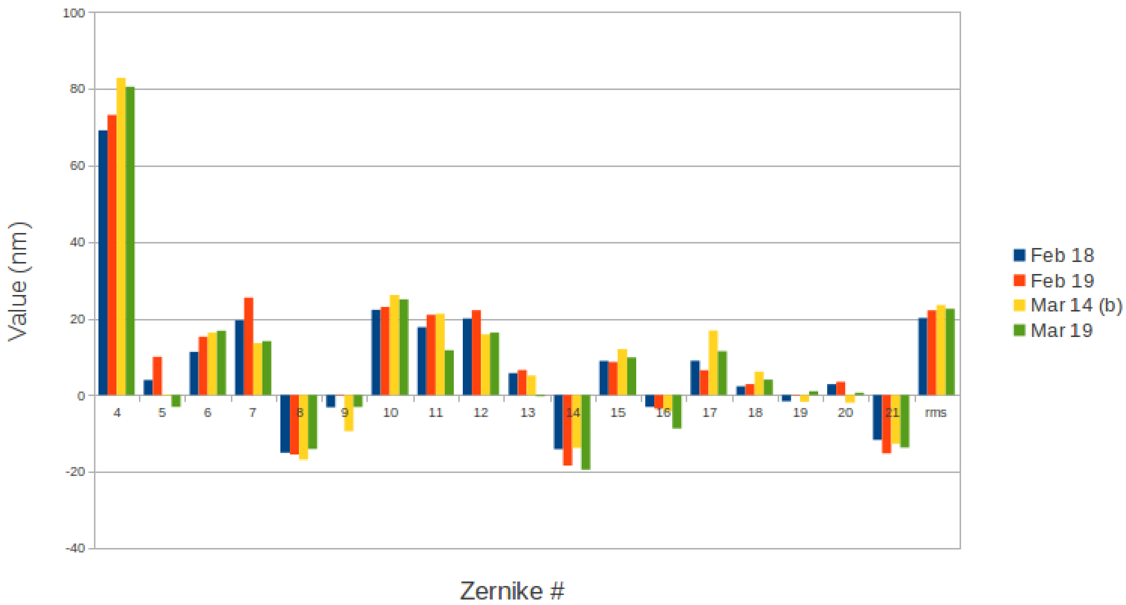

Figure 20: Plot of the Zernike coefficients computed for measurements taken both on February and March.

Date	σ_ϕ [nm rms]	$\mathbf{Sr}_1$ [%]	$\mathbf{Sr}_2$ [%]	$\mathbf{Sr}_3$ [%]	$\mathbf{Sr}_4$ [%]	$\mathbf{Sr}_5$ [%]
Feb. 18	85.4	92.9	/	85.3	81.5	85.5
Feb. 19	93.8	91.7	/	82.5	81.3	82.6
Feb. 24	73.7	94.2	/	78.7	76.0	78.2
Mar. 14 (11:15)	109.8	91.1	/	88.0	83.5	83.5
Mar. 14 (16:55)	99.7	90.1	/	84.5	80.1	81.4
Mar. 15 (early morning)	94.3	91.8	83.9	85.5	83.3	84.0
Mar. 15 (late morning)	94.2	91.8	79.3	84.8	80.5	82.0
Mar. 15 (afternoon)	90.2	92.3	76.1	83.2	80.2	84.1
Mar. 17	123.0	87.6	79.3	57.3	57.0	58.1
Mar. 18	90.7	92.3	86.3	84.4	82.0	82.5
Mar. 19	95.4	91.7	77.5	84.3	80.1	81.9
Median $\pm\sigma$	94.2$\pm$8.8	92$\pm$2	80$\pm$3	84$\pm$2	81.5$\pm$2	82$\pm$3

Table 3: Evolution in time of rms and Sr values computed by the five methods. The Sr values computed by the ESO pipeline on February and March 14th were not available anymore at the time I tried to retrieve them. The Sr values computed on March 17th confirm a strong degradation and to a lesser extent, February 24th as well.

The causes of the absolute Sr error bars are mainly linked with the photometric incertitude in the acquisition. We do not focus here on this issue. However, the interested reader can find a comprehensive discussion about this topic in (Roberts et al., 2004).

Method 3: MAD Strehl meter The error bars of the Sr computed by MAD are assessed in the following way. First, asserting a fixed value of 10x10 px (as determined in subsection 4.4.3) for the background boxes, the Sr is computed for values of sub-image size varied from 30x30 px to 256x256 px (table 4). We put in the first column the Sr computed for a mean case, and the two other columns correspond to the most extreme - minimum and maximum - cases obtained among all the measurements.

For sizes ranging from 30x30 to 60x60 px, the background boxes are too large compared to the sub-image and we are in the case shown in figure 13 a). It can be seen that the Sr ratio is then significantly overestimated[25]. On the other hand, a size of 256x256 gives a discrepancy in the computed Sr and it can be concluded that artifacts unrelated to the PSF have been accounted for during the computation (figure 13 c). The *significant* values of Sr are thus those computed for sub-image sizes ranging between 70x70 and 120x120 px.

Second, asserting a fixed value of 100x100 px (as determined in subsection 4.4.3) for the sub-image frame, the Sr is now computed for values of background box sizes ranging from 1x1 px to 40x40 px (table 5).

Again, for sizes larger than 32x32 px, we are in the case shown in figure 13 a) and the Sr are overestimated. Up to 3x3 px, the computed Sr show some random evolution. The single pixels effects are dominant. From table 5, we infer that the *significant* background box sizes, for a sub-image size of 100x100 px, are ranging between 4x4 and 28x28 px.

We decide to call *Sr standard values* the Sr values computed in the configuration [100x100 px (sub-image size), 10x10 px (background box size)]. Using this definition, we decide to assign to

[25] The Sr is overestimated (and not underrated) since in this case, the background is higher, therefore the ensquared energy that acts as normalization of the theoretical diffraction pattern is lower, hence a lower highest peak in the theoretical diffraction pattern (the denominator of equation (10)) triggering a higher computed Sr.

Sub-image box size	**Sr, mean case (18/02, rot0)**	**Sr, worst case (24/02, rot90)**	**Sr, best case (19/03, iter2)**
30x30	96.4	81.3	99.6
40x40	90.4	76.2	94.9
50x50	88.1	74.9	93.2
60x60	88.1	74.7	92.7
70x70	87.7	74.1	92.1
80x80	87.0	73.6	91.9
90x90	85.3	73.4	90.7
100x100	85.3	72.8	91.6
110x110	85.3	74.0	91.4
120x120	86.0	73.2	91.4
256x256	86.8	71.9	86.9

Table 4: Sr computed for a fixed background box size (10x10 px) and a variable sub-image box size. The software does not accept intermediate values between 120x120 and 256x256 px.

Background box size	**Sr, mean case (18/02, rot0)**	**Sr, worst case (24/02, rot90)**	**Sr, best case (19/03, iter2)**
1x1	82.9	73.6	92.4
2x2	84.9	73.3	91.6
3x3	85.7	73.2	90.1
4x4	85.3	73.2	91.6
6x6	85.3	72.6	91.6
8x8	85.5	73.1	91.6
10x10	85.3	72.8	91.6
12x12	85.7	72.8	90.5
16x16	85.7	73.2	91.6
20x20	86.4	73.2	91.6
24x24	86.4	73.3	91.6
28x28	86.6	73.6	94.0
32x32	86.6	73.9	93.6
36x36	87.1	73.8	93.4
40x40	87.6	74.2	93.4

Table 5: Sr computed for a fixed sub-image box size (100x100 px) and a variable background box size.

the error bars the maximum value among the three maximum deviations (obtained for the mean, worst and best cases) with the *Sr standard values*, considering only *significant* Sr values. Better a good example than a sermon, in the first column, the *Sr standard value* is 85.3% and, looking in the same column of both tables 4 and 5, the value which is both *significant* and the most distant is 87.7%. Therefore, the maximum deviation in the first column is 2.4%. The same operation performed on the two other columns provides 1.3 and 2.4%. The maximum of these three values is then 2.4%. In conclusion, one should assign approximately a ±2.4% error bar to the MAD Sr measurements.

This value is consistent with the Sr deviation of MAD that was found in table 3. It means that the former calibrations show constant performances in the course of time.

Method 4: MVD Strehl meter Relying on the fact that the correction performances are constant with time, as derived with the MAD Sr meter. We infer that the error bars of the MVD Strehl meter are approximately equal to its corresponding standard deviation in table 3. Their value is thus about ±2 %.

Method 5: OTF Strehl meter The same reasoning provides an error bar of about ±3% for the OTF Strehl meter.

4.6 Effects of different parameters on the image quality

In this section, the results of the reference setup (VIS 14x14 WFS, NB_2.17 filter, rotator=0°, 0 iteration) are compared to similar setups with either one or several modified parameters, in order to quantify each parameter's influence on the aberrations.

4.6.1 Effect of different filters

As explained in section 4.2.2, after characterizing the reference mode using the most used filter, all the other filters should also be tested with the `cnstooTakePDData` script + OPRA combination. Each time, the resultant aberration coefficients, specific to the filter used, are added to the current coefficients in the corresponding configuration file. In this way, the system will be well-calibrated for the VIS 14x14 WFS's different filters modes. As a reminder the different filters available and their characteristics are presented in table 18 (appendix C).

Figure 21 plots the Zernike coefficients computed for five commonly used broad and narrow band filters: NB_2.17, Ks (centered on 2.18 μm), NB_1.04, H (centered on 1.66 μm) and J (centered on 1.265 μm). We observe that they are relatively different. However, some coefficients show relatively similar trends such as coefficients 7, 8 (primary comas), 9, 10 (trefoils), 14, 15 (quadrafoils), 20 and 21 (pentafoils)[26]. We also note that there are stronger similarities between the wavelength-close NB_2.17 and Ks (2.18) filters than with the others.

From these observations, we conclude that different filters introduce indeed different aberrations, and require therefore specific corrections. However, some particular coefficients show similar values, meaning likely that some of them are introduced by common features of the different filters (collimator or objectives aberrations as proposed in section 4.2. It is interesting to note that although the different filters introduce aberrations in different ways, all considered they still give similar coefficients rms (last column).

[26] Cf. figure 3.

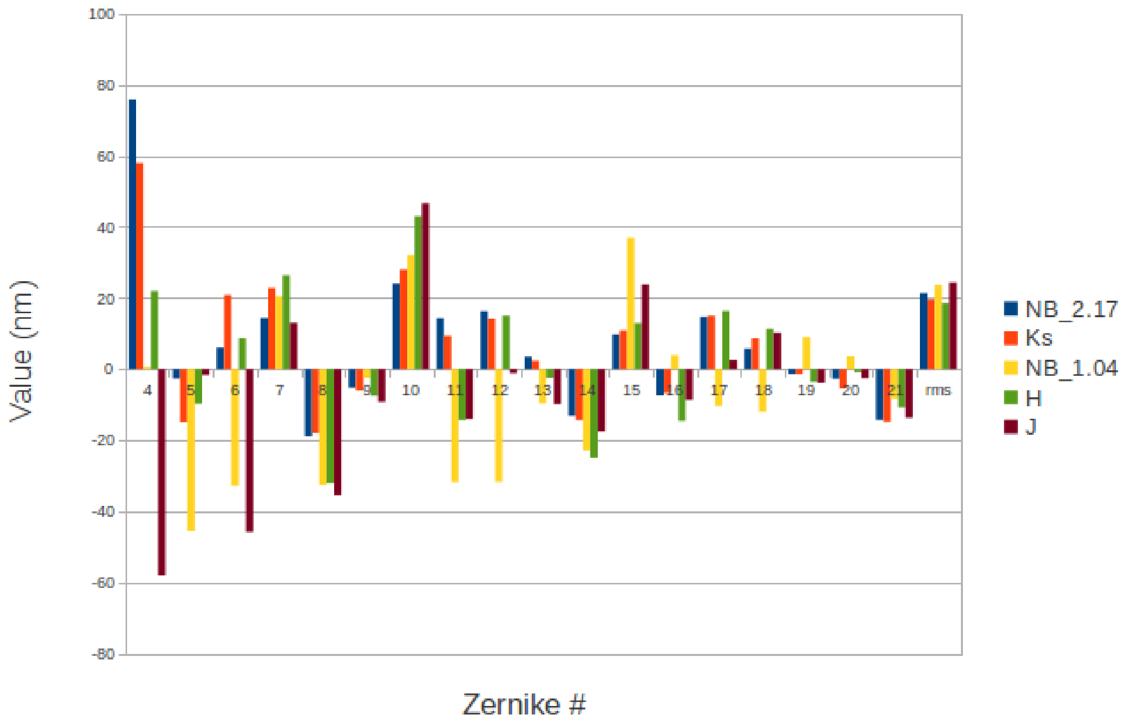

Figure 21: Plot of the Zernike coefficients computed for five commonly used filters.

We give in table 6 the exact values of the Zernike coefficients computed for the different filters. If one wishes to improve the corrections on the static aberrations for these specific filters modes, these values have to be added in the appropriate configuration files[27].

Different filters are used at different wavelengths. In addition, images background level and diffraction pattern are wavelength-dependent. In view of the definition of Sr (equation (10)), it is background level- and thereby wavelength-dependent. Comparing the image correction level with this ratio is subsequently not suited. Even though they are given in table 6, one should keep in mind that no direct comparison is possible between the level of corrections between the different filters. Note that these Sr values are computed in the same way as before, except that the wavelength field has to be filled by the appropriate value (sometimes difficult to assess if the filter is a broad-band one) so that the Sr meters compute the corresponding diffraction pattern. In particular, the SHK filter is a very broad band filter (used for spectroscopy), it was therefore very difficult for the Sr meters to compute the Sr. It accounts for the non physical values computed by MVD and OTF Sr meters.

Being only based on the Zernike coefficients value, one could think that the Sr computed by OPRA is wavelength-independent, allowing therefore a better comparison of the correction level provided to the different filters modes. In reality, they are also indirectly wavelength-dependent since images are taken at different wavelengths as well. One should therefore remain cautious before infering from Sr_2 line of table 6 that the correction levels are equivalent for the different filters (which could already be infered from the similar rms values in figure 21).

[27]Better estimated coefficients are given in subsection 4.6.2 for filters NB_2.17 and Ks.

Zernike #	NB_2.17	Ks	NB_1.04	H	J	IB_2.48	SHK
4	+76	+58	+1	+22	-58	105	+21
5	-3	-15	-45	-10	-2	-18	-9
6	+6	+21	-33	+9	-46	-4	+16
7	+14	+23	+20	+26	+13	+12	+37
8	-19	-18	-32	-32	-35	-9	-11
9	-5	-6	-2	-7	-9	-6	-13
10	+24	+28	+32	+43	+47	+17	+37
11	+14	+9	-32	-14	-14	+11	-58
12	+16	+14	-32	+15	-1	+11	+16
13	+4	+2	-10	-2	-10	+2	-1
14	-13	-14	-23	-25	-17	-7	-23
15	+10	+11	+37	+13	+24	+10	+17
16	-7	-7	+4	-15	-9	-2	+4
17	+15	+15	-10	+16	+3	+6	+27
18	+6	+9	-12	+11	+10	+1	+9
19	-1	-1	+9	-4	-4	+1	-5
20	-3	-5	+4	-1	-3	-3	-3
21	-14	-15	-8	-11	-14	-14	-12
σ_ϕ **[nm rms]**	90.7	83.0	100.3	79.0	103.4	111.6	95.8
$\mathbf{Sr}_2$ [%]	92.3	92.9	87.5	92.5	89.1	88.9	89.3
$\mathbf{Sr}_3$ [%]	84.4	92.2	55.1	82.9	63.5	85.5	32.9
$\mathbf{Sr}_4$ [%]	82.0	90.4	46.5	76.1	58.9	91.0	/
$\mathbf{Sr}_5$ [%]	82.5	90.5	46.8	77.7	58.7	86.3	/

Table 6: Zernike coefficients, rms and Sr computed for different filters. The exact sets of coefficients are given to serve as new reference coefficients for these modes. The Sr computed for SHK filter by MVD and OTF Sr meters were non physical (above 100 and below 0 respectively).

4.6.2 Effect of several iterations

After retrieving the phase aberration coefficients, they have to be entered through the `cnsguiConicaAberr` command in order to check the improvement on the image quality and the new residual coefficients, as well as to possibly continue the improvement with other iterations. The panel that is opened by this command is shown in figure 38 (appendix C).

As explained in the logbook, the first attempts to iterate were carried out on March 14th and did not lead to better results. In consequence, we thought that the aberration corrections obtained by the former calibration campaign were already sufficiently accurate so that no further correction was possible. My objectives were then modified and I turned to the characterization of filters and rotator angle's effects to cite but a few.

I realized by chance on March 19th that in reality we misused the `cnsguiConicaAberr` panel. During the first attempts to iterate, we did not apply the coefficients found by OPRA *differentially* to those loaded by clicking on the *refresh* button (which are those present in the configuration files), but *directly.* In other words, when for a specific Zernike term the loaded value was e.g +10 nm and the sign-inverted OPRA value e.g. +20 nm, we did apply +20nm instead of applying 10+20 = +30 nm. These values are then added to the aberrations due to the dichroic used (which were estimated separately).

The input coefficients are used to modify the DM to the most appropriate shape to correct the wavefront errors. The conversion from Zernike coefficients to voltages applied to the DM occurs as represented in figure 39. This operation first needs the conversion from Zernike to *slopes* (cf. section 4.1) and then from slopes to voltages applied to the DM. The latter matrix is in reality the inverted IM, whose estimate must thus have been performed accurately during the NAOS calibration phase[28].

The new coefficients being entered differentially in the panel, a new iteration consisting in basically the same operations as described in section 4.5 can be performed. More exactly, the procedure can be safely resume from step 4, up to step 10. A major discovery was then achieved at step 11. As afore explained, the PD acquisition launched by the `cnstooTakePDData` script takes images at 4 different defocuses which are 0, 400, 800 and 1200 nm. Each time it is run, it thus starts from its *zero* defocus (i.e. focused) position. However, this focused position is not accurately known. The defocus correction present in the configuration file allows a way better estimate of the focused position. Therefore the next acquisitions should be taken at: z4 initial defocus term (obtained through clicking on *Refresh* in the `cnsguiConicaAberr` panel and whose value is about +80 nm) + 0, 400, 800 and 1200 nm = 80, 480, 880 and 1280 nm instead. These acquisitions were done manually since `cnstooTakePDData` script was inappropriate. Comparison of the results after one iteration, with and without taking this defocus correction into account are given in table 7.

Iteration	σ_ϕ **[nm rms]**	$\mathbf{Sr_2}$ **[%]**	$\mathbf{Sr_3}$ **[%]**	$\mathbf{Sr_4}$ **[%]**	$\mathbf{Sr_5}$ **[%]**
0	95.4	91.7	84.3	80.1	81.9
"0.5"	85.6	92.8	83.8	81.1	84.2
1	41.5	97.6	90.3	85.2	85.9

Table 7: Rms and Sr computed in the three following cases: 0 iteration (0), correction of the high-order coefficients but not taking the defocus term into account ("0.5") and correction of the high-order coefficients with taking of the defocus term into account (1). These values were obtained with the reference mode and NB_2.17 filter.

The sole correction of the high-order aberrations seem to provide both a slight decrease in the rms and a slight increase in the Sr computed by the Sr meters. However, it is not even certain that there is indeed image quality improvement because the evolution of the values can be considered within error bars. On the contrary, taking the defocus term into account provides a jump of about 4 to 6 % in Sr (depending on the method). No ambiguity about the usefulness of this action is therefore possible. I suggest modifying the script in the future in that sense. If not, the manual acquisition of eight (acquisition + background) *phase diverse* images being extremely time-consuming, one would spend days to test only the main other filters.

Both the understanding of the way to use the `cnsguiConicaAberr` panel and the inappropriateness of the `cnstooTakePDData` script for iterations were discovered the last day of my second run at Paranal. In addition, the manual acquisition of *phase diverse* images is very time-consuming. Consequently, few iterations could be done. As explained in the next paragraphs, we performed 2 iterations on the most-used NB_2.17 filter and also performed 1 iteration with the Ks filter.

NB_2.17 filter Figure 22 shows the evolution of the absolute value of the Zernike coefficients with the number of iterations, for the NB_2.17 filter. We chose to plot the absolute values since there is no similarity between coefficients computed at consecutive iterations (indeed, they are only

[28] Typically, one computes the interaction matrix by pushing one by one the different actuators of the DM and looking at the slopes on the WFS. In practice, several actuators defined by Hadamard matrices are pushed at the same time in order to allow a faster computation.

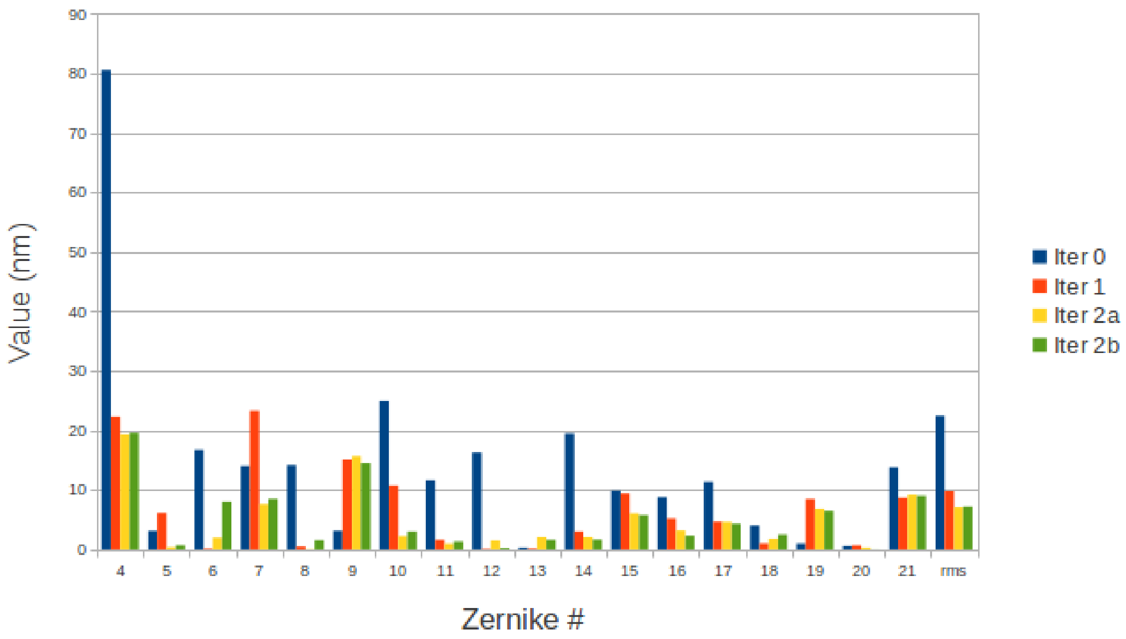

Figure 22: Plot of the absolute value of the Zernike coefficients computed after 2 iterations for filter NB_2.17. The coefficients in case 2a were obtained considering all the coefficients of step 1 but the imprecise defocus term, whereas this term was not neglected to reach case 2b.

meant to correct previous iteration's value). Therefore, showing the absolute values instead of the real values enables a better visibility of their decrease.

Two cases were considered at the second iteration. In the first case (2a), we applied the high-order coefficients determined at iteration 1 but we neglect the defocus term estimated by OPRA, since it is known that its estimate of a_4 is unaccurate. The case 2b is obtained by applying it, in order to confirm that no improvement is obtained.

As expected while observing figure 22, the coefficients globally decrease when the number of iterations increases. It is confirmed by the coefficients rms in last column. We also notice that values computed at steps 2a and 2b are close and provide similar coefficients rms.

Table 8 provides the Zernike coefficients, the rms and Sr according to the number of iterations. From it, and after only two iterations, it is already possible to say that the defocus term computed by OPRA does not converge. Indeed, let's compare cases 2a and 2b's values:

Case 2a: We do not take the defocus correction computed at iteration 1 into account. As expected, the next defocus term is roughly the same (-19 instead of -22 nm).

Case 2b: We take the -22 nm correction into account. The new defocus term is now estimated as its exact opposite (+20 nm).

Subsequently, continuing iterations that take the defocus term estimated by OPRA into account would, in all likelihood, not make it converge. This result was expected, it confirms the fact that the PD technique is not suited to estimate the term that it makes itself vary in order to recover the others. The defocus uncertainty is therefore ± 40 nm. This result is consistent with the original

Zernike #	**NB_2.17** Iter. 0	Iter. 1	Iter. 2a	Iter. 2b	Sum (0+1+2a)	**Ks** Iter. 0	Iter. 1
4	+81	-22	-19	+20	+81	+8	+2
5	-3	-6	0	+1	**-9**	-10	+13
6	+17	0	+2	+8	**+19**	+25	-11
7	+14	-23	+8	+8	**-1**	+21	-16
8	-14	-1	0	-2	**-15**	-13	+6
9	-3	-15	+16	+15	**-2**	-6	+2
10	+25	+11	-2	-3	**+34**	+27	-22
11	+12	-2	+1	+1	**+11**	+3	-1
12	+16	0	-2	0	**+14**	+12	-10
13	0	0	-2	-2	**-2**	+1	+2
14	-19	-3	-2	-2	**-24**	-17	+8
15	+10	+9	-6	-6	**+13**	+11	-12
16	-9	+5	-3	-2	**-7**	-4	-2
17	+11	+5	-5	-4	**+11**	+10	-7
18	+4	-1	+2	+3	**+5**	+5	-3
19	+1	-8	+7	+6	**0**	0	+1
20	+1	+1	0	0	**+2**	-2	0
21	-14	-9	-9	-9	**-32**	-12	-7
σ_ϕ **[nm rms]**	95.4	41.5	30.0	30.6	-	55.0	38.9
$\mathbf{Sr_2}$ [%]	91.7	97.6	98.4	98.2	-	96.4	97.4
$\mathbf{Sr_3}$ [%]	84.3	90.3	91.6	90.3	-	96.9	87.7
$\mathbf{Sr_4}$ [%]	80.1	85.2	88.1	86.7	-	90.4	83.4
$\mathbf{Sr_5}$ [%]	81.9	85.9	86.2	86.3	-	92.1	87.1

Table 8: Evolution of the Zernike coefficients, their rms and Sr for the NB_2.17 and Ks filters with the number of iterations. The bold set of coefficients is the one recommended to replace the former reference mode's configuration file. It is the sum of the 0, 1 and 2a iterations for all the coefficients but the defocus term.

cumbersome PD-based procedure which led to ±35 nm and a few nm for respectively the defocus and the high-order terms uncertainties (Hartung et al., 2003).

The results obtained with the different Sr-computing methods all lead to a same conclusion for the two first iterations: we have a gain in Sr. The gain is of course greater after the first iteration (0 → 1): between 4 and 6 % depending on the method, thereby greater than the error bars. We still have a gain ranging between 1 and 3% of Sr at the second iteration (1 → 2). This increase could be considered in the error bars, however since all of the methods show this jump, the possibility of a real slight increase should be favored.

Summing the coefficients provided at iteration 0, 1 and 2a (except for the defocus term) provides the best estimate of the residual static aberrations of CONICA after the previous static calibration campaign that provided the current configuration files. The sum is performed and appears in bold in table 8. This bold set represents relative corrections that need to be provided. We therefore recommend to replace the current values in the configuration file by their sum with the bold set. We also recommend to estimate the defocus term with another more accurate method.

Ks filter The same iteration procedure applied to the Ks filter provides the plot given in figure 23. We observe a striking sign inversion for almost all the computed coefficients after the first

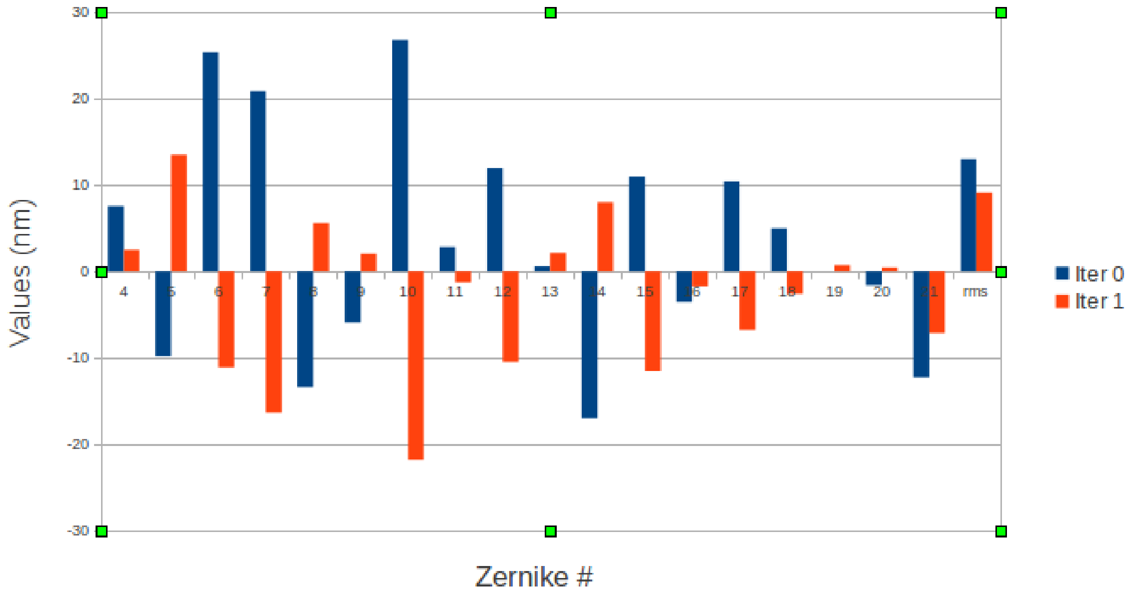

Figure 23: Plot of the Zernike coefficients computed after 2 iterations for filter Ks.

iteration. It seems first values were overestimated, so that the first iteration needed sign inverted coefficients. However, we note again a global decrease of the coefficients value (cf. the rms values).

Surprisingly, looking at table 8, the Sr values computed by the different Sr meters convey a decrease of the image quality. Consequently, we do not recommend to take the computed coefficients into account for new configuration files. Instead, we recommend to perform more iterations during the next static calibration campaign.

4.6.3 Effect of the rotator

As stated in section 3, NaCo is mounted on an adapter/rotator. The instrument thus rotates during observations. Rotation involves mechanical flexures in the instrument, in particular to all detectors. The sensed WF is therefore different according to the rotator angle. In order to quantify this effect, we ran the calibration procedure for several rotator angles. Zernike coefficients retrieved on February 24th are plotted in figure 24, those retrieved on March 15th in figure 25 and table 9 shows the rms and Sr obtained both on February 24th and March 15th.

In figure 24, we notice that Zernike coefficients stay quite similar for angles 0 and 45°. On the contrary, they tend to burst at 90°. Though we were expecting a slight decrease in the image quality, the magnitude of this burst is a bit suspicious.

Data taken at different rotator angles during my second run show a more credible increase of the Zernike coefficients. Looking at figure 25, coefficients of the same Zernike numbers appear to be relatively similar at different angles. As a matter of fact, only the defocus term (a_4) and primary vertical astigmatism (a_6, cf. figure 3) show a dramatic difference at 90°compared to other terms. Looking again at figure 25, we notice that these two terms were indeed the most substantial at this angle on February 24th as well.

The Sr computed by the Sr meters (table 9) tend to confirm that there is a drop of image quality with the rotator angle. On February 24th, the drop is significant, leading to an rms value over 175 nm rms at 90°, whereas it is decreasing gently on March 15th.

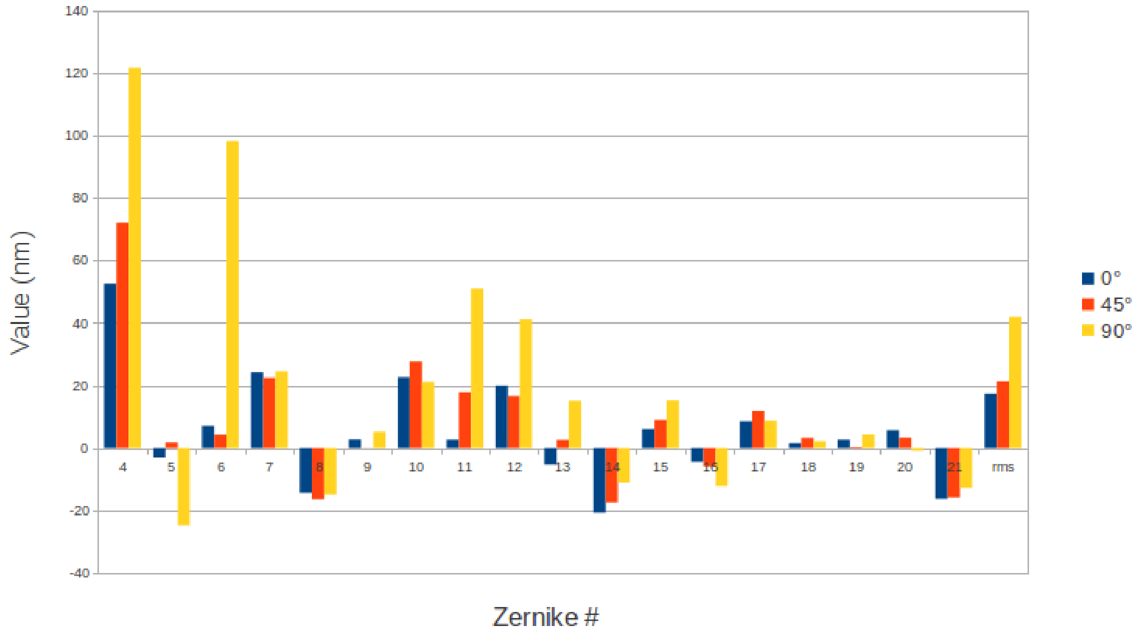

Figure 24: Plot of the Zernike coefficients computed for the three following rotator angles: 0°, 45°and 90°. The acquisitions were taken on February 24th.

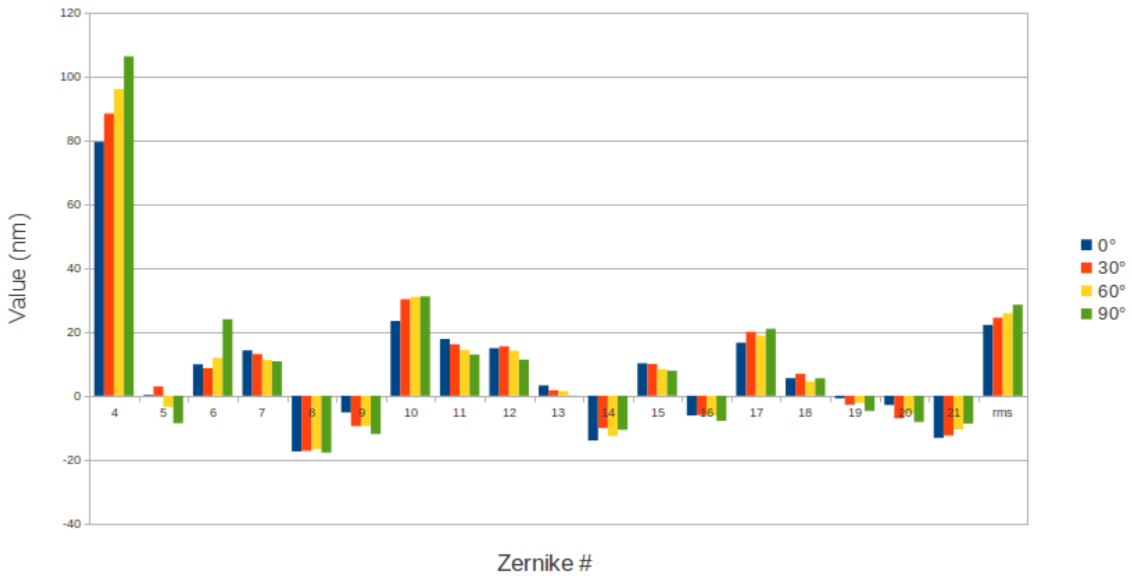

Figure 25: Plot of the Zernike coefficients computed for the four following rotator angles: 0°, 30°, 60°and 90°. The acquisitions were taken on March 15th.

Angle (Feb. 24th)	σ_ϕ **[nm rms]**	**Sr**$_3$ **[%]**	**Sr**$_4$ **[%]**	**Sr**$_5$ **[%]**
0°	73.7	78.7	76.0	78.2
45°	90.5	85.0	81.9	82.5
90°	177.9	72.8	69.1	70.6
Angle (Mar. 15th)	σ_ϕ **[nm rms]**	**Sr**$_3$ **[%]**	**Sr**$_4$ **[%]**	**Sr**$_5$ **[%]**
0°	94.3	85.5	83.3	84.0
30°	103.9	82.1	79.2	83.1
60°	109.7	83.2	78.5	80.8
90°	121.2	78.5	76.3	78.8

Table 9: Sr and rms computed for different rotator angles.

In conclusion, we recommend to enter additional corrections to the reference mode's configuration file (if possible) for angles close to 90°. These additional corrections would have to be computed ideally after 2 iterations, so that only the differential values compared to the bold set of coefficients of table 8 should be considered. In view of our results, it is likely that the two main terms to be corrected are a_4 and a_6. More generally, further calibrations should not neglect the rotator angle parameter for optimal corrections.

4.7 Encountered difficulties

A very first problem involving the FS delayed the beginning of my calibrations. It seems the FS was oscillating, causing an elongated PSF for long-exposure acquisitions. The repairing took two days, which forced me to wait until February 18th to begin the calibration procedure. This highlight the importance of NAOS calibrations, if the problem had not been fixed, it would have been of no use to do Phase Diversity. Similarly, a problem linked to CONICA on March 13th forced me to begin a day later during my second stay at Paranal. The problem was the persistence of noise columns on one or two (depending on time) of the upper-quadrants of CONICA's detector. To avoid biasing by these noise columns, my acquisitions were done on the two lower-quadrants.

A general feature concerning VLT instruments such as NaCo, is that they require frequent attention, either for daily calibrations, or maintenance operations. This fight for time, in which I had no priority, resulted in a necessity for maximal productivity during the unexploited hours of NaCo. Since, my alloted time was relatively tight, my calibrations had to overlap some maintenance operations in the dome, which required the opening of it and the moving of the telescope. In view of the Sr values of March 17th entry in table 3, the measurements that were done that day were seriously biased by these maintenance operations. Therefore, we do not give the results of the comparison between the different WFS modes (VIS 7x7, VIS 14x14, IR 7x7 (V0 and V1), IR 14x14) that was performed that day and which seemed also a bit suspicious at first sight.

Please note that these maintenance operations not only took place on March 17th, but also the 18th and 19th. No *a priori* degradation is reflected by the table showing the evolution in time of the results (table 3). Nevertheless, this fact only means that at the moment the test on the reference mode occured, no operation was done. It does not mean that measurements taken later could not have been influenced by maintenance operations. Therefore, suspicious results obtained on March 18th and 19th still have to be considered carefully (such as the degradation of the corrections for the Ks filter after one iteration).

Several basic changes in OPRA caller's code were attempted. Some were immediately succesful, such as the repairing of the bad pixel problem (a sub-algorithm had to be changed in order to avoid picking up hot pixels instead of true PSFs). Others, seeming *a priori* really basic, such as the writing of the resulting coefficients in an external file, turned out to be tougher and required an external help. The reason is that OPRA is written in Yorick, which compared to other languages (IDL, Python, MatLab) is relatively bad documented and whose community is also more limited. A recommendation would be to write it in *Python*, if time permitted.

As mentioned in section 4.6.2, we also faced other software difficulties while applying the sign inverted Zernike coefficients computed by OPRA to the window opened with the `cnsguiCONICAaberr` command. This misunderstanding led to a whole week spent to actions not linked to the primary objective. Only the last day was dedicated to iterations.

5 Conclusions and perspectives

5.1 Conclusion and perspectives from the results

First, the major result that has to be reminded is the sets of Zernike cofficients determined after 2 iterations (the bold set in table 8). It was indeed the original task that was demanded. We highly recommend to apply them to the ones currently in the configuration file. However, we recommend to iterate even more times, knowing now how to proceed. More iterations should allow to find more and more accurate sets of coefficients and eventually lead to the ultimate stability of the instrument. Such procedure has already been implemented successfully at Palomar observatory by Burruss et al. (2010).

The implementation of iterations also allowed to underline a modification that should be applied to the `cnstooTakePDData` script in order to perform a first iteration giving better corrections. Taking the initial defocus term into account indeed provided a jump of about 4 to 6 % in Sr, whereas improvements were uncertain when it was not. The gain obtained at the second step was then ranging between 1 and 3% of Sr, which though very slight should also be considered an increase since all of the methods show this jump.

Running the basic calibration procedure without iteration led us to the aberration coefficients that should be applied in the case of different filters. These coefficients were presented in table 6. In this case however, we prefer to recommend to re-run the procedure with several iterations in order to reach more accurate correction coefficients.

Another important result was the highlight of the rotator angle's effect on the aberrations. Further calibrations should take this parameter into account in order to reach optimal corrections.

Finally, at a secondary level, we proved that OPRA worked as well with 3 or 4 input PSFs, that the aberration corrections provided relatively stable results in time and that ESO pipeline do not give the most reliable Sr. We recommended to lower the size of the sub-image taken for the photometric calibration of the theoretical diffraction pattern. In the meantime, we used the MAD, MVD and Sridharan Sr meters to get accurate Sr computed and also assessed their error bars (respectively about 2, 2 and 3%).

5.2 Personal conclusion

From a personal viewpoint, this internship and more precisely the integration to the team formed by my supervisors was extremely rewarding. A first phase of assimilation of new concepts, techniques and knowledge allowed me to become familiar with NaCo, static aberrations calibration procedures, softwares used and later to the concept of Sr measurements as well. I also realized the importance of cooperation and communication between astronomers, useful to trade off softwares developed by different teams.

After this phase, and the context of my task within the framework of the NaCo calibration procedure being also clearly laid out, the team let me lead independently my task on NaCo instrument. However, I was never alone in case of questioning. Unexpected problems (FS misalignment, opening of the UT4 dome for maintenance, dysfunction/misunderstanding of the aberration coefficients corrector tool) punctuated my task, which got delayed, disturbed by external source of errors, and also more distant from the initial objective. Patience, adaptation capability, autonomous research and perseverance were practiced, as well as new languages such as IDL and Yorick.

Besides the characterization of different parameters' effects on the image quality, my work ended up in the discovery of a non-appropriate operation in the script performing phase diversity measurements. Its correction led to improvement of the Sr ratio in the consecutive measurements. This successful contribution constitutes a really valuable reward and meet the initial objective.

Finally, the writing phase brought me a lot as well, forcing me to go deeper on my own in the details of the topics tackled during the internship.

Looking to the future, this internship provided me a significant gain in experience to hopefully tackle one day issues linked to the so-considered successor of NaCo: SPHERE, whose arrival is going to be simultaneous to the beginning of my doctorate.

References

Amico, P., & Marchetti, E. (2007, May). Multi-Strehl Meter (MSM) for the LPO, User's manual 2.0 [Computer software manual].

Biller, B. A., Close, L. M., Masciadri, E., Nielsen, E., Lenzen, R., Brandner, W., et al. (2007, November). An Imaging Survey for Extrasolar Planets around 45 Close, Young Stars with the Simultaneous Differential Imager at the Very Large Telescope and MMT. *apjs*, *173*, 143-165.

Biller, B. A., Kasper, M., Close, L. M., Brandner, W., & Kellner, S. (2006, April). Discovery of a Brown Dwarf Very Close to the Sun: A Methane-rich Brown Dwarf Companion to the Low-Mass Star SCR 1845-6357. *apjl*, *641*, L141-L144.

Blanc, A., Fusco, T., Hartung, M., Mugnier, L. M., & Rousset, G. (2003, February). Calibration of NAOS and CONICA static aberrations. Application of the phase diversity technique. *aap*, *399*, 373-383.

Burruss, R. S., Serabyn, E., Mawet, D. P., Roberts, J. E., Hickey, J. P., Rykoski, K., et al. (2010, July). Demonstration of on sky contrast improvement using the modified Gerchberg-Saxton algorithm at the Palomar Observatory. In *Society of photo-optical instrumentation engineers (spie) conference series* (Vol. 7736).

Carreras, R. A., Restaino, S. R., & Duneman, D. C. (1994, September). Laboratory experiment using phase diversity to extract higher order Zernike coefficients. In T. J. Schulz & D. L. Snyder (Eds.), *Society of photo-optical instrumentation engineers (spie) conference series* (Vol. 2302, p. 323-329).

Chauvin, G., Lagrange, A.-M., Dumas, C., Zuckerman, B., Mouillet, D., Song, I., et al. (2005, August). Giant planet companion to 2MASSW J1207334-393254. *aap*, *438*, L25-L28.

Crepp, J. R., Pueyo, L., Brenner, D., Oppenheimer, B. R., Zimmerman, N., Hinkley, S., et al. (2011, March). Speckle Suppression with the Project 1640 Integral Field Spectrograph. *apj*, *729*, 132.

Cristian Herrera, G., Pompei, E., Girard, J., & Montagnier, G. (2010, August). NaCo Survival Guide for TIO's and Astronomers [Computer software manual]. Karl-Schwarzschild-Str.2, 85748 Garching bei Munchen, Germany.

Eckart, A., Schödel, R., Meyer, L., Trippe, S., Ott, T., & Genzel, R. (2006, August). Polarimetry of near-infrared flares from Sagittarius A*. *aap*, *455*, 1-10.

Ekstrom, M. P., & Rhoads, R. L. (1974, March). On the Application of Eigenvector Expansions to Numerical Deconvolution. *Journal of Computational Physics*, *14*, 319.

Fienup, J. R. (1982, August). Phase retrieval algorithms: a comparison. *ao*, *21*, 2758-2769.

Gerdes, R., Beletic, J. W., & Duvarney, R. C. (1998, July). Design concepts for a fast-readout low-noise CCD controller. In S. D'Odorico (Ed.), *Society of photo-optical instrumentation engineers (spie) conference series* (Vol. 3355, p. 520-528).

Girard, J. (2011, June). Very Large Telescope NaCo User Manual [Computer software manual]. Karl-Schwarzschild-Str.2, 85748 Garching bei Munchen, Germany.

Hartmann, J. (1900, June). Remarks on the Construction and Adjustment of Spectrographs. I. *apj*, *11*, 400.

Hartung, M., Blanc, A., Fusco, T., Lacombe, F., Mugnier, L. M., Rousset, G., et al. (2003, February). Calibration of NAOS and CONICA static aberrations. Experimental results. *aap*, *399*, 385-394.

Janson, M., Bergfors, C., Goto, M., Brandner, W., & Lafrenière, D. (2010, February). Spatially Resolved Spectroscopy of the Exoplanet HR 8799 c. *apjl*, *710*, L35-L38.

Janson, M., Brandner, W., Henning, T., Lenzen, R., McArthur, B., Benedict, G. F., et al. (2007, June). NACO-SDI Direct Imaging Search for the Exoplanet ϵ Eri b. *aj*, *133*, 2442-2456.

Jenkins, J. S., Jones, H. R. A., Biller, B., O'Toole, S. J., Pinfield, D. J., Close, L., et al. (2010, June). NACO-SDI imaging of known companion host stars from the AAPS and Keck planet search surveys. *aap*, *515*, A17.

Kendrick, R. L., Acton, D. S., & Duncan, A. L. (1994, September). Phase-diversity wave-front sensor for imaging systems. *ao*, *33*, 6533-6546.

Lacombe, F., Zins, G., Charton, J., Chauvin, G., Dumont, G., Feautrier, P., et al. (2002). Naos: from an ao system to an astronomical instrument.

Lafrenière, D., Marois, C., Doyon, R., Nadeau, D., & Artigau, É. (2007, May). A New Algorithm for Point-Spread Function Subtraction in High-Contrast Imaging: A Demonstration with Angular Differential Imaging. *apj*, *660*, 770-780.

Lagrange, A.-M., Bonnefoy, M., Chauvin, G., Apai, D., Ehrenreich, D., Boccaletti, A., et al. (2010, July). A Giant Planet Imaged in the Disk of the Young Star β Pictoris. *Science*, *329*, 57-.

Lee, D. J., Welsh, B. M., Roggemann, M. C., & Ellerbroek, B. L. (1997, July). Diagnosing unknown aberrationsin an adaptive optics system by use of phase diversity. *Optics Letters*, *22*, 952-954.

Lenzen, R., Hartung, M., Brandner, W., Finger, G., Hubin, N. N., Lacombe, F., et al. (2003, March). NAOS-CONICA first on sky results in a variety of observing modes. In M. Iye & A. F. M. Moorwood (Eds.), *Society of photo-optical instrumentation engineers (spie) conference series* (Vol. 4841, p. 944-952).

Lidman, C., Ageorges, N., & Soenke, C. (2009). NACO - Technical Templates (v1.3. ed.) [Computer software manual].

Löfdahl, M. G., Scharmer, G. B., & Wei, W. (2000, January). Calibration of a Deformable Mirror and Strehl Ratio Measurements by Use of Phase Diversity. *ao*, *39*, 94-103.

MacGovern, A. J., & Wyant, J. C. (1971, March). Computer generated holograms for testing optical elements. *ao*, *10*, 619.

Magette, A. (2010). *The International Liquid Mirror Telescope: optical testing and alignment using a Nijboer-Zernike aberration-retrieval approach.* Unpublished doctoral dissertation.

Mahajan, V. N. (1981). Zernike annular polynomials for imaging systems with annular pupils. *Journal of the Optical Society of America (1917-1983)*, *71*, 75-85.

Marco, O., Ageorges, N., Mathys, G., & Gilmozzi, R. (2003, October). Naos-conica operation manual [Computer software manual]. Karl-Schwarzschild-Str.2, 85748 Garching bei Munchen, Germany.

Marechal, Y., Coulomb, J. L., Meunier, G., & Touzot, G. (1994, September). Use of the diffuse approximation method for electromagnetic field computation. *IEEE Transactions on Magnetics*, *30*, 3558-3561.

Mayor, M., & Queloz, D. (1995, November). A Jupiter-mass companion to a solar-type star. *nat*, *378*, 355-359.

Montagnier, G., Segransan, D., Beuzit, J.-L., Udry, S., Mayor, M., & Forveille, T. (2007, June). Characterization of the Brown Dwarf Desert Around Solar Neighborhood G & K dwarfs using NACO-SDI. In *In the spirit of bernard lyot: The direct detection of planets and circumstellar disks in the 21st century.*

Noll, R. J. (1976, March). Zernike polynomials and atmospheric turbulence. *Journal of the Optical Society of America (1917-1983)*, *66*, 207-211.

O'Neal, J. (2012, February). *Proposed NaCo Maintenance Calibration Plan.* Memo.

Ragazzoni, R., & Farinato, J. (1999, October). Sensitivity of a pyramidic Wave Front sensor in closed loop Adaptive Optics. *aap*, *350*, L23-L26.

Roberts, L. C., Jr., Perrin, M. D., Marchis, F., Sivaramakrishnan, A., Makidon, R. B., Christou, J. C., et al. (2004, October). Is that really your Strehl ratio? In D. Bonaccini Calia,

B. L. Ellerbroek, & R. Ragazzoni (Eds.), *Society of photo-optical instrumentation engineers (spie) conference series* (Vol. 5490, p. 504-515).

Roddier, C., Roddier, F., Stockton, A., Pickles, A., & Roddier, N. (1990, July). Testing of telescope optics - A new approach. In L. D. Barr (Ed.), *Society of photo-optical instrumentation engineers (spie) conference series* (Vol. 1236, p. 756-766).

Ronchi, V. (1964, April). Forty years of history of a grating interferometer. *ao*, *3*, 437.

Rousset, G., Lacombe, F., Puget, P., Gendron, E., Arsenault, R., Kern, P. Y., et al. (2000, July). Status of the VLT Nasmyth adaptive optics system (NAOS). In P. L. Wizinowich (Ed.), *Society of photo-optical instrumentation engineers (spie) conference series* (Vol. 4007, p. 72-81).

Rousset, G., Lacombe, F., Puget, P., Hubin, N. N., Gendron, E., Fusco, T., et al. (2003, February). NAOS, the first AO system of the VLT: on-sky performance. In P. L. Wizinowich & D. Bonaccini (Eds.), *Society of photo-optical instrumentation engineers (spie) conference series* (Vol. 4839, p. 140-149).

Sanchez-Bermudez, J., Schoedel, R., Alberdi, A., & Pott, J. U. (2012, March). NACO/SAM observations of sources at the Galactic Center. *ArXiv e-prints*.

Sauvage, J.-F., Fusco, T., Rousset, G., & Petit, C. (2007, August). Calibration and precompensation of noncommon path aberrations for extreme adaptive optics. *Journal of the Optical Society of America A*, *24*, 2334-2346.

Schödel, R., Merritt, D., & Eckart, A. (2009, July). The nuclear star cluster of the Milky Way: proper motions and mass. *aap*, *502*, 91-111.

Schödel, R., Ott, T., Genzel, R., Hofmann, R., Lehnert, M., Eckart, A., et al. (2002, October). A star in a 15.2-year orbit around the supermassive black hole at the centre of the Milky Way. *nat*, *419*, 694-696.

Shack, R. B., & Platt, B. C. (1971). Lenticular Hartmann-screen. *J. Opt. Soc. Am. A*, *61*, 656.

Spanoudakis, P., Zago, L., Chetelat, O., Gentsch, R., & Mato Mira, F. (2000, July). Extremely high resolution tip-tilt-piston mirror mechanism for the VLT-NAOS field selector. In P. L. Wizinowich (Ed.), *Society of photo-optical instrumentation engineers (spie) conference series* (Vol. 4007, p. 408-415).

Strehl, K. (1901).
Z. f. Instrumkde, *22*, 213.

Thelen, B. J., Paxman, R. G., Carrara, D. A., & Seldin, J. H. (1999, May). Maximum a posteriori estimation of fixed aberrations, dynamic aberrations, and the object from phase-diverse speckle data. *Journal of the Optical Society of America A*, *16*, 1016-1025.

Zernike, F. (1934, May). Beugungstheorie des schneidenver-fahrens und seiner verbesserten form, der phasenkontrastmethode. *Physica*, *1*, 689-704.

Appendices

Appendix A
Logbook

January 27th, 2012

Arrival in Santiago.

From January 30th to February 3rd

Specification of problem by J. Girard and D. Mawet:

Jan. 30th	Introduction to Adaptive Optics and NaCo by D. Mawet.
Jan. 31th	Introduction to NaCo and specification of problem by J. Girard.
Feb. 2nd	Introduction to OPRA and Yorick language by J. Girard.
Feb. 3rd	Specification of objectives and drafting of the schedule of my internship.

From February 16th to February 19th

First run at Paranal, supervised by D. Mawet:

Feb. 16th	Description of NaCo at the UT4 workstation, visit of NaCo in the UT4 dome and attempts to fix the FS problem.
Feb. 17th	Introduction to the user interface (SOS, NAOS ICS, CONICA ICS) and attempts to fix the FS problem.
Feb. 18th	Problem fixed. First runs of the calibration procedure with both S13 and S27 cameras.
Feb. 19th	Second run of the calibration procedure with the reference mode.

From February 24th to March 6th

Processing of the calibration data with OPRA:

Feb. 24th	Discussion with J. Girard about the results obtained during the first run.
Feb. 27,28th	Analysis of the calibration data taken by D. Mawet on Feb. 24th at different rotator angles with OPRA.
Feb. 29th	Modification of the `opra\_caller.i` file in order to fix the hot-pixel pickup problem.
Mar. 2nd	Modification of the `opra\_caller.i` file in order to write the results in an external file and save the phase map in a fits file.
Mar. 6th	Plot of the computed Zernike coefficients for different rotator angles.

From March 13th to March 19th

Second run at Paranal, supervised by J. Girard and J. ONeal:

Mar. 13th	Discussions about the CONICA detector's upper-quadrants problem. Comparison between the results provided by 3 and 4 PSFs with OPRA.
Mar. 14th	Introduction to the MAD Strehl meter by J. Girard. Run of the calibration procedure and first attempt to iterate. These attempts to iterate did not provide better results, involving a change of the initial objectives. Acquisition of data at different rotator angles in order to confirm data taken by D. Mawet on Feb. 24th.
Mar. 15th	The gain in autonomy of yesterday allows me to be self-sufficient with the procedure today. The data taken at different rotator angles yesterday were spurious. New acquisition of data at different rotator angles and run of the PD procedure with different filters.
Mar. 16th	Introduction to RS and IM by J. O'Neil. Run of the calibration procedure before and after new RS and new IM for the IR WFS modes, and analysis of results.
Mar. 17th	The ambiguous results of yesterday encouraged me to take new acquisitions with new RS and IM today. I also ran the calibration procedure for all the different WFS modes. The results show that there were likely contamined by maintenance operations in the dome.
Mar. 18th	New run of the procedure before and after new RS. Continuation of the tests with different filters.
Mar. 19th	New run of the procedure before and after new RS. New attempt to iterate the calibration procedure with the NB_2.17 filter. This time it works. The non-convincing results obtained on Mar. 14th was due to a misunderstanding of the `cnsguiConicaAberr` panel. Two iterations were applied with the NB_2.17 filter and one iteration with the Ks filter.

From March 26th to April 19th

Analysis of the data taken during the second run, application of the different Sr measurement methods and redaction of the report:

Mar. 26th	Discussion with J. Girard about the results obtained during the second run. Directives for the data reduction.
Mar. 27th	Improvement of knowledge about the Strehl ratio and its computation methods.
Mar. 29th	Installation and first attempts to use MAD, Sridharan and MVD Sr meters.
Mar. 30th	Determination of MAD's optimal parameters (sub-image and bckg box sizes).
Apr. 2nd	Estimate of the MAD Sr meter error bars through the computation of Sr with different sub-image and background box sizes.
Apr. 4th	Use of MAD's optimal set of parameters to compute the Sr of all acquired images.
Apr. 5th	Comparison of the Sr ratios obtained with the ESO pipeline, OPRA, and MAD.
Apr. 9th	Implementation of an IDL code computing the VLT pupil.
Apr. 10th	Measurement of all the acquired images's Sr with the MVD Sr meter, fed with the newly created VLT pupil.
Apr. 16th	Informal presentation of the results to my supervisors.
Apr. 19th	Summarized personal recommendations to my supervisors in order to improve the static calibration procedure.

April 24th

Return in Belgium.

Appendix B
OPRA caller

A copy of the OPRA caller code is attached hereunder. We also give some useful advice to facilitate the understanding of the code:

- The more defocused, the longer the DIT, in order to have similar fluxes for all input images.
- / denotes the beginning of comments.
- `.i` denotes a Yorick file.
- `plh` allows to plot a graph in the opened window.

```
// RUNNING OPRA FROM THE TERMINAL:
// cd /Users/valentinchristiaens/OPRA/
// yorick
// #include "./opra_caller_jon.i"
// (then apply coefficients with -1 factor using the cnsguiConicaAberr panel)

require,"opra.i";
#include "lmfit.i"

// Used to convert nm rms defocus to radians:
ffocus = 0.6*0.7;

path = "/Users/valentinchristiaens/OPRA/DATA/Test_PDNACO_NB217_2012-02-18/";
psf_name_tmp =  path + "NAOS_PSF_Fiber500_NB_2.17_FLM13_S13_CL_F";
psf_dark_name_tmp = path + "NAOS_BCKG_Fiber500_NB_2.17_FLM13_S13_";

dit1 = 2.0;
psf1_name = psf_name_tmp + "0_2s.fits";
psf1_dark_name = psf_dark_name_tmp + "2s.fits";
psf1_defocus = 0;

dit2 = 4.0;
psf2_name = psf_name_tmp + "400_4s.fits";
psf2_dark_name = psf_dark_name_tmp + "4s.fits";
psf2_defocus = 4.0*ffocus;

dit3 = 7.0;
psf3_name = psf_name_tmp + "800_7s.fits";
psf3_dark_name = psf_dark_name_tmp + "7s.fits";
psf3_defocus = 8.0*ffocus;

dit4 = 12.0;
psf4_name = psf_name_tmp + "1200_12s.fits";
psf4_dark_name = psf_dark_name_tmp + "12s.fits";
psf4_defocus = 12.0*ffocus;
```

```
/*-------------PSF1-----------------*/
im1 = fits_read( psf1_name );

//1. Dark Subtraction
d = fits_read( psf1_dark_name );
im1 = im1 - d;

//2. Crop
m = where(im1 == max(im1));
xy = indices(dimsof(im1)(2));
xc = long((xy(*,1)(m))(1));
yc = long((xy(*,2)(m))(1));
ss = 128;
im2 = im1(xc-ss/2:xc+ss/2-1,yc-ss/2:yc+ss/2-1);

//3. Sigma Filtering
im3 = sigmaFilter(im2,5,iter=5);

//4. Clipping/normalization:
psf1 = clip(im3,0.,);
sumpsf1 = sum( psf1 );
psf1 /= sumpsf1;

output_name = path + "psf1.fits"
//fits_write,output_name,im3

/*-------------PSF2-----------------*/
im1 = fits_read( psf2_name );

//1. Dark Subtraction
d = fits_read( psf2_dark_name );
im1 = im1 - d;

//2. Crop
m = where(im1 == max(im1));
xy = indices(dimsof(im1)(2));
xc = long((xy(*,1)(m))(1));
yc = long((xy(*,2)(m))(1));
ss = 128;
im2 = im1(xc-ss/2:xc+ss/2-1,yc-ss/2:yc+ss/2-1);

//3. Sigma Filtering
im3 = sigmaFilter(im2,5,iter=5);

//4. Clipping/normalization:
psf2 = clip(im3,0.,);
psf2 /= ( sumpsf1*dit2/dit1 );
```

```
//psf2 /= sum( psf2 );

output_name = path + "psf2.fits";
//fits_write,output_name,im3

/*-------------PSF3-----------------*/
im1 = fits_read( psf3_name );

//1. Dark Subtraction
d = fits_read( psf3_dark_name );
im1 = im1 - d;

//2. Crop
m = where(im1 == max(im1));
xy = indices(dimsof(im1)(2));
xc = long((xy(*,1)(m))(1));
yc = long((xy(*,2)(m))(1));
//overwrite values for this one as it is too much out of focus...
//xc = 512;
//yc = 423;
ss = 128;
im2 = im1(xc-ss/2:xc+ss/2-1,yc-ss/2:yc+ss/2-1);

//3. Sigma Filtering
im3 = sigmaFilter(im2,5,iter=5);

//4. Clipping/normalization:
psf3 = clip(im3,0.,);
psf3 /= ( sumpsf1*dit3/dit1 );
//psf3 /= sum( psf3 );

output_name = path + "psf3.fits";
//fits_write,output_name,im3

/*-------------PSF4-----------------*/
im1 = fits_read( psf4_name );

//1. Dark Subtraction
d = fits_read( psf4_dark_name );
im1 = im1 - d;

//2. Crop
m = where(im1 == max(im1));
xy = indices(dimsof(im1)(2));
xc = long((xy(*,1)(m))(1));
yc = long((xy(*,2)(m))(1));
//overwrite values for this one as it is too much out of focus...
//xc = 512;
//yc = 423;
```

```
ss = 128;
im2 = im1(xc-ss/2:xc+ss/2-1,yc-ss/2:yc+ss/2-1);

//3. Sigma Filtering
im3 = sigmaFilter(im2,5,iter=5);

//4. Clipping/normalization:
psf4 = clip(im3,0.,);
psf4 /= ( sumpsf1*dit4/dit1 );
//psf4 /= sum( psf4 );

output_name = path + "psf4.fits";
//fits_write,output_name,im3;

/*---------Evaluate Noise---------------*/
noise = psf1(1:50,1:50)(*)(rms);

/*---------And Lets Go!!----------------*/

nmodesmax=25;

opp = opra([psf1,psf2,psf3,psf4], [psf1_defocus,psf2_defocus,psf3_defocus,
psf4_defocus], 2.166e-6, 0.01327, 8.0, cobs=0.1, nmodes=nmodesmax, noise=noise,
use_mode="zernike", fix_amp=[], progressive=[], nm=1);

coefs = *( ( *opp.coefs )( 1 ) );

\\ Plot of the coefficients
window,1;fma;
plh, -coefs(4:19+2)*1000*2.166/(2*pi),indgen(numberof(coefs(4:19+2)))+3, marks=0;
xytitles,"Zernike #","nm rms";
```

Appendix C
NaCo instrument

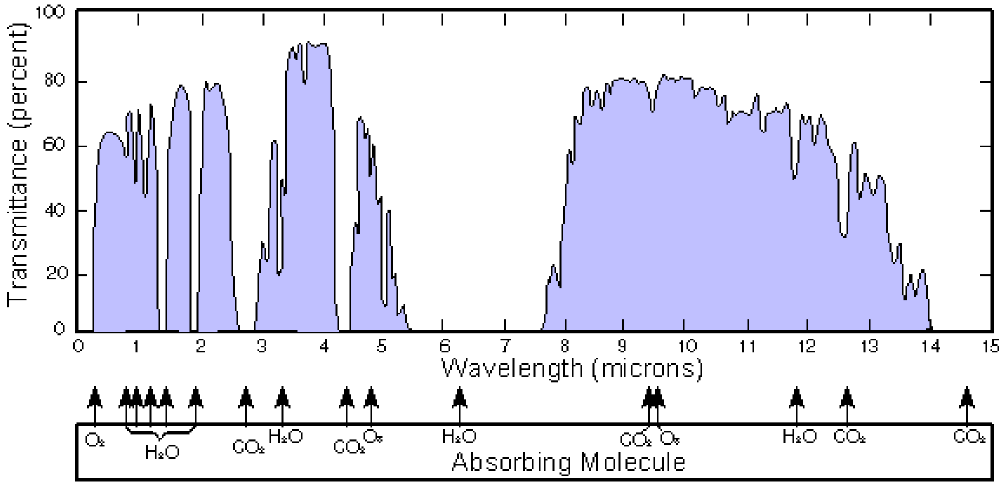

Figure 26: Main atmospheric IR windows. The infrared domain is divided in several astronomical bands which correspond to the main infrared windows, in which the Earth's atmosphere is transparent.

Astronomical band	**Wavelength range [μm]**
R and I bands	0.65 to 1.0
J band	1.1 to 1.4
H band	1.5 to 1.8
K band	2.0 to 2.4
L band	3.0 to 4.0
M band	4.6 to 5.0
N band	7.5 to 14.5

Table 10: Main infrared bands. As mentioned in section 3, NaCo's spectral range is from J band to M band (1 to 5 μm).

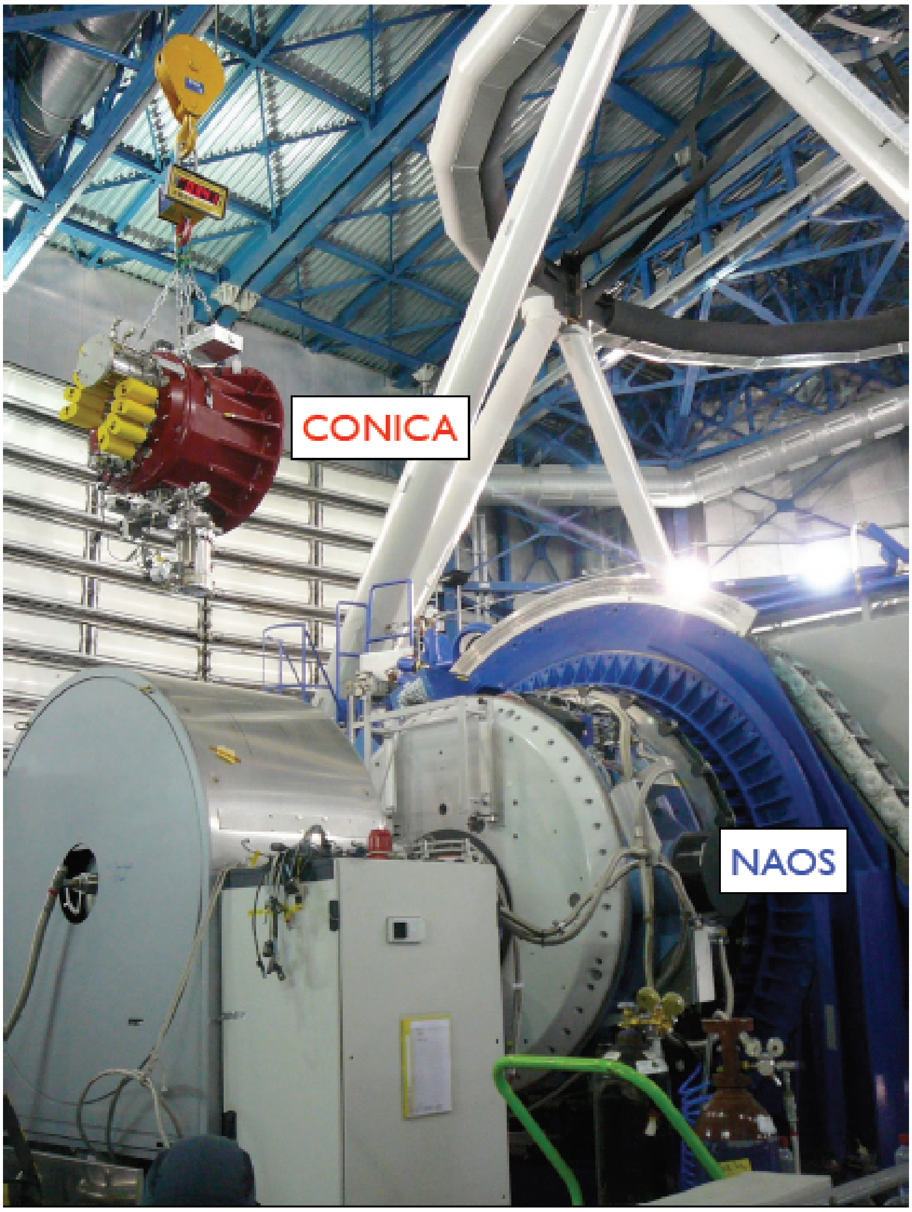

Figure 27: NaCo instrument during November 2009 intervention (Courtesy of J. Girard).

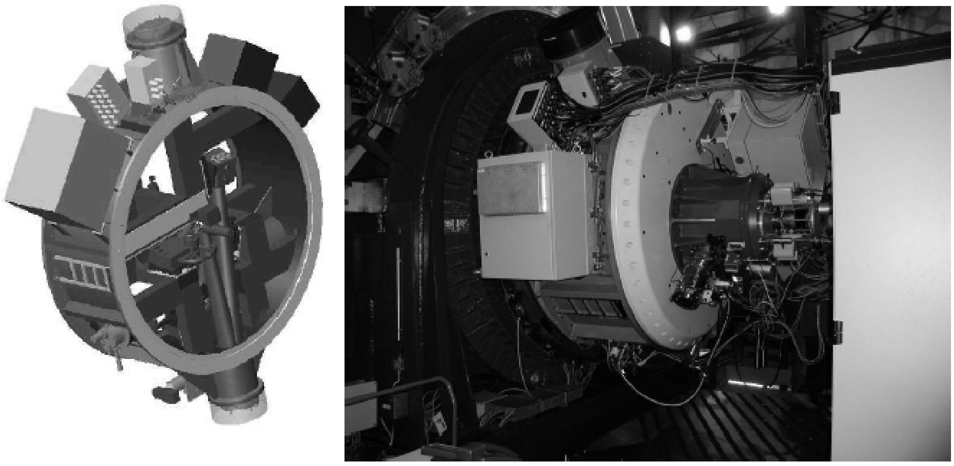

Figure 28: Left: NAOS Adapter. Right: NAOS + CONICA are attached to the Nasmyth adapter-rotator (Rousset et al., 2003).

Operation	Scheduled time	Description
Science calibrations	end of night or morning	Aim at taking the calibration frames needed to reduce science data taken during the night (dark, flat,...).
Periodic calibrations	daytime	Aim at controlling the instrument performances and monitor its health.
Check List	daytime	E.g cleaning directories, checking the pipeline products.
Preparation for the night	twilight	E.g. startup of the instrument, check of instrument performances.
Science	nighttime	Science or calibration observations.
Report/classification	night	Report/classification of observations.

Table 11: Overview of NaCo operations.

Actor	Responsibility
Paranal Observatory	Overall responsibility of the instrument on site (safety, maintenance, operations, interventions)
Paranal Engineering Department	Preventive and corrective maintenance, upgrades and functional operation.
Paranal Science Operations	Operates the instrument within the global scheme established for the VLT Science Operations
Instrument Scientist (J. Girard) 2nd ISs (D.Mawet & G. Hau)	Maintenance of NaCo within the Science Operation scheme (e.g. calibration plan, template definitions, maintenance of User and Operating manuals, Operating manuals, pipeline requirements, configuration control of the operating tools, instrument testing, performance monitoring, delivery of the Instrument Packages).
Telescope and Instrument Operator	Telescope + instrument operation and safety at night, shares the night instrument operation with the night astronomer.
Night Astronomer	In charge of the night observations (e.g. quality control classification, nighttime calibrations, correctness of the daytime science calibrations).
Day Astronomer	Execution and QC of the daytime science calibrations, preparation of the instrument for the following night
DFS Group (in Garching)	Development of new pipeline functionalities, maintenance of the existing recipes, configuration control
USD (led by L. Tacconi-Garman)	User Support during proposal preparation (review and certification)
QCG (led by W. Hummel)	Quality Control: data reduction, final certification and distribution of the science data gathered
Instrument Operation Team	Gathers representatives from Paranal (IS, Astronomers), and Garching (pipeline, USG and QCG); acts as a coordination and information channel; led by the IS.

Table 12: Overview of the different actors of NaCo and their responsibilities.

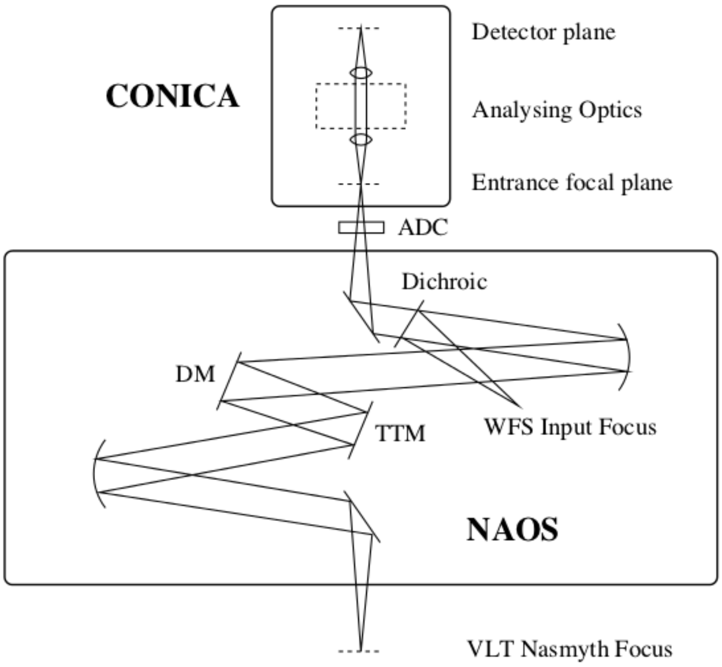

Figure 29: NaCo outline (Hartung et al., 2003).

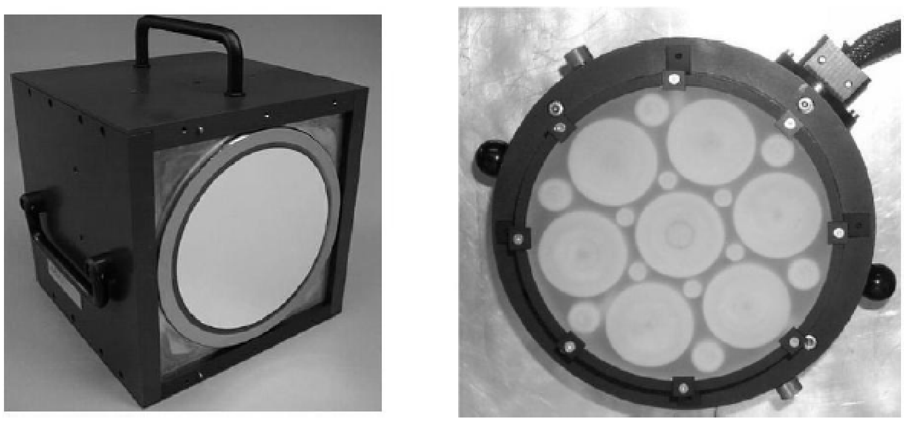

Figure 30: AO mirrors. Left: TTM. Right: DM. (Rousset et al., 2003).

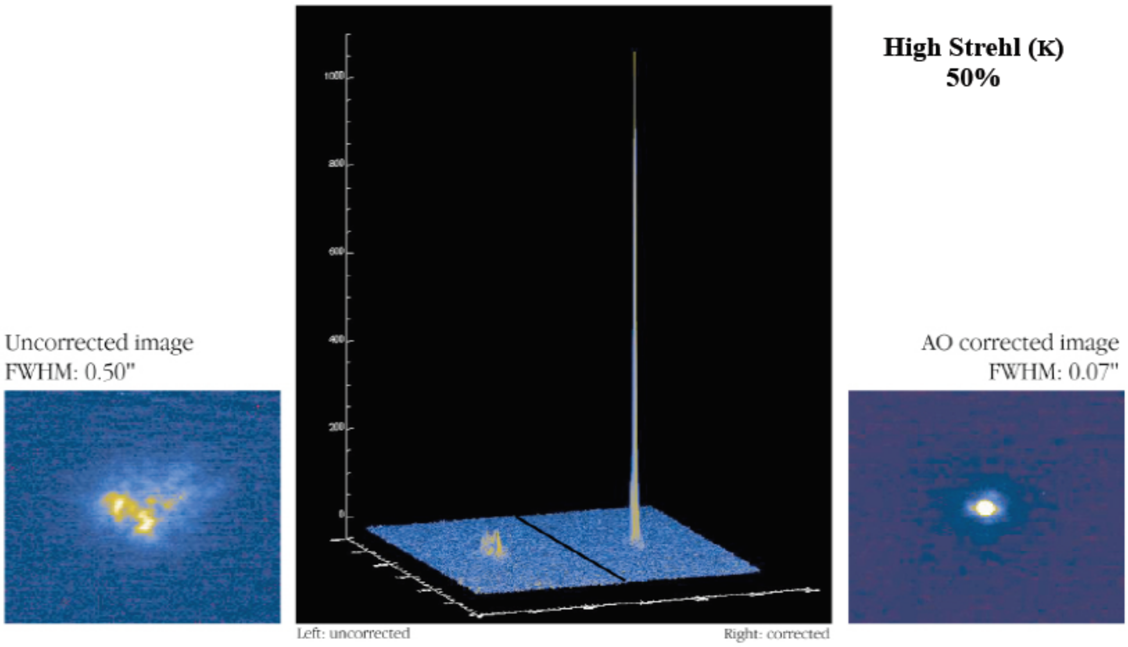

Figure 31: First light of NaCo. Left: uncorrected image. Right: AO corrected image enables a 50 % Sr in K band (Girard, 2011).

Dichroic or BS name	**Reflected light to the WFS & Efficiency**	**Transmitted light to CONICA & Efficiency**	**Use**
VIS	V → I 0.46 → 0.95 μm 90 %	J → M 1.05 → 5.0 μm 90 %	Observations in near-IR with optical WFS
N20C80	V → K 0.45 → 2.55 μm 20 %	V → K 0.45 → 2.55 μm 80 %	Observations and WFS both in the near-IR
N90C10	V → K 0.45 → 2.55 μm 10 %	V → K 0.45 → 2.55 μm 90 %	Observations and WFS both in the near-IR
JHK	I → K 0.80 → 2.55 μm 90 %	L → M 2.8 → 5.5 μm 10 %	Observations in the thermal-IR and WFS in the near-IR
K	K 1.9 → 2.55 μm 90 %	V → H 0.45 → 1.8 μm 90 %	J,H band observations and WFS in the K band

Table 13: Characteristics of dichroics and beam splitters of NaCo (Girard, 2011).

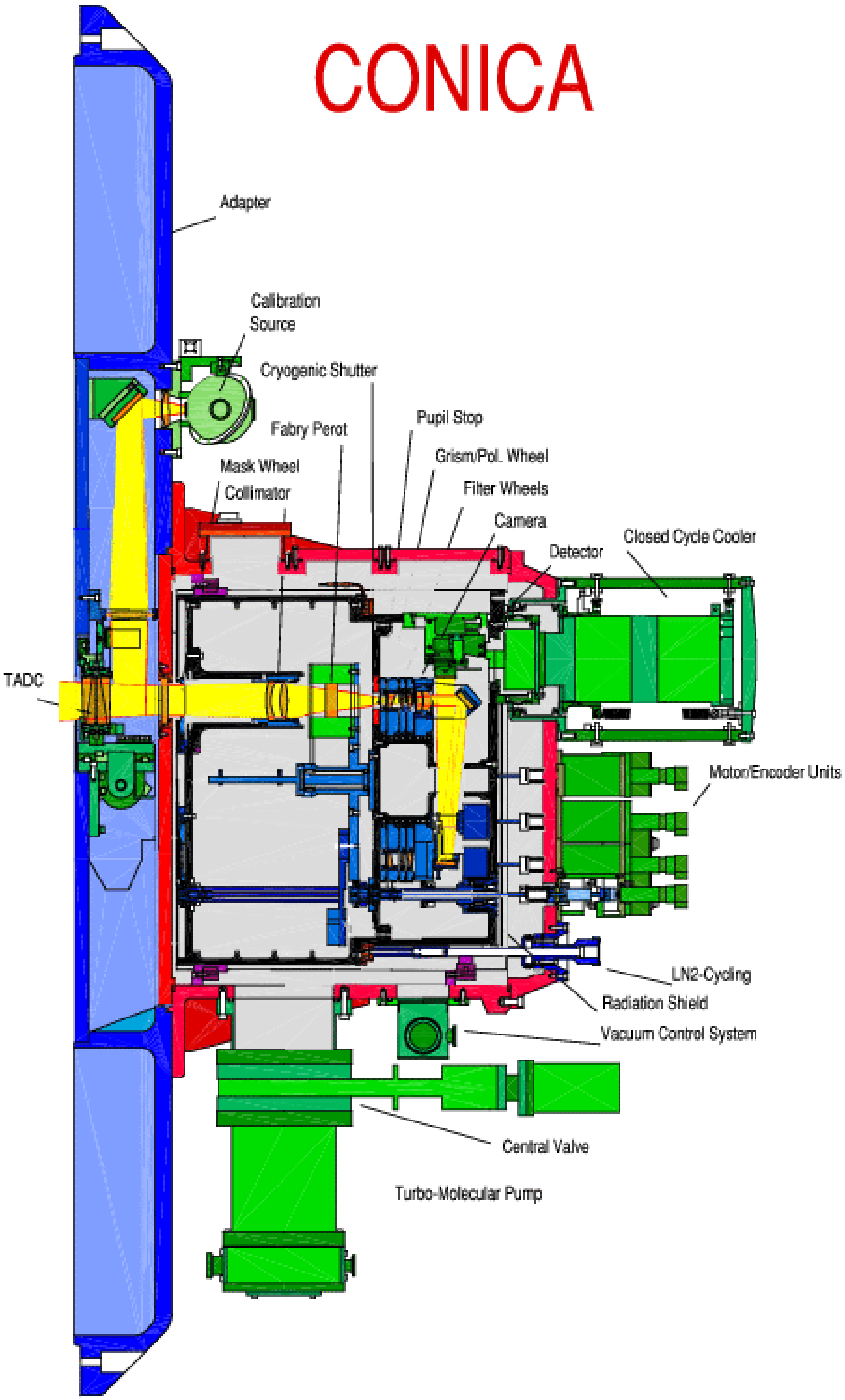

Figure 32: Schematic view of CONICA (courtesy of J. Girard).

Characteristics	Visible WFS	Infrared WFS
Wavelength range	0.45 - 1.0 μm	0.8 - 2.5 μm
FOV per lenslet 14x14 7x7	 2.32" 4.64"	 1.5, 2.92 or 4.38" 4.8" (V0) or 5.15" (V1)
Magnitude range 14x14 7x7	 0 - 12 12 - 16.7	 4 - 9 9 - 12
Detector	128x128 EEV CCD	1024x1024 Rockwell Hawaii

Table 14: Characteristics of the two WFS. (Girard, 2011).

Readout mode	**Detector mode**	**RON**	**Gain**	**Full** Well	**Min** DIT
FowlerNSamp(SW)	HighSensitivity	1.3	12.1	7500	1.7927
Double_RdRstRd(SW)	HighDynamic	4.2	11.0	15000	0.3454
Uncorr (LW NB Im.)	HighDynamic	4.4	11.0	15000	0.1750
Uncorr (LW Lp Im.)	HighWellDepth	4.2	9.8	22000	0.1750
Uncorr (LW Mp Im.)	HighBackground	4.2	9.0	28000	0.0560

Table 15: CONICA detector readout modes with the corresponding allowed saturation levels. SW = Short wavelengths (< 2.5 μm), LW = Long wavelengths (< 2.5 μm). RON is Readout noise and is expressed in ADU, gain is expressed in e-/ADU, the full well capacity is also in ADU, and the minimum DIT is in seconds. (Girard, 2011).

Camera	**Wavelength range**	**Scale (mas/px)**	**FOV**	**Sampling**
S13	1 - 2.5 μm	13.27	13.5"x13.5"	J
S27	1 - 2.5 μm	27.03	27.6"x27.6"	Ks
S54	1 - 2.5 μm	54.3	55.6"x55.6"	under
L27	2.5 - 5 μm	27.12	27.6"x27.6"	Lp
L54	2.5 - 5 μm	54.67	55.6"x55.6"	M

Table 16: Characteristics of the different CONICA cameras (Marco et al., 2003).

Band	**J**	**H**	**Ks**	**L'**	**M'**
λ/D (mas)[29]	32	42	56	98	123
Sky background (mag)	16.0	14.0	13.0	3.0	-0.5
Limiting magnitude	24.05	24.05	23.35	18.55	15.15

Table 17: Magnitude limits with the NAOS visual dichroic. Values are computed assuming the use of the NAOS visual dichroic. The given limiting magnitude is the 5-sigma value in 1 hour using a V=11.5 mag reference star located 10 arcsec away from the (point) source, with a visible seeing of 0.8 arcsec. For narrow band (hereafter NB) filters, subtract 2 to 3 magnitudes (Cristian Herrera et al., 2010).

Filter name	**Line**	λ_c [μm]	**FWHM** [μm]	**Max. Transmission** [%]
J	1.265	-	0.25	78
H	1.66	-	0.33	77
Ks	2.18	-	0.35	70
Lp	3.80	-	0.62	95
Mp	4.78	-	0.59	91
NB_1.04	-	1.040	0.015	62
NB_1.083	He I	1.083	0.015	65
NB_1.094	Paschen gamma	1.094	0.015	64
NB_1.24	-	1.237	0.015	60
NB_1.26	Fe II	1.257	0.014	60
NB_1.28	Paschen beta	1.282	0.014	62
NB_1.64	Fe II	1.644	0.018	47
NB_1.75	-	1.748	0.026	72
NB_2.12	H_2 (1-0) S(1)	2.122	0.022	55
NB_2.17	Brackett gamma	2.166	0.023	52
NB_3.74	Pfund gamma	3.740	0.02	92
NB_4.05	Brackett alpha	4.051	0.02	89
IB_2.00	-	2.00	0.06	68
IB_2.03	-	2.03	0.06	64
IB_2.06	-	2.06	0.06	66
IB_2.09	-	2.09	0.06	62
IB_2.12	-	2.12	0.06	59
IB_2.15	-	2.15	0.06	60
IB_2.18	-	2.18	0.06	61
IB_2.21	-	2.21	0.06	58
IB_2.24	-	2.24	0.06	57
IB_2.27	-	2.27	0.06	51
IB_2.30	-	2.30	0.06	55
IB_2.33	-	2.33	0.06	54
IB_2.36	-	2.36	0.06	56
IB_2.39	-	2.39	0.06	53
IB_2.42	-	2.42	0.06	52
IB_2.45	-	2.45	0.06	57
IB_2.48	-	2.48	0.06	53

Table 18: Characteristics of CONICA's filters (Girard, 2011).

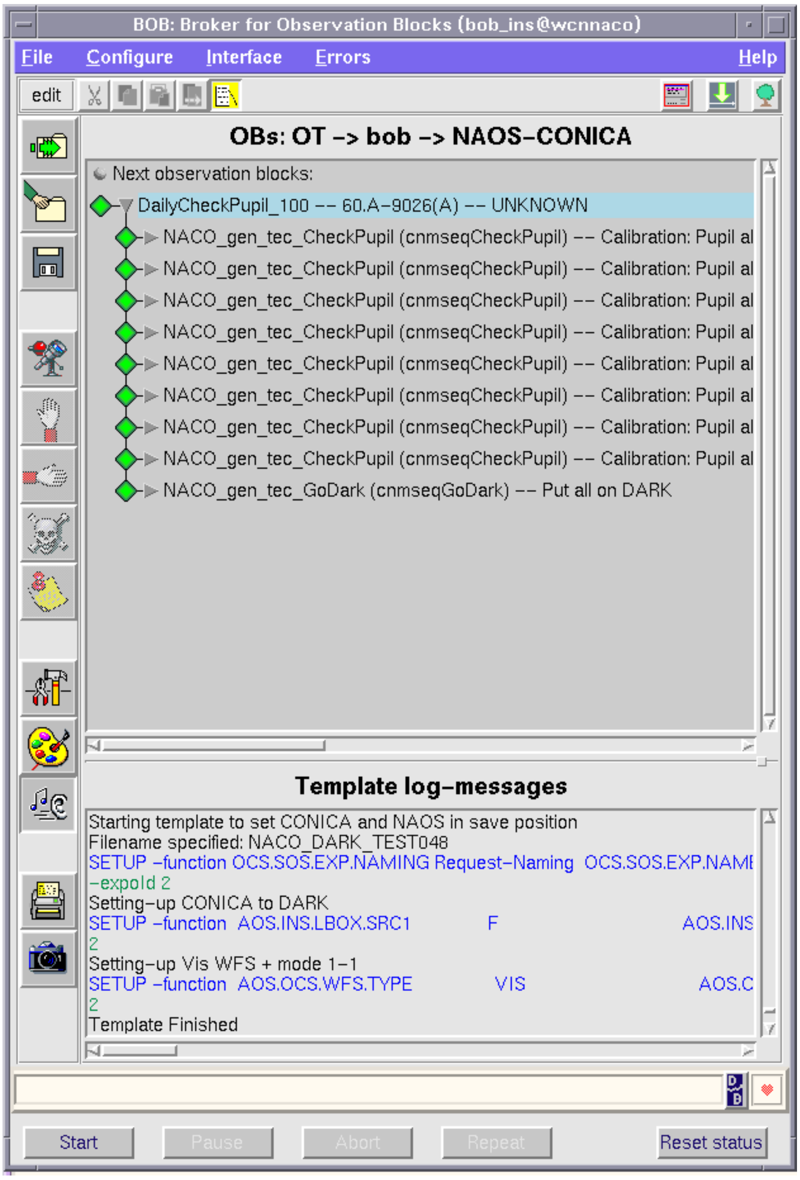

Figure 33: View of the Browser for Observing Blocks after it has finished to run the DailyCheck-Pupil OB.

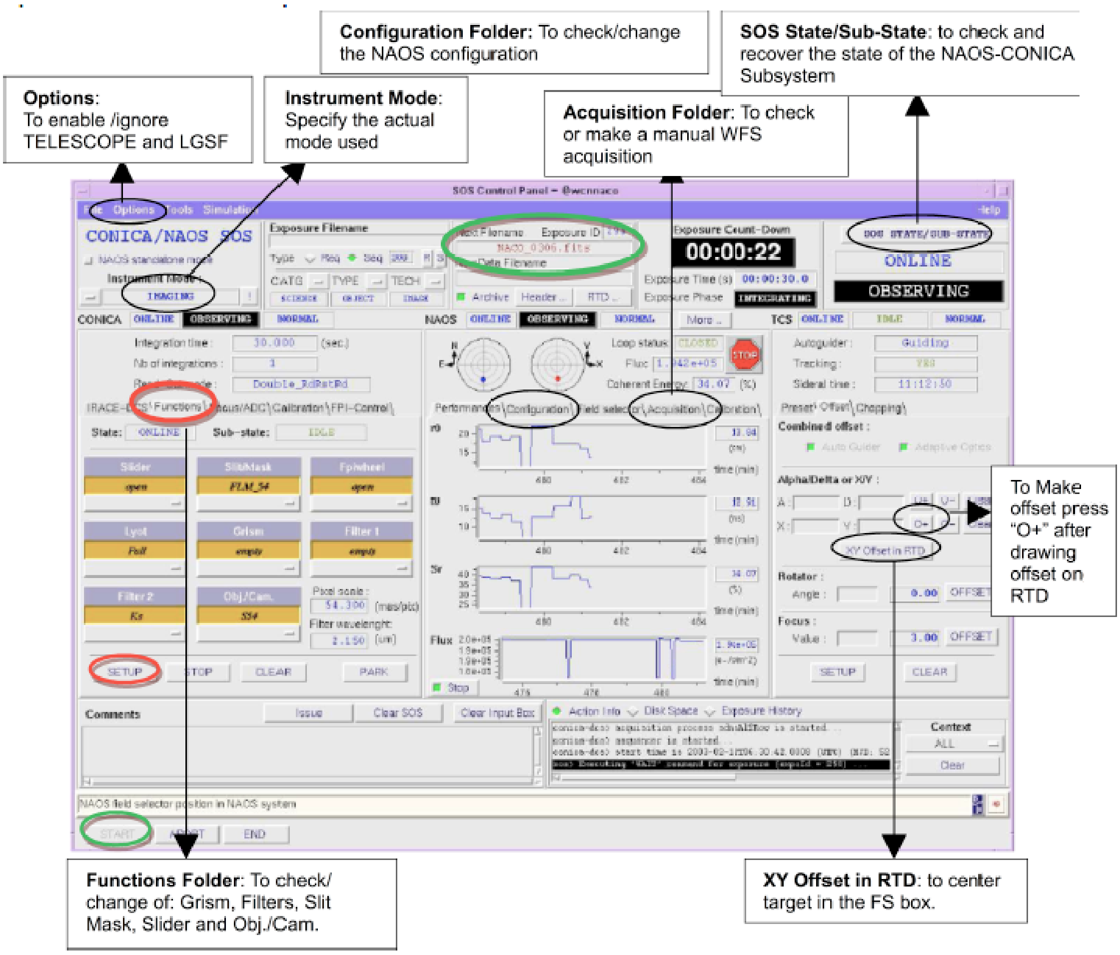

Figure 34: NaCo SOS control panel.

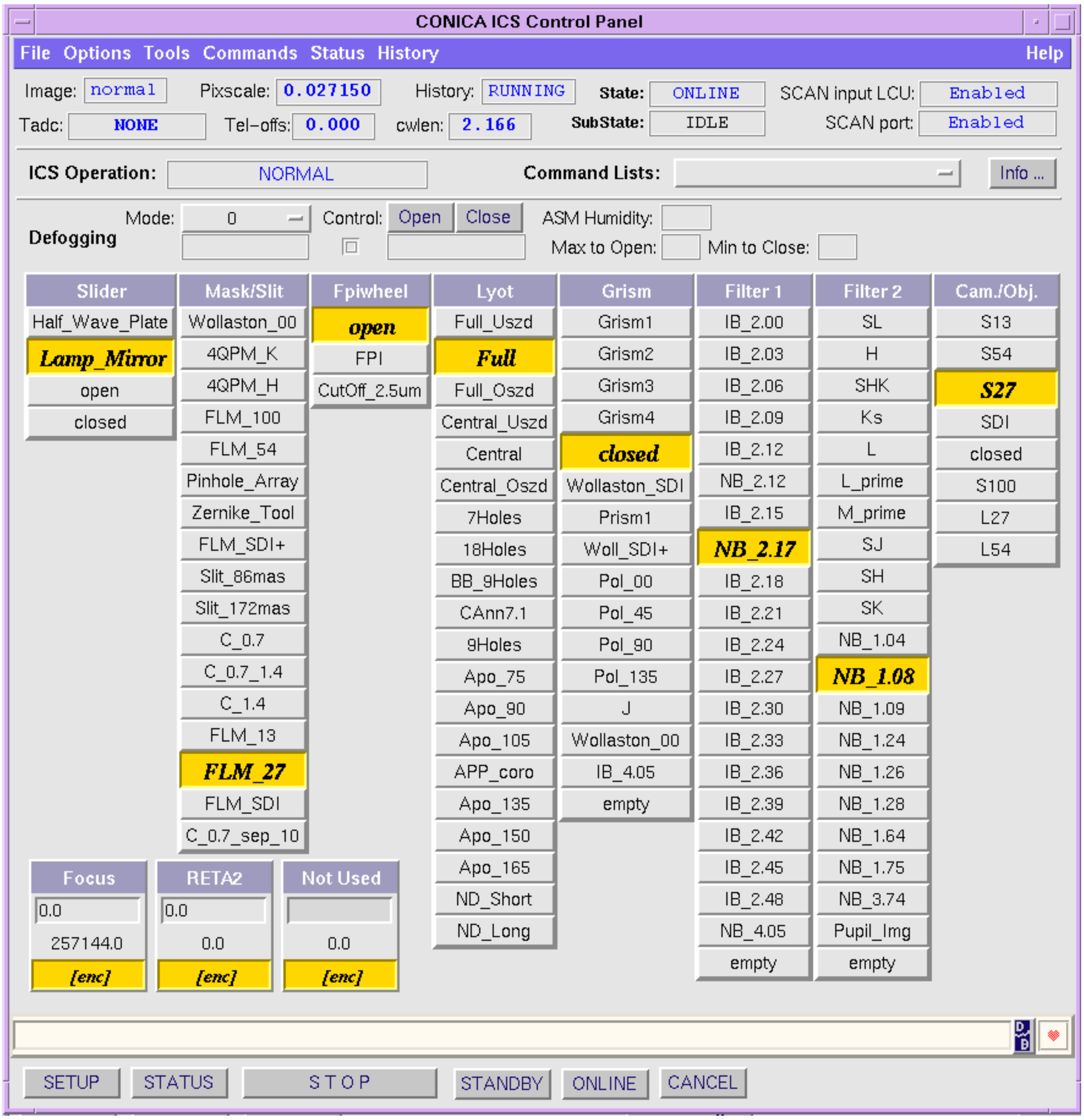

Figure 35: CONICA ICS control panel.

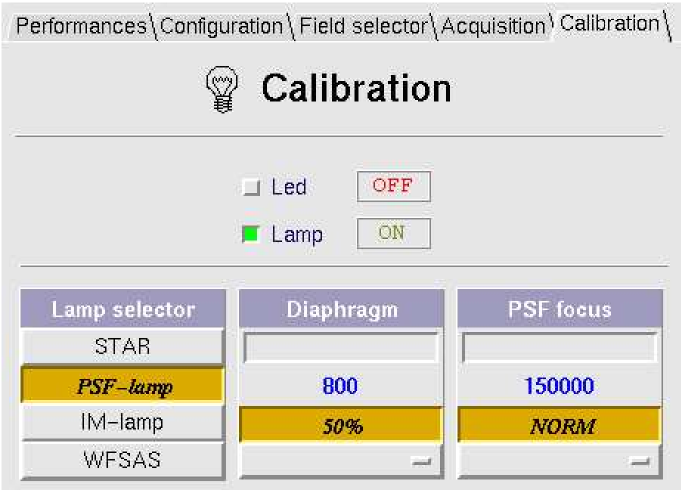

Figure 36: SOS-NAOS calibration source panel.

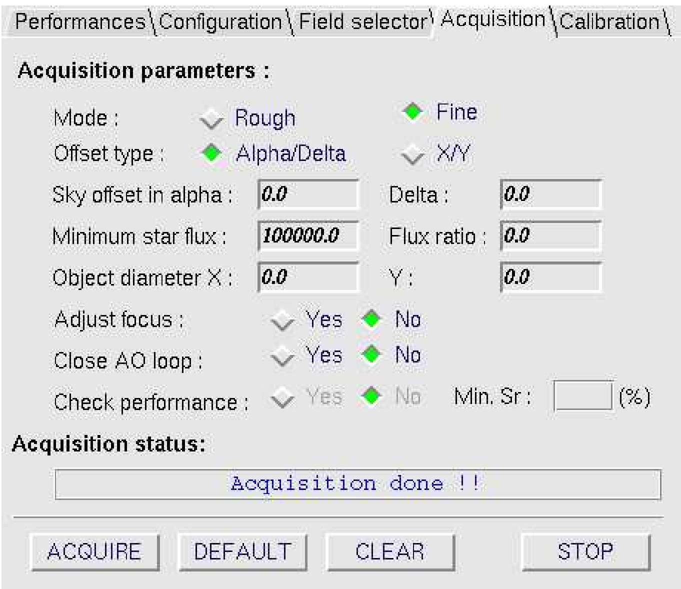

Figure 37: SOS-NAOS acquisition panel.

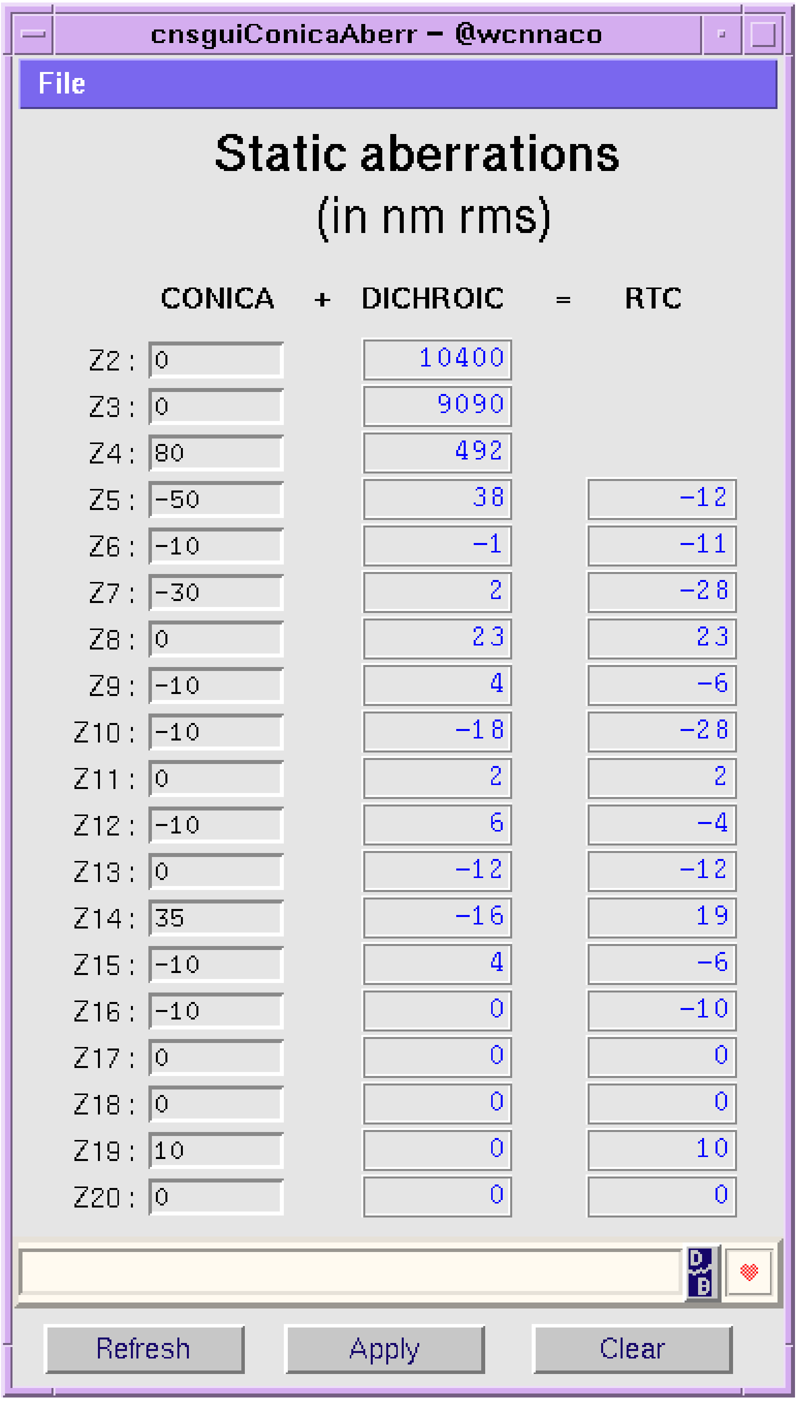

Figure 38: cnsguiConicaAberr panel. When clicking on *refresh*, values of CONICA's aberrations coefficients present in the configuration file are loaded (those shown on the image). They are then added to the aberrations due to the dichroic used (estimated separately), in our case the VIS dichroic before application. New coefficients computed with OPRA have to be added to those given by the first refreshment (and should not simply replace them).

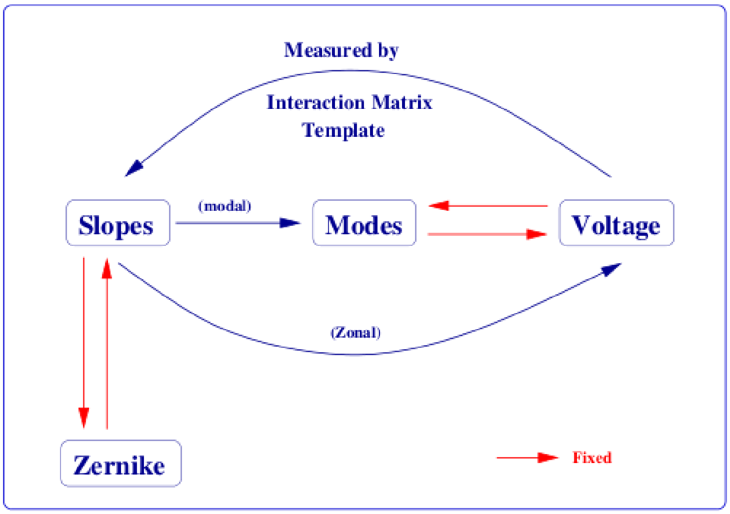

Figure 39: Relations between the different matrices used during the calibrations.

Appendix D
IDL code computing the VLT pupil

A copy of the implemented IDL code computing the VLT pupil is attached hereunder. We also give some useful advice to facilitate the understanding of the code:

- The pupil is first computed for a 100 times bigger image 16000x16000 px instead of 160x160px demanded by MVD. Then the `congrid(input_img, output_hor_dim, output_vert_dim, interpolation_type)` function is used to resize the pupil. We used a cubic interpolation type. The asset of this operation is the intermediate values (between 0 and 1) filling the pixels on the edge of the created pupil, providing thereby a better simulation of a circular pupil.

- ; denotes the beginning of comments.

- `dist(rad)` creates a disk filled with unit values, the argument `rad` is its radius.

- `FFT(img)` takes the Fast Fourier Transform of `img`.

The computed pupil is then given in figure 40.

```
pro pupil_VLT

;Parameters
D_out = 8.0
D_in = 1.116
n_pix=160

;Useful definitions
ratio = D_in/D_out
n_cong=n_pix*100

;Declaration
puptmp = fltarr(n_cong, n_cong)
PSF = fltarr(n_cong, n_cong)

;Computation of the pupil
r= shift(dist(n_cong),n_cong/2.,n_cong/2.)
; "dist" creates a disk, with distances to the center, here it's shifted

puptmp = r LE n_cong/2. AND r GE ratio*n_cong/2.

;Congrid of the pupil
pup = CONGRID(puptmp, n_pix, n_pix,CUBIC=-0.5)


;PSF computation (optional since MVD also performs it)
PSF = abs(FFT(pup))^2
PSF = shift(PSF,n_pix/2.,n_pix/2.)
; if no "shift", the Airy Pattern is centered on the corners of the output image
```

```
;Writing
writefits,'Pupil_VLT.fits', pup
writefits,'PSF_VLT.fits', PSF

end
```

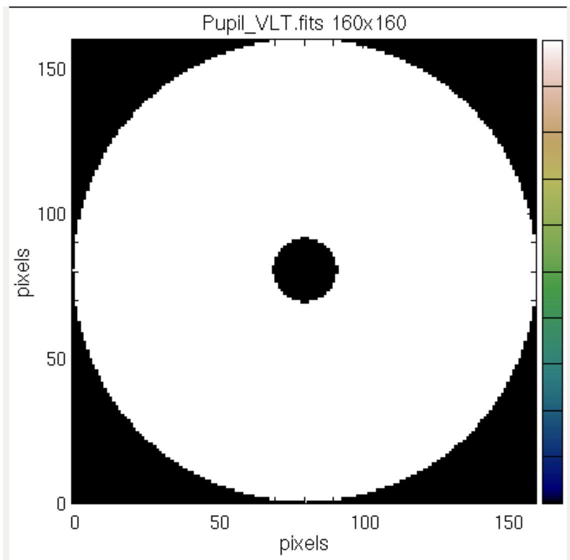

Figure 40: VLT pupil computed with the IDL code above-written.